NORTHWESTERN UNIVERSITY

Phases and Actuation of Superparamagnetic Soft Matter

A DISSERTATION

SUBMITTED TO THE GRADUATE SCHOOL
IN PARTIAL FULFILLMENT OF THE REQUIREMENTS

for the degree

DOCTOR OF PHILOSOPHY

Field of Materials Science and Engineering

By

Chase Austyn Brisbois

EVANSTON, ILLINOIS

December 2022

ABSTRACT

Phases and Actuation of Superparamagnetic Soft Matter

Chase Austyn Brisbois

External manipulation of soft matter underlies a multitude of advancements in far-from-equilibrium materials. The application of magnetic fields has proven tremendously beneficial due to its ability to impart rapid and precise changes throughout soft magnetic systems. This has led to scientists and engineers to develop composite materials that take advantage of the characteristics of soft condensed matter with those of magnetic nanoparticles to achieve novel properties not possible in the absence of a magnetic field. Using a combination of theory, experiments, and simulation, we describe how magnetic fields affect the state of distinct colloidal nanostructures composed of superparamagnetic particles suspended in a liquid environment. This dissertation is composed of two parts that each investigate a superparamagnetic system first with a static field and then with a dynamic field. Part One focuses on magnetoelastic membranes in precessing magnetic fields. In the fast precession regime, we uncover buckling mechanisms that affect membrane actuation. By lowering the precession frequency, we found dynamic steady-states where membrane locomotion could be achieved. In Part Two, we explore the effects of

magnetic fields on magnetic crystal phases and morphology. We show how magnetic coupling directly affects the morphology of superparamagnetic rods in static magnetic fields. Driving such rods to precess will impart positional ordering to a layered (smectic) liquid crystal phase. In these works, we have striven to develop simple mathematical relationships between pertinent system properties and dimensionless control parameters in order to confer physical intuition to the reader.

Acknowledgements

I would like to offer my sincere appreciation to everyone I met during my doctoral studies. I am particularly grateful to my mentor, Prof. Monica Olvera de la Cruz, for her support and allowing me the independence to grow as a scientist. Her kindness and sincerity are matched only by her potent experience and scholarly intellect. I would also like to extend my thanks to the members of my committee, Prof. Samuel Stupp, Prof. Michelle Driscoll, Prof. Petia Vlahovska, and Prof. Peter Voorhees, for their guidance during my qualifying exam, and for reviewing this thesis that represents all the work I did at Northwestern.

I was able to work with many skilled and knowledgeable collaborators at Northwestern. I want to thank Dr. Pablo Vàzquez-Montejo for his analytical work together with Prof. Mykola Tasinkevych for formulating the continuum mechanics model, and giving me the opportunity to visit Europe for the first time. Later on, I had the privilege to work with Dr. Zack Urbach and Dr. Sarah Park from the Mirkin group. I am grateful for speaking with them and others at the monthly meeting for the Center for Bio-inspired Energy Science (CBES).

I will never forget all the members of the Olvera group that helped and accompanied me during my years in Evanston. I would like to thank my officemates, Dr. Siyu Li, Dr. Meng Shen, Yange Lin, Yang Li, Zehao Song, Dr. Annalisa Cardellini, and Dr. Anisha Shakya, for being a source of scientific discussion and chill vibes. I must thank the experienced Dr. Trung Nguyen, Prof. Baofu Qiao and Dr. Felipe Jimenez Angeles, who would always answer my incessant questions. For those elsewhere in the lab, I would like to thank Dr. Aaveg Aggarwal, Dr. Leticia Lopez, Ali Ehlen, Hector Manuel Lopez de la Cerda Rios, and Curt Waltmann for all the great discussions at subgroup meetings or just in the hall.

All of the plants that got me through the COVID-19 pandemic would not have existed without Prof. Nyree Zerega and Prof. Aykut Erbas.

I would be remissed if I did not acknowledge all the people I who supported me before I started graduate school. It was my mentor at the National Institutes of Health, Dr. Jennifer C. Lee, that suggested I apply to Northwestern University. She instilled a brand of scientific vigor that I carry around with my today. I want to thank her and the other members of the Lee lab, Dr. Ryan McGlinchey, Dr. Jessica D. Flynn, Dr. Michel de Messieres, and Dr. Zhiping Jiang, for all of the thoughtful (and fun) conversations we enjoyed.

I would like to acknowledge my time at the Physical Measurement Laboratory in the National Institute of Standards and Technology. My advisor, Mr. Joseph J. Kopanski, along with everyone else I worked and ate lunch with, Dr. Yaw S. Obeng, Dr. Jungjoon Ahn, and Dr. Lin You, help broaden my scientific and personal horizons.

I first began developing as a scientist during my undergrad at SUNY Albany. I have my advisor, Dr. Robert Brainard, to thank for instilling me with many of the habits and practices of an efficient and diligent scientist. I would like to thank Dr. William George Earley for all the advice he gave me, which I keep in mind everyday.

I would like to thank my parents for their support, which started well before graduate school. I would also like to say thanks to my friends, Kyle, Henry, Bradley, Utthara, Sonal, and Anusheela, along with all the horticulturally-inclined folks at the graduate gardens.

Lastly, I would like to acknowledge the International Institute of Nanotechnology (IIN), the Center for Bio-inspired Energy Science (CBES), the Sherman Fairchild Foundation, and the team at the Quest computing cluster for providing financial and computational support during my Ph.D.

List of abbreviations

0-D	Zero dimensional
1-D	One dimensional
2-D	Two dimensional
3-D	Three dimensional
BCC	body-centered cubic
CBES	Center for Bio-inspired Energy Sciences
CM	Continuum Mechanics
CSM	Continuous Symmetry Measure
DNA	Deoxyribonucleic acid
EL	Euler-Lagrange
IIN	International Institute of Nanotechnology
LAMMPS	Large-scale Atomic/Molecular Massively Parallel Simulator
LB	Lattice Boltzmann
MD	Molecular Dynamics
NN	Nearest Neighbor
NPT	Constant (Particle) Number, Constant Pressure, Constant Temperature
NVT	Constant (Particle) Number, Constant Volume, Constant Temperature
OVITO	Open Visualization Tool

PDMS	Polydimethylsiloxane
VMD	Visual Molecular Dynamics
WCA	Weeks-Chandler-Andersen

Dedication

I dedicate this work to my friends and family, but especially to my daughter, Nikita.

Table of Contents

ABSTRACT 3

Acknowledgements 5

List of abbreviations 8

Dedication 10

Table of Contents 11

List of Figures 14

Chapter 1. Introduction to Superparamagnetic Soft Matter 26

- Part 1: Magnetoelastic Membranes 28
- Part 2: Colloidal Magnetic Crystals 29

Chapter 2. Magnetoelastic Membranes in Fast Precessing Fields 34

- 2.1. Introduction 34
- 2.2. Methods 38
  - 2.2.1. Molecular Dynamics Simulations 38
  - 2.2.2. Continuum Elastic Model 41
  - 2.2.3. Analytical Solution of Unstretchable Magnetoelastic Membrane 43
- 2.3. Results and Discussion 44

2.3.1. Magnetoelastic membranes under linear compression 44
2.3.2. Torque on a magnetoelastic membranes 49
2.4. Conclusions 55

Chapter 3. Magnetoelastic Membrane swimmers 57
3.1. Introduction 57
3.2. Methods 61
3.2.1. Molecular dynamics model 61
3.2.2. The lattice Boltzmann method with immersed boundaries 62
3.3. Results and Discussion 64
3.3.1. Phases of a magnetoelastic membrane 64
3.3.2. Hydrodynamics of membrane "wobblers" 73
3.3.3. Directed membrane swimming 80
3.4. Conclusions 82

Chapter 4. DNA-Assembly of Magnetic Colloidal Crystals 85
4.1. Introduction 85
4.2. Methods 86
4.2.1. Molecular dynamics simulations 86
4.2.2. Magnetic dipole component to surface energy 89
4.2.3. Magnetic coupling between clusters 90
4.3. Results and Discussion 91
4.4. Conclusions 97

Chapter 5. Precession-driven phase transitions in Superparamagnetic Nanorods 99
5.1. Introduction 99
5.2. Methods 101
5.2.1. Precession angle for dilute superparamagnetic rods 101
5.2.2. Magnetic MD Model 105
5.2.3. Purely steric "strong precession" MD model 107
5.3. Results and Discussion 110
5.4. Conclusions 115
Chapter 6. Summary and Outlook 117
6.1. Dissertation Summary 117
6.2. Outlook for Future Work 118
6.2.1. Magnetoelastic Membranes 118
6.2.2. Colloidal Magnetic Crystals 121
Bibliography 124

List of Figures

2.1 Magnetoelastic membranes under precessing magnetic fields. (A) Magnetic fields precess at an angle θ around the Z axis. (B) A membrane composed of hexagonally-packed superparamagnetic colloids possessing 3 bending axes (red arrows) with magnetic moment μ precessing with the field. Time-averaged interaction potential $\langle U_d \rangle_t \propto (3\cos^2\beta - 1)(3\cos^2\theta - 1)/r^3$, where r is the distance between the particles and β is the angle between the center-to-center vector and the precession axis. (C) Small-angle precession ($\theta < \theta^*, \gamma > 0$). A schematic cross-section of a membrane shows preferred dipole orientation which interact with the potential $\langle U_d \rangle_t$. (D) Schematic of a membrane minimizing its bending energy by adopting a single "arch". Each edge has length L_o where two parallel boundaries are separated by a distance L. (E) A membrane with opposite boundaries at a distance L. Each boundary is rotated by α in opposite directions for a total angle of 2α. The midpoint of each boundary is stationary and defines a centerline that remains perpendicular to the magnetic field precession axis. (F) Large-angle precession ($\theta > \theta^*, \gamma < 0$). This leads to a change in the membrane's magnetic modulus which depends on the angle of precession, $m(\theta) \propto (3\cos^2\theta - 1)$. Cross-section of a membrane shows an alignment of rotating dipoles interacting with the potential $\langle U_d \rangle_t$. 36

2.2 Effect of boundary separation on an elastic membrane with no external field ($\gamma = 0$). (A) Under a uniform compression ($L/L_o = 0.8$) on opposite, stiff boundaries (blue), the strain related to the in-plane deformations is released via a buckling transition where the membrane adopts a symmetric arch shape. The edges that define the boundary separation are colored blue. (B) Total membrane energy obtained from molecular dynamics (MD) simulations as the distance, L, between opposite boundaries changes. The total membrane energy (in units of kT) is normalized to the total number of colloids, N. The colloids are modeled as 10 nm particles under room temperature. 44

2.3 Shifted components of the total membrane energy in the absence of a magnetic field: bending energy, stretching energy, and soft core particle repulsion (Weeks-Chandler-Anderson force) for (A) membrane boundary separation and (B) twisting. 45

2.4 Influence of boundary separation on magnetoelastic membranes. Total membrane energy as a function of L obtained via MD simulations. The results show membrane contraction under (A) small-angle magnetic field precession ($\gamma > 0$) and expansion under (B) large-angle precession ($\gamma < 0$). Curves are shifted by the value of the energy (in units of kT) at $L/L_o = 1$, ϵ_i, for clarity and normalized by the number of colloids, N. (C) Calculated membrane total free energy $\mathcal{F}$ from continuum mechanics with $\gamma > 0$ and $\gamma < 0$. Free energy curves are shifted by $\mathcal{F}_i, i = 1, 2$, the values at $L/L_o = 1$, for clarity and normalized to the bending modulus. (D) Snapshots of membrane configurations at boundary separation L/L_o = 0.5, 0.75, and 0.90 ($2\alpha = 0$) at under different values of γ. Field precession at $\theta < \theta^*$ causes secondary buckling of the free membrane edges which is reflected by the brake in the slope of the free energy curves at $\gamma = 150$ and 300. The edges that define the boundary separation are colored blue. 48

2.5 Application of magnetic field breaks membrane symmetry. (A) MD simulation data for the transition between symmetric and asymmetric membrane configurations as a function of γ and L/L_0. Above the critical values of $|\gamma|$, only asymmetric configuration exists. (B) Membrane profiles found by analytical methods for $\gamma = 100$ and -100 ($L/L_o = 0.75$). 50

2.6 Profile curves for the symmetrical ($F_z = 0$) analytical solutions to a magnetoelastic membrane at various positive and negative values of γ. 50

2.7 Schematic drawing of a membrane showing the angle Θ that the local tangent vector $\mathbf{e}_l$ makes with the precession axis Z. The membrane edges which are parallel to the X axis are fixed. 51

2.8 Effect of boundary rotation on an elastic membrane with no external field ($\gamma = 0$). (A) Total membrane energy (in units of kT) normalized by the number of colloids, N obtained from molecular dynamics (MD) simulations as the total angle, 2α, between boundaries changes with constant separation ($L/L_o = 0.5$). (B) MD simulated membranes show the conformational transition as the angle between stiff, separated boundaries (blue) increases (images represent $2\alpha = 0, 45°, 90°$, respectively). The membrane undergoes a conformational transition at some threshold value of $2\alpha \simeq 70°$ to relieve accumulated stretching strain causing the formation of a hysteresis. 51

2.9 Influence of boundary rotation on magnetoelastic membranes. MD simulations results for membrane energy as a function of 2α, the twisting angle of two opposite membrane edges, at $L/L_0 = 0.5$, and for several values of (A) $\gamma > 0$ and (B) $\gamma < 0$. Membranes resist twisting at small 2α under small-angle magnetic field precession ($\gamma > 0$) and for all rotation angles under large-angle precession ($\gamma < 0$). The solid lines represent rotation from $2\alpha = 0$ to $2\alpha = 90°$ and the dashed lines represent the reverse path back to $2\alpha = 0$. There exists a threshold value of γ above which the hysteresis from rotation disappears, green and magenta curves. Curves are shifted by the value of the energy (in units of kT) at $2\alpha = 0$, ϵ_i, for clarity and normalized by the number of colloids, N. Energy is given in the Lennard-Jones units. (C) Membrane free energies from CM calculations as a function of 2α for $\gamma > 0$ and $\gamma < 0$. Free energy curves are shifted by $\mathcal{F}_i$, the free energy values at $2\alpha = 0$, for clarity and normalized to the bending modulus. (D) Snapshots of the membrane configurations at $\alpha = 0, 45°, 90°$, respectively, under different values of γ ($L/L_o = 0.5$). The edges that define the boundary separation are colored blue. 52

2.10 Components of the total membrane energy in the presence of a magnetic field: dipole interaction energy, bending energy, stretching energy, and soft core particle repulsion for (A) $\gamma = 150$, (B) $\gamma = 1200$, (C) $\gamma = -12$, and (D) $\gamma = -96$. For clarity, energy curves are shifted and error bars on reverse curves are omitted. 53

2.11 Numerical calculations for the total bending energy of a membrane with three bending axes at various curvatures. We fit the continuum bending constant, $\kappa_{real} \approx 26$, to this line, $E = \pi\kappa_{real}/R$. 53

2.12 Values for the shifted energy constants used in Figure 2.4 and 2.9 as a function of γ. 54

3.1 An image of a truncated magnetoelastic membrane in a precessing magnetic field. The degree of truncation $S = h/2R$, where h is the sagitta length of the removed circular segment, and R is the membrane radius, determines membrane symmetry. The magnetic field $\vec{\boldsymbol{H}}$ precesses at the angle θ around the z axis with a phase given by $\phi = \omega t$, where ω is the precession frequency and t is time. The field induces a transverse wave along the membrane perimeter with amplitude A, measured from the x-y plane. Coloration indicates z position as shown by the color bar on the left. 57

3.2 A circular magnetoelastic membrane in a precessing magnetic field. (a) Transverse waves propagate around the membrane above a critical frequency ($\omega > \omega_c$) with negligible membrane rotation, highlighted by the black colored colloid. Coloration indicates z position as shown by the color bar in the top right corner. (b) A schematic plot showing the phase diagram of a membrane. Above the dotted black curve, the 'wobbling' membrane remains perpendicular to the precession axis and possess the rotational waves from (a). The wave amplitude maximizes just before the transition. Below this curve, the membrane buckles and rotates asynchronously with the field, hence 'dancers'. (c) The bending stiffness controls the shape of the rotational waves. The black arrows indicate the direction of wave propagation along the perimeter (thick arrow) and radially toward the membrane center (thin arrow). 58

3.3 The synchronous-asynchronous (wobbler-dancer) transition frequency ω_c for a magnetoelastic membrane. (a) Molecular dynamics calculation of ω_c as a function of the field precession angle θ. The solid and dashed lines indicate a dipole magnitude of $\mu = 2$ and $\mu = 1$, respectively. The inset shows the dimensionless transition frequency ω_c/Ω, where Ω is the membrane's characteristic rotation frequency. The green-dashed line represents the theoretical transition at $\omega_c/\Omega = 2/\pi$, which, near $\theta = 90°$, is independent of bending stiffness ($\kappa = 1$, orange. $\kappa = 100$, blue/red). The black squares show the transition calculated from lattice-Boltzmann simulations. (b) Supercritical and subcritical behavior of the total energy U (magnetic + bending) in units of ϵ. The precession frequency is close to the critical frequency, $0.029 < \omega_c < 0.030$ ($\theta = 80^\circ$). Fourier transform of the rotational wave amplitude (bottom). 64

3.4 Fluid flow around a magnetoelastic membranes in the "wobbler" regime. The top images show the total force vector for each colloid (blue arrows) alongside the dipole orientation (cyan arrows) for a precessing field (μ =1, $\theta = 70^\circ$, $\omega = 0.1$). The bottom images show streamlines around the membrane, where the color indicates flow speed u. (a) A snapshot of a circular membrane. (b) Two snapshots of a truncated circular membrane separated by a shift in the field precession $\Delta\phi = \omega t = 6\pi/5$. 67

3.5 Actuation drives circular locomotion of truncated magnetoelastic membranes through a viscous fluid. (a) The average rotational ("wobble") wave amplitude A_{avg}, scaled by the membrane radius R, depends inversely on the magnetoviscous parameter $\tau\omega$. Data points from lattice Boltzmann simulations are compared to our analytical model (solid blue line). The coloration of the simulation data notes the degree of truncation S. The inset shows the variation in A/σ over time based on membrane geometry (S = 0.05, black; S = 0.5, gray), where σ is the colloid diameter. (b) The path taken by a membrane in a precessing field. The arrow indicates the travel direction with velocity V. The inset shows the radius ρ of this path as a function of S. (c) The membrane velocity is proportional to $A_{avg}^2 \propto (\tau\omega)^{-2}$ and scales with $S^{3/2}$ due to changes in the length of the membrane perimeter. The data point shapes are coded by the membrane radius ($R = 7$, triangle; $R = 9$, square; $R = 12$, circle). The blue line shows our analytical prediction (slope = 1.0). The inset shows the continuous inversion symmetry measure for a flat truncated membrane. 69

3.6 A two-step magnetic field directs a swimming membrane along a path. (a) First, a membrane wobbler moves under a precessing magnetic field. After it rotates a half-turn (#1), the precession switches to a fast frequency at $\theta = \pi/2$ while the axis rotates to flip the membrane (#2). (b) We define the angles that the normal vector $\boldsymbol{n}$ and the truncation vector $\boldsymbol{S}$ make with the x axis as ζ_n and ζ_S, respectively. (c) The path in conformation space over the two-step field. (c) Repeated cycles from (a) move the membrane against the Brownian motion of a thermalized fluid. The upper panel shows the motion of the membrane in the x-y plane. The black arrow indicates the direction of motion. The lower panel shows the displacement in the z direction. 75

4.1 Molecular dynamics snapshot of a 1:1 stoichiometry mixture of complementary DNA-coated superparamagnetic nanoparticles in a magnetic field pointing to the left. Each particle has a dipole moment of (a) 0.0, (b) 0.5, and (c) 0.9. Colors represent single crystals of nanoparticles. 90

4.2 Normalized potential energy curves for a square prism crystal as a function of crystal aspect ratio (AR). The inset shows how increasing the ratio between field and surface energy density increases the equilibrium AR of the crystal. 92

4.3 Estimate for the magnetic contribution to the surface energy for (100), (110), and (111) surfaces of magnetically saturated 20 nm magnetite nanoparticles. 93

4.4 a) Schematic showing how magnetic coupling between individual superparamagnetic particles, Γ_1, and the DNA hybridization interaction strength, ε_{DNA}, between complementary particles affect system morphology. b) Radial pair distribution plots with increasing ε_{DNA}. c) Mismatch probability between complementary particle types increases with increasing magnetic field. d) The change in the effective magnetic coupling between clusters, Γ_{eff}, as cluster diameter grows (in lattice parameter units). e) The aggregation parameter with increasing cluster diameter (in lattice parameter units). f) The magnetic coupling between two clusters of equal sizes, Γ_{eff}, normalized by the magnetic coupling between individual particles, Γ_1. g) Calculation of the diameter of a cluster at the onset of chain formation given the initial magnetic coupling. It follows the scaling law $d_{eff} \sim \Gamma_1^{-1/3}$. This figure is adapted from Park *et al.* [80] 94

4.5 (left) Scanning tunneling electron microscope image of a rod under a 3800 G field, assembled from (left) 20 nm Fe_3O_4 nanoparticles, scale bar: 500 nm and (right) 10 nm Fe_3O_4 nanoparticles, scale bar: 2 µm. 95

4.6 An image of the title page for Haüy essay on his theories for crystalline solids. On page 21 he states the beginning of his construction: “...avec une multitude de petits cubes, une pile quadrangulaire régulière, c’est-à-dire, composée de couches qui aillent en décroissant uniformément de la base au sommet.” Translating this as: “ ...with a multitude of small cubes, a regular quadrangular pile, that is to say, composed of layers which decrease uniformly from the base to the top.” [117] 96

4.7 Haüy construction of a dodecahedron using cubes. Image from Wolfram [118]. 97

5.1 Precession of a superparamagnetic rod. (a) Schematic for a magnetic field $\boldsymbol{H}$ precessing around the z-axis at a precession angle θ. A rod composed of a stiff chain of superparamagnetic particles (blue) of diameter σ are coated by a non-magnetic material (orange); the coating determines its aspect ratio l/d. The rod orientation is measured by its angle β to the precession (z) axis. (b) The external field $\boldsymbol{H}$ drives rod precession for $\theta = 20°$ and $50°$. As the field precession frequency ω increases, β decreases. The blue shaded region highlights when the diffusion time over the rod area is less than the precession period. (inset) The reduced frequency at which $\beta = \theta/2$ as a function θ for simulated (red) and theory (green dash). 110

5.2 (a) The magnetic coupling $\Gamma(\ 1/d^3)$ decreases as the distance between dipoles ($\mu = 1$ (red) and 2 (green)) increases. (a, inset) The orientational order of magnetic rods as μ increases with error bars representing one standard error in the order. (b) Steric MD model, that assumes small Γ, where the red bead is the centre of precession for a rod ($l/d = 8$) and the white beads fill the skin of a double-cone matching the rod precession angle β. (c) The smectic order of the steric model at various precession angles showing how increasing β decreases the transition density. Shaded areas represent one standard error. (d) Steric model in the smectic phase; for clarity, only the red centre beads are shown. 112

5.3 (a) Magnetic MD model below (left) and above (right) the nematic-smectic transition ($\theta = 20°$, $\omega' = 0.2$). (b) The smectic order κ and rod angle β for the magnetic MD model as the system density ρd^3 increases. (c) The phase diagram separating the nematic and smectic regions. The orange data is the strong precession model and the black squares denote the observed transition from the magnetic MD model, with green and blue highlight snapshots from (a). 114

5.4 A (50% cyan $l/d = 4$: 50% red $l/d = 8$) binary mixture of rods in the smectic regime, centres shown for clarity. 115

6.1 (a) A membrane petal with intrinsic curvature, left, can be opened with a large-angle precessing field, right. (b) A square membrane forced to lie in along the precession axis, will curl similar to filaments in a precessing field. (c) Closed membrane spheres, left, will deform in the presence of a large-angle precessing field, middle, and a small-angle precessing field, right. 119

6.2 Various membrane shapes in large-angle precessing field. The color shows displacement in the direction of the precession axis. 121

6.3 Colloidal crystals in a rotating magnetic field with various number n and dipole ratios μ ratios. 122

CHAPTER 1

Introduction to Superparamagnetic Soft Matter

Humanity has been aware of the power of magnetic fields since the first archaic lodestones was picked up off the ground. Modern knowledge of physics allows us to understand that these rocks have been magnetized, usually, and most theatrically, from the intense magnetic fields generated from lightning strikes [1]. One can almost imagine the fantastic awe an ancient hominid would feel to witness such an event. Lodestones attracted pins of iron and allowed them to be used in compasses for navigation. It is no wonder that such minerals were incorporated into pendants and talismans in an attempt to influence the external world, though such endeavors mostly focused on curing or preventing diseases [2]. Unfortunately, without a scientific understanding of the underlying phenomenon, the full potential remained elusive. It wasn't until William Gilbert of Colchester published *De Magnete* in 1600 that humanity began to appreciate and understand natural magnets in a comprehensive, and scientifically rigorous manner [3]. Over four centuries later, contemporary knowledge of magnetic materials has broadened widely giving us access to a level of technological control not even dreamed by the healing shamans of yore.

Bulk magnetic materials, such as magnetite, possess many magnetic domains. Each magnetic domain is a small volume where the magnetic dipoles of all the atoms or molecules are aligned in the same direction. Many ferromagnetic materials do not appear magnetic because these domains are antiparallel, or otherwise randomly oriented, canceling out the net magnetic field generated by the collective dipoles within each domain. The entire material can be magnetized by applying an external magnetic field, which reorients these domains. However, the energy needed to do this is typically large and the material is left with a residual magnetization when the external field is turned off. If the particle is small enough, typically less than 100 nm, it will contain a single domain whose dipole can be flipped from thermal energy alone. In technical terms, the Néél relaxation time of the dipole is much shorter than magnetization measurement time. This phenomenon is called superparamagnetism. In the absence of a magnetic field, these particles have no net magnetization, but benefit from a large magnetic susceptibility with high magnetic saturation.

Superparamagnetic nanoparticles have wide-reaching scientific and technological applications. They are actively researched for their magnetic properties and are used in nanomedicine, actuators, photonics, and industrial applications. Their applications broadly depend upon their arrangement within matter based on their connectivity in space: 0-D (ferrofluid), 1-D (filaments), 2-D (membranes), and 3-D (bulk actuators/crystals). This dissertation will touch on the properties inherent in all four connectivities. We split this thesis into two parts: In Part 1 (Chap. 2 and 3), we focus on the actuating and swimming properties of magnetoelastic membranes, and, in Part 2 (Chap. 4 and 5), the morphology of colloidal magnetic crystals assembled from individual nanoparticles and stiff nanorods. Each Part is broken into two chapters. The first chapter will involve a static (or quasi-static) magnetic field which will inform the time-dependent dynamics induced by a precessing magnetic field in the next chapter.

Part 1: Magnetoelastic Membranes

Of the four arrangements of superparamagnetic matter previously mentioned, 2-D sheets are the least studied due to challenges in their synthesis. However, the few experimental studies have suggested that the physical properties of magnetic sheets introduce new functionality not possible with other 0-D, 1-D, or 3-D arrangements such as dynamic encapsulation of catalysts/drugs, and 2-D patterning for anisotropic mechanical properties [4, 5]. The possibility of patterning uniform arrays of membranes is of particular interest for tailoring shape-transforming modalities. Hu *et al.* used magnetic patterning (i.e., arranging the orientation of imbedded magnetic particles in a pattern) as a main mechanism for sheet swimming and encapsulation. Li *et al.*. shows similar functionality by patterning both the sheet shape and magnetic components. Encapsulation and swimming are possible with other structures like 1-D filaments or 3-D magnetoelastomers, however, magnetic sheets hold the possibility of doing both dynamically.

Chapter 2: Membrane actuation. Achieving shape-transforming functionality in magnetoelastic membranes requires a mastery of membrane actuation. We begin by investigating a membrane in a fast precessing field. We show how induced magnetic interactions affect the buckling and the configuration of magnetoelastic membranes in rapidly precessing magnetic fields. The field, in competition with the bending and stretching of the membrane, transmits forces and torques that drives the membrane to expand, contract, or twist. We identify critical field values that induce spontaneous symmetry breaking as well as field regimes where multiple membrane configurations may be observed. Our insights into buckling mechanisms provide the bases to develop soft, autonomous robotic systems that can be used at micro- and macroscopic length scales.

Chapter 3: Membrane swimming. The push for microscale robots necessitates locomotion at the scale of bacteria. Swimming at the smallest scales must satisfy the Scallop Theorem [6], which states that back-and-forth motion using only one degree of freedom will not produce a net swimming velocity. While using magnetic fields to manipulate a microrobot has many advantages, it requires that the field satisfy this condition in order to impart a swimming motion. For a magnetic membrane to swim, it must (1) have at least two degrees of freedom and (2) produce a motion that moves its center of mass. We meet the first requirement by decreasing the symmetry of the membrane and address the second requirement by defining the conditions necessary to produce a non-reciprocal undulation in the membrane. Beginning with a homogeneous, circular membrane, we show that truncations of circular segments linearly increase the velocity of the center of mass as the membrane undulates in a precessing magnetic field. The velocity is proportional to the membrane asymmetry, a critical design consideration for membrane robots.

Part 2: Colloidal Magnetic Crystals

Colloidal crystals have seen a great deal of development due to their mechanical and optical properties and potential applications in photonics and sensors [7]. The properties of a colloidal crystal depend upon the material properties of the colloid, the assembly method, and the crystal thermal stability, symmetry and shape. Frequently, these four aspects are closely dependent on each other. By making them independent, the properties of a crystal can be tweaked or redesigned without overhauling the entire material system or developing a new synthetic procedure. DNA-mediated assembly imparts control over almost any aspect of the crystal symmetry and thermal stability by creating an independent shell-core system, where the DNA shell can be modified without affecting the inner core [8]. However, chemical linkers [9], like DNA, are not the only method of obtaining crystalline order. In fact, in 1949, Onsager showed that steric interactions from particle shape alone can transmit order in colloidal liquid crystals [10]. When using a superparamagnetic core, an externally applied magnetic fields can be used to induce order directly *via* dipole-dipole magnetic coupling or, indirectly, in the case of 1-D filaments, *via* dynamic motion.

Chapter 4: Magnetic coupling effects in magnetic crystals. It is critical to understand the influence of dipole-dipole interactions and other competing forces on the self-assembly of superparamagnetic particles. In collaboration with the lab of Prof. Chad Mirkin, we study the assembly of superparamagnetic magnetite nanoparticles coated with complementary DNA. Under a static magnetic field, the nanoparticles assemble into elongated crystals. We explain the influence of magnetic coupling on crystal morphology as well as how the relative strength between DNA bonding and magnetic coupling will alter the crystalline order. These results directly affect how to control the order and shape of magnetic colloidal crystals.

Chapter 5: Precession-induced ordering in magnetic liquid crystals. The dynamic motion produced by precessing magnetic fields can drive matter into far-from-equilibrium states. We predict 1D periodic ordering in systems of precessing rods when magnetic coupling between rods remain negligible. The precession angle of the rods is completely determined by the field's precession angle and the ratio of the field's precession frequency and the characteristic response frequency of the rods. We develop a molecular dynamics model that explicitly calculates magnetic interactions between particles, and we also simulate rods in the limit of a strong and fast precessing magnetic field where inter-rod magnetic interactions are negligible, using a purely steric model. As the rod precession angle increases, the nematic-smectic transition density significantly decreases. The minimization of unfavorable steric interactions also induces phase separation in binary mixtures of rods of different lengths. This effect is general to any force that produces precession in elongated particles. This work will advance the understanding and control of out-of-equilibrium soft matter systems.

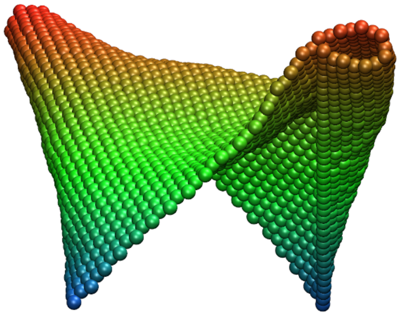

Part 1

Magnetoelastic Membranes

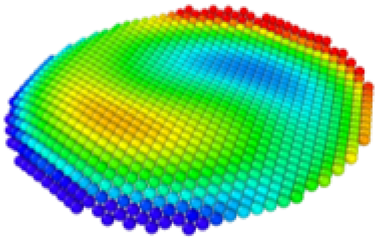

CHAPTER 2

Magnetoelastic Membranes in Fast Precessing Fields

2.1. Introduction

External magnetic fields can readily direct the collective behavior and actuation of magnetic colloids in order to influence the static structure of a magnetic material as well as control dynamic motion [11–17]. Incorporating magnetic particles into elastic media allows for a material to bend in presence of a magnetic field to realize accurate locomotion and conformational control. [4, 18–21]. Superparamagnetic nanoparticles are ideal for actuating systems at the micro- and nanoscale because the strength and direction of their magnetic dipole moments is directly controlled by the field. Furthermore, they lack a permanent dipole moment which prevents unwanted aggregation in the absence of a magnetic field [22–24].

Previous studies have focused on manipulating linear chains of superparamagnetic particles, also known as magnetoelastic filaments [25]. Using dynamic magnetic fields, magnetoelastic filaments have been incorporated into microswimmers [19, 26], active surfaces [20, 27], and gels [21, 28]. These past works have demonstrated the wide range of functionality avaible to filaments; however, we extending magnetoelastic matter into magnetoelastic membranes add the potential for switching between open and closed membrane states for molecular transport or catalysis and actuating modes based on sheet buckling. Synthesizing magnetoelastic membranes have been challenging but could be fabricated using existing techniques [28–30] and can use a rotating magnetic field to align particles into a plane.

This chapter introduces a theoretical framework for the actuation of magnetoelastic membranes [31] under fast precessing magnetic fields. We combine analytical description, continuum mechanics (CM) solutions and particle-based, coarse-grained molecular dynamics (MD) simulations to study how the precession angle, θ, of the field (2.1A) affects the configuration of a square-shaped patch of linked, superparamagnetic nanoparticles (2.1B).

Under a field that precesses at high frequency, the membrane conformation is quasistatic with respect to precession. That is, the precession period is short compared to the characteristic time scale for colloidal translation. Therefore, the magnetic energy of the membrane can be obtained by time-averaging the dipole-dipole interactions over the precession period. The time-averaged interaction potential, $\langle U_d \rangle_t$, between two rapidly rotating dipoles can be approximated as the magnetic interaction energy with a θ-dependent coupling strength. In this fast precessing regime, the behavior of an unstretchable membrane patch is characterized by a single dimensionless parameter defined as $\gamma = m(\theta)L_o^2/\kappa$, where $m(\theta)$ is the magnetic modulus, L_o is the length of one edge of a square membrane, and κ is the bending modulus [31]. This "magnetoelastic" parameter describes the relative strength between the magnetic and bending energy of the membrane. The angle of precession determines the magnitude of γ via the magnetic modulus, which can take positive or negative values and is zero at a critical precessing angle θ^*. More explicitly, in the case where $\theta < \theta^*$, the magnetic modulus is positive, ($\gamma > 0$, 2.1C) and negative for $\theta > \theta^*$ ($\gamma < 0$, 2.1F).

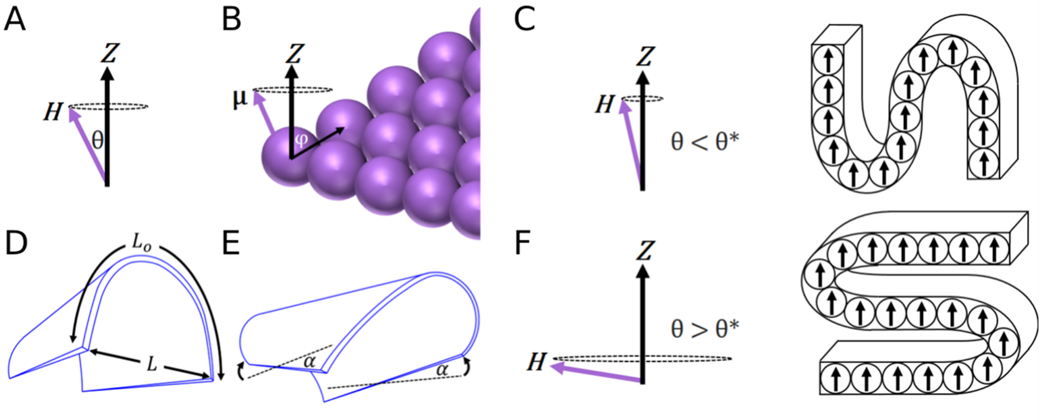

Figure 2.1. Magnetoelastic membranes under precessing magnetic fields. (A) Magnetic fields precess at an angle θ around the Z axis. (B) A membrane composed of hexagonally-packed superparamagnetic colloids possessing 3 bending axes (red arrows) with magnetic moment μ precessing with the field. Time-averaged interaction potential $\langle U_d \rangle_t \propto (3\cos^2\beta - 1)(3\cos^2\theta - 1)/r^3$, where r is the distance between the particles and β is the angle between the center-to-center vector and the precession axis. (C) Small-angle precession ($\theta < \theta^*, \gamma > 0$). A schematic cross-section of a membrane shows preferred dipole orientation which interact with the potential $\langle U_d \rangle_t$. (D) Schematic of a membrane minimizing its bending energy by adopting a single "arch". Each edge has length L_o where two parallel boundaries are separated by a distance L. (E) A membrane with opposite boundaries at a distance L. Each boundary is rotated by α in opposite directions for a total angle of 2α. The midpoint of each boundary is stationary and defines a centerline that remains perpendicular to the magnetic field precession axis. (F) Large-angle precession ($\theta > \theta^*, \gamma < 0$). This leads to a change in the membrane's magnetic modulus which depends on the angle of precession, $m(\theta) \propto (3\cos^2\theta - 1)$. Cross-section of a membrane shows an alignment of rotating dipoles interacting with the potential $\langle U_d \rangle_t$.

The sign and magnitude of the magnetoelastic parameter, γ, indicates how magnetic particles interact with each other [32, 33]. Therefore, γ influences the configuration of a membrane. In particular, there exists critical γ values which mark significant changes in membrane behavior. We show how changing the separation between opposite boundaries of the membrane (Fig. 2.1D) yields a transition from a symmetric to an asymmetric configuration at a critical field strength. Similarly, hysteresis present in the membrane energy as opposite boundaries are twisted by a total angle, 2α, (2.1E) can either be preserved or eliminated under weak or strong fields, respectively, allowing the membrane to resist or promote twisting.

The magnetoelastic membrane at room temperature is simulated as a hexagonally, close-packed monolayer of soft spheres possessing a dipole moment. Each sphere interacts with its nearest neighbors through stiff harmonic springs and angular harmonic potentials representing the stretching and the bending of the membrane, respectively. Spheres along the boundaries parallel to the X axis are bound to their initial position with an additional harmonic spring potential for a predefined distance, L/L_o, and angle, α. The bending of the membrane is determined along three directions along the membrane (Fig. 2.1B, red arrows) and uses the harmonic angle potential, $U_{bend} = \dfrac{\kappa}{2}(\theta_{NN} - \pi)^2$, where θ_{NN} is the angle three spheres make along one bending direction, and κ is the bending constant. To prevent the membrane from moving through itself, we add the repulsive Weeks-Chandler-Andersen (WCA) potential to all spheres. For the magnetic interactions, each sphere possesses a point dipole with the potential $U_{dipole} = \frac{\mu_0}{4\pi}\left(\frac{1}{r_{ij}^3}(\vec{\boldsymbol{\mu}}_{\boldsymbol{i}} \cdot \vec{\boldsymbol{\mu}}_{\boldsymbol{j}}) - \frac{3}{r_{ij}^5}(\vec{\boldsymbol{\mu}}_{\boldsymbol{i}} \cdot \vec{\boldsymbol{r}}_{\boldsymbol{ij}})(\vec{\boldsymbol{\mu}}_{\boldsymbol{j}} \cdot \vec{\boldsymbol{r}}_{\boldsymbol{ij}})\right)$, where μ_0 is the magnetic permeability of free space, $\vec{\boldsymbol{\mu}}$ is the magnetic moment and $\vec{\boldsymbol{r}}_{\boldsymbol{ij}}$ is the displacement vector between spheres. The total energy of the membrane is determined as the sum of each potential and the kinetic energy. Assuming the spheres represent 10 nm particles, the magnitude of the dipole moment represents typical values for superparamagnetic materials (20 – 140 Am^2/kg). For particles in water at $25°C$, the required frequency is 1 MHz. The required precession frequency to meet the quasistatic condition for the time-averaged interaction potential scales as $\omega \sim \sigma^{-3}$ [21], so as the particles increase in size, the required frequency decreases rapidly.

2.2. Methods

2.2.1. Molecular Dynamics Simulations

The membrane is coarse-grained into a close-packed monolayer of soft spheres with a dipole at their centers. Each sphere is connected to its nearest neighbors by a stiff, harmonic bond as well as an angular harmonic potential along the three directions each sphere makes with its neighbors. These define the stretching and bending of the membrane. The energy of the elastic bonds are given by the deviation from an equilibrium value equal to the particle diameter, $U_{bond} = \frac{K}{2}(r_{ij} - \sigma)^2$, where K is the bond stiffness, r_{ij} is the distance between neighboring spheres, $r_{ij} = |\vec{\mathbf{r_i}} - \vec{\mathbf{r_j}}|$, and σ is the diameter of a sphere. The bending of the membrane is determined using three directions along the membrane (Fig. 2.1B, red arrows). Despite this discretization, the bending energy is not sensitive to the bending axis (Fig. 2.11). In these directions, the bending energy is determined using a harmonic angle potential, $U_{bend} = \frac{\kappa}{2}(\theta_{NN} - \pi)^2$, where θ_{NN} is the angle between two bonds along one of the three bending axis, and which share a common sphere, and κ is the bending constant. To prevent the membrane from moving through itself, we add the Weeks-Chandler-Andersen (WCA) potential [34] between adjacent spheres defined as

$$U_{WCA} = \begin{cases} 4\epsilon[(\frac{\sigma}{r})^{12} - (\frac{\sigma}{r})^{6}] + \epsilon, & \text{for } r \leq 2^{1/6}\sigma \\ 0, & \text{for } r > 2^{1/6}\sigma, \end{cases} \tag{2.1}$$

where ϵ is the characteristic energy of the system, and r is the distance between spheres. The magnetic dipole interaction is modeled by giving each sphere a point dipole that interacts according to

$$U_{dipole} = \frac{\mu_0}{4\pi}\left(\frac{1}{r_{ij}^3}(\vec{\boldsymbol{\mu_i}}\cdot\vec{\boldsymbol{\mu_j}}) - \frac{3}{r_{ij}^5}(\vec{\boldsymbol{\mu_i}}\cdot\vec{\boldsymbol{r_{ij}}})(\vec{\boldsymbol{\mu_j}}\cdot\vec{\boldsymbol{r_{ij}}})\right), \tag{2.2}$$

where μ_0 is the magnetic permeability of free space, $\vec{\boldsymbol{\mu}}$ is the magnetic moment and $\vec{\boldsymbol{r_{ij}}}$ is the displacement vector between colloids. The total energy of the membrane is determined as the sum of each potential

$$U_{total} = \sum_{i,j}^{N} U_{WCA} + U_{bond} + U_{bend} + U_{dipole}, \tag{2.3}$$

and the kinetic energy of the system. The colloids along the boundaries parallel to the X axis are bound to their initial starting position with an additional harmonic potential, U_{bond}, where r_{ij} is simply the distance from its origin in space, and $\sigma = 0$.

The initial positions of the spheres in the membrane are determined by defining the boundary conditions (i.e. the boundary rotation, separation, and number of spheres at the boundaries), and then, if necessary, apply a static magnetic field. First, the number of beads on each edge is chosen. All simulations use $N_x = 41$ beads in the X direction and $N_y = 47$ in the Y direction. This defines the edges of the undistorted membrane, $L_x^o = N_x - 1$ and $L_y^o = (\sqrt{3}/2)(N_y - 1)$, leading to a square membrane. By choosing a boundary rotation angle, α, and boundary separation (fractional distance between edges), S, the projection of the initial membrane onto the $X - Y$ plane forms a rectangle with dimensions L_x and L_y where $L_x = L_x^o \cos(2\alpha)$ and $L_y = CL_y^o$. This area is filled in with

N_y alternating rows of N_x and $N_x - 1$ spheres to create a hexagonal lattice and gives the undistorted, flat membrane 2-fold symmetry. Next, the z position for each sphere is found with the following equation:

$$z = (x - \frac{L_x}{2}) \tan[\frac{2\alpha}{L_y}(y - \frac{L_y}{2})] - Z_o \sin[(y - \frac{L_y}{2})\frac{\pi}{L_y} - \frac{\pi}{2}] \tag{2.4}$$

where (x, y, z) is a sphere's coordinate in space, α is half the angle between the bound edges, and Z_o is a parameter that dictates wave height (set to 10).

The initial orientations of the dipole moment is irrelevant because the field should be sufficiently strong to dominate the torque on each dipole. For all simulations, the initial orientations are random. For the large-angle precession simulations, the membrane is subjected to a static magnetic field in the Y direction to initialize the membrane into its lowest energy configuration. If this is not done, the membrane would temporarily adopt a high energy, symmetric configuration. During the boundary separation and rotation simulations, the membrane edges move in steps of 1 degree and $0.025L_y^o$, respectively, and allowing the membrane to relax at each step.

All MD simulations use reduced units and set the temperature, sphere mass, sphere diameter, and $\frac{\mu_o}{4\pi}$ to 1. Each sphere is linked to its nearest neighbors as a harmonic spring with a force constant of 500 and equilibrium distance value of 1. Thermal energy is maintained using a Langevin thermostat with a damping parameter set to 0.1. The harmonic angle bending constant is set to 20. The external magnetic field, for the separation and twisting simulations, is set to 1000 while the magnitude of the dipole moment is varied between 0.257 and 1.818. The transition simulations for the symmetric and asymmetric membrane configurations are performed by varying bending constants to change γ rather than the magnetic dipole moment, set to 2.874. The asymmetry of the membrane is measured by comparing the average y position of each sphere to the midpoint between the boundaries. The dipole-dipole interactions are calculated up to a cutoff distance of 8σ. Membrane energy is normalized by the number of particles, N = 1904. The molecular dynamics simulations use the open source package LAMMPS [35] and visualized with VMD [36].

2.2.2. Continuum Elastic Model

The continuum elastic model was formulated and solved numerically by Prof. Mykola Tasinkevych (U. Lisbon). The details can be found in our paper [37], but we will briefly describe it here. The membrane is represented by a 2-D surface passing thought the centers of the superparamagnetic particles The undeformed conformation is a flat square with area $A_0 = L_0^2$. The location of each particle is triangularized using the BL2D mesh generator [38]. The model takes the total free energy $\mathcal{F}$ of a magnetoelastic membrane as a sum of the stretching, $\mathcal{F}_s$, bending, $\mathcal{F}_b$, and magnetic, $\mathcal{F}_m$, terms. It is numerically minimized with respect to the in-plane stretching $\mathbf{u}(x, y)$ and vertical deformation $h(x, y)$ [39].

The magnetic energy in a fast precessing field implies that the colloidal displacement is much slower than the field precession period. As a result, we time-average the magnetic energy between nearest neighbors and obtain

$$\mathcal{F}_m = \frac{1}{2}\int_{S_{ref}} dS\ m(\theta)\left(\frac{2}{3} - g^{ij}(\mathbf{e_i}\cdot\hat{\mathbf{z}})(\mathbf{e_j}\cdot\hat{\mathbf{z}})\right), \tag{2.5}$$

where S is the surface, $\hat{\mathbf{z}}$ is the precession axis, and g^{ij} are components of the inverse of the metric tensor $g_{ij} = (\mathbf{e_i} \cdot \mathbf{e_j})$, and $\mathbf{e_i} \equiv \partial_\mathbf{i}\mathbf{X}$ are the membrane tangent vectors, dependent on the position vector $\mathbf{X}$. The last term needing definition is the magnetic modulus $m(\theta)$, which depends on the precession angle θ

$$m(\theta) = \frac{3\mu_0}{4\pi\Delta l}\left(\frac{\mu}{\Delta l^2}\right)^2 (3\cos^2\theta - 1), \tag{2.6}$$

where, μ is the magnitude of the magnetic dipoles and Δl is the particle bond separation.

The elastic contributions are a sum of the in-plane stretching and out-of-plane bending terms. The stretching deformations are associated with the free energy cost

$$\mathcal{F}_s = \frac{1}{2}\int_{S_{ref}} d^2r\Big(2\mu u_{ij}u_{ji} + \lambda u_{kk}^2\Big), \tag{2.7}$$

where λ and μ are the 2-D Lamé coefficients, the strain tensor $u_{ij} = \frac{1}{2}\Big(\partial_i u_j + \partial_j u_i + (\partial_i u_k)(\partial_j u_k) + (\partial_i h)(\partial_j h)\Big)$, $h(x, y)$ is the height over the reference plane. The bending free energy, $\mathcal{F}_b$, of a membrane may be expressed in terms of its twice mean curvature H Gaussian curvature K:

$$\mathcal{F}_b = \int_{S_{ref}} dS\Big(\frac{1}{2}\kappa H^2 + \kappa_G K\Big), \tag{2.8}$$

where dS is the area element, κ and κ_G are the bending and Gaussian rigidities, respectively. We set $\lambda = \mu$, and $\kappa_G = -\kappa$ [40]. This implies that the 2-D Young's modulus is $2\epsilon/\sqrt{3}$, where ϵ is the microscopic stretching constant, and the bending rigidity is $\sqrt{3}\widetilde{\kappa}/2$, where $\widetilde{\kappa}$ is the microscopic bending constant.

2.2.3. Analytical Solution of Unstretchable Magnetoelastic Membrane

Two analytical solutions of a continuum model were found by Prof. Pablo Vázquez-Montejo (U. Autónoma de Yucatán). Like in the previous section, the details can be found in our paper [37], but we will briefly describe it here. The membrane is parametrized by its arc length l and can be determine by a 2-D profile curve [41] described in Cartisian coordinates $\mathbf{X}(x,l) = x\hat{\mathbf{x}} + y(l)\hat{\mathbf{y}} + z(l)\hat{\mathbf{z}}$, see Fig. 2.7. The total energy of the membrane is given by $H = L\int dl\mathscr{H}$, where

$$\begin{aligned} \mathscr{H} &= \frac{1}{2}\left(\kappa\dot{\Theta}^2 - \mathrm{m}\cos^2\Theta\right) \\ &- F_y(\dot{y} - \sin\Theta) - F_z(\dot{z} - \cos\Theta)\,, \end{aligned} \tag{2.9}$$

where κ and m are the bending and magnetic moduli; F_y and F_z are Lagrange multipliers and are found to be constants [42, 43]. The resulting quadrature for Θ is

$$\frac{1}{2}\left(\mathrm{k}\,\dot{\Theta}^2 + \mathrm{m}\cos^2\Theta\right) - F_y\sin\Theta - F_z\cos\Theta = c\,, \tag{2.10}$$

where c is a constant of integration. In order to solve Eq. (2.10), appropriate boundary conditions must be determined and are described in our publication [37]. The first solution results from assuming left-right symmetry and implies that the force is directed along the Y axis, $F = F_y$ and $F_z = 0$. The profiles obtained from these contions are shown in Fig. 2.6. For a finite vertical force, $F_z \neq 0$, Eq. (2.10) becomes asymmetric as seen in Fig. 2.5.

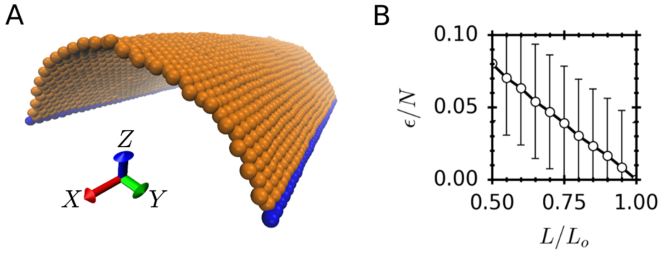

Figure 2.2. Effect of boundary separation on an elastic membrane with no external field ($\gamma = 0$). (A) Under a uniform compression ($L/L_o = 0.8$) on opposite, stiff boundaries (blue), the strain related to the in-plane deformations is released via a buckling transition where the membrane adopts a symmetric arch shape. The edges that define the boundary separation are colored blue. (B) Total membrane energy obtained from molecular dynamics (MD) simulations as the distance, L, between opposite boundaries changes. The total membrane energy (in units of kT) is normalized to the total number of colloids, N. The colloids are modeled as 10 nm particles under room temperature.

2.3. Results and Discussion

2.3.1. Magnetoelastic membranes under linear compression

In order to understand the affect of a precessing field on the linear compression of a magnetic membrane, we first must understand the case for a purely elastic membrane. When two stiff boundaries of a square membrane are brought together, the adjacent flexible boundaries will bend to relieve the relatively high energetic cost of in-plane elastic deformation and the equilibrium state is a single arch (Fig. 2.2A). The energy curve is proportional to the membrane curvature and decreases linearly until reaching its smallest value at $L = L_o$ (Fig. 2.2B). The total membrane energy is therefore dominated by bending interactions, with negligible changes in stretching or self-interaction (Fig. 2.3, top). Therefore, there is constant bending force acting on the boundaries of a compressed

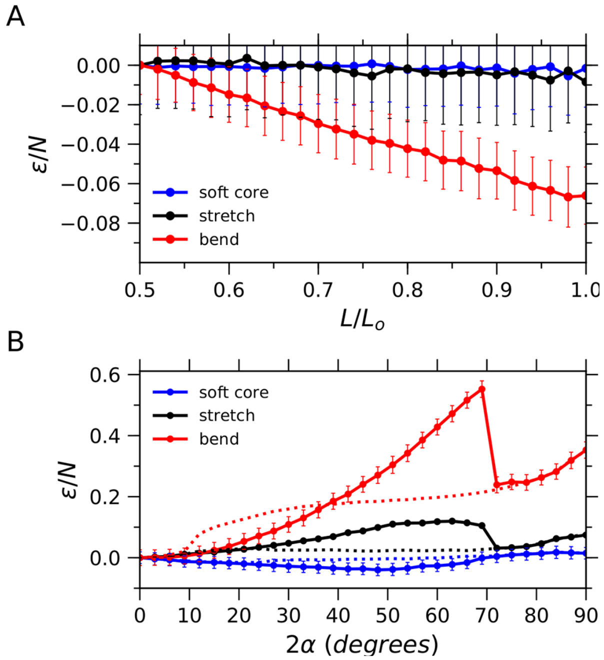

Figure 2.3. Shifted components of the total membrane energy in the absence of a magnetic field: bending energy, stretching energy, and soft core particle repulsion (Weeks-Chandler-Anderson force) for (A) membrane boundary separation and (B) twisting.

membrane that drive it to expand flat. If allowed to move freely, the blue boundaries in Fig. 2.2A would move apart ($L \rightarrow L_o$).

In a precessing magnetic field, the direction of force (expansion or contraction) on the membrane's boundaries depends on the sign of γ. Under small-angle precession ($\gamma > 0$, $\theta < \theta^*$), a membrane, with any initial amount of compression, contracts when the boundaries move together (Fig. 2.4A). Contraction of the boundaries only occurs if the field strength is sufficient to overcome the penalty of bending. When this requirement is met, the force pulling the boundaries together increases with field strength. As contraction proceeds, the force on the boundaries decreases and approaches zero. The energy curves from MD simulations match closely with those from CM calculations (Fig. 2.4C). For moderate field strengths, an instability appears on the energy curve ($\gamma = 150$ and 300) where the free edges of the single-arch membrane buckle towards the center due to the favorable alignment of the dipoles, leading to a "double-buckled" configuration. This transition is also predicted by our CM calculations for weak-to-moderate field strengths ($\gamma = 100$ and 200). These mark the transition point at which the energy branches of the single-arch and double-buckled membranes intersect and is dependent on the boundary separation L/L_o and γ (Fig. 2.4D). Our MD simulations observe this transition around $L/L_o = 0.65 - 0.80$. Larger values of L favor the double-buckled membrane, while smaller values of L favor the single-arch membrane. In order for the flexible boundaries to buckle inwards, the stiff boundaries must be sufficiently spaced so that the increase in bending energy is offset by the recovery of magnetic energy. Increasing γ lowers the value of L needed to induce the buckling transition. For $\gamma > 300$, we observe only the double-buckled configurations in the range of $0.5 < L/L_o < 1.0$.

While the mirror symmetry of the membrane across the Y axis is preserved in the $\gamma > 0$ case, the symmetry across the $X - Z$ plane at the midpoint between the stiff boundaries is broken under large-angle precession ($\gamma < 0$, $\theta > \theta^*$) and large compressions. These conditions lead to an asymmetric arch membrane configuration shown in Fig. 2.4D predicted by CM calculations and MD simulations. Similar transitions have been previously described in non-magnetic systems where elastic membranes are deformed on a solid or liquid substrate [44–46]. The asymmetric arch allows the membrane to significantly reduce the force driving expansion (Fig. 2.4B), with a similar force reduction in CM calculations (Fig. 2.4C), and corresponds to the small L branch of the membrane energy. At larger L, we observe the symmetric arch configurations which exhibit a larger expansion force. Unlike in the case of the small-angle precession, the membrane does not reveal a secondary buckling transition. Rather, it possesses a continuous flattening in the $X - Y$ plane as the field strength increases.

At a given level of membrane compression, MD simulations predicts a critical field strength above which the membrane adopts an asymmetric arch shape. The cross-over between asymmetric and symmetric configurations is reported in Fig 2.5A. As compression increases, the asymmetric configuration becomes more favorable and the minimum magnetic field strength required to induce the symmetric-to-asymmetric transition decreases. Of course, as L approaches L_o, the field strength needed to distort the membrane increases rapidly.

We develop analytical solutions that predict this spontaneous symmetry breaking. The membrane is assumed to be translationally invariant in the X direction. This assumptions is justified in the limit of small compression and weak to moderate strength of the magnetic field. In this regime, the membrane shape is described by a profile curve which we parametrize by the angle $\Theta(l)$ that the local tangent vector $\mathbf{e}_l$ makes with the precession axis, where l is the arc length along the membrane profile curve (Fig 2.7). This analysis yields the total energy of the membrane given by $H = L_o \int dl \mathscr{H}$, where the linear energy density $\mathscr{H}$ coincides with the energy density of a paramagnetic filament [41]. The Euler-Lagrange equations arising from $\mathscr{H}$ lead to the profile curves of the ground state. Symmetric solutions correspond to zero vertical force on the membrane, whereas for a finite vertical force the potential in quadrature $\mathscr{H}$ becomes asymmetric. This asymmetry is a property inherited by the corresponding solutions (Fig 2.5B).

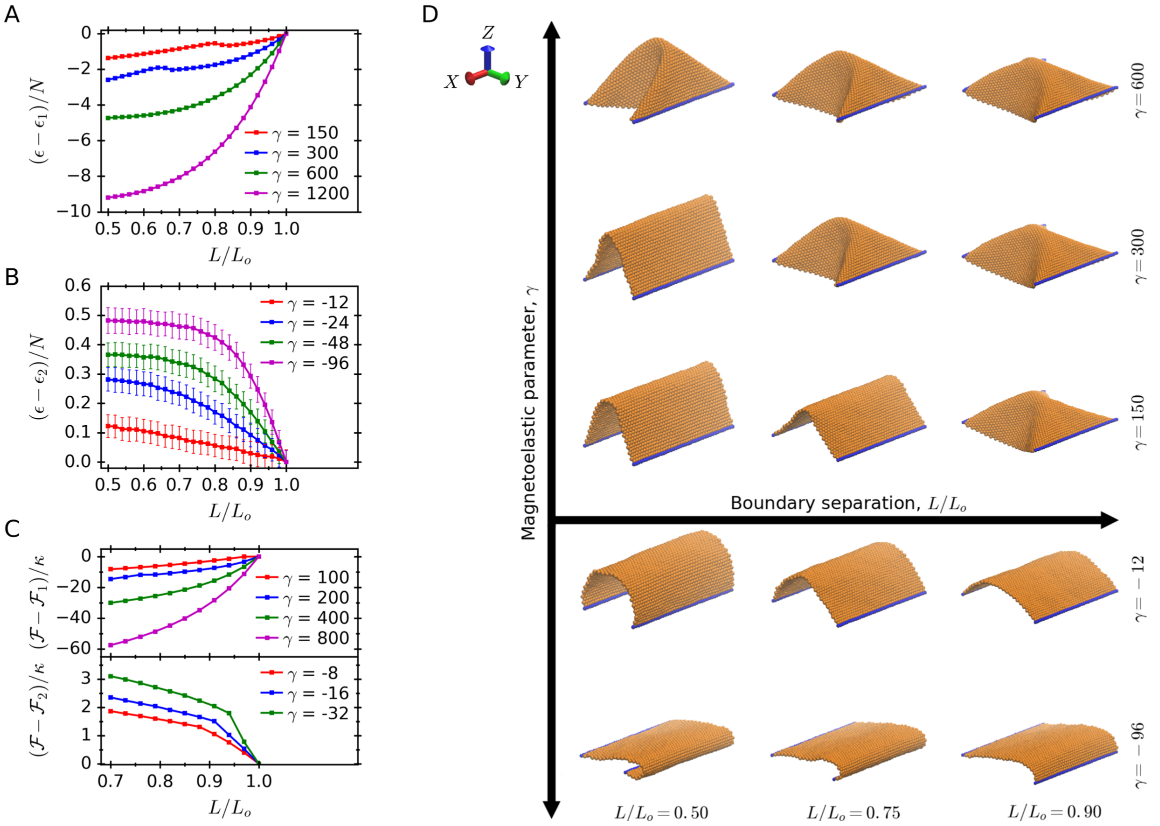

Figure 2.4. Influence of boundary separation on magnetoelastic membranes. Total membrane energy as a function of L obtained via MD simulations. The results show membrane contraction under (A) small-angle magnetic field precession ($\gamma > 0$) and expansion under (B) large-angle precession ($\gamma < 0$). Curves are shifted by the value of the energy (in units of kT) at $L/L_o = 1$, ϵ_i, for clarity and normalized by the number of colloids, N. (C) Calculated membrane total free energy $\mathcal{F}$ from continuum mechanics with $\gamma > 0$ and $\gamma < 0$. Free energy curves are shifted by $\mathcal{F}_i, i = 1, 2$, the values at $L/L_o = 1$, for clarity and normalized to the bending modulus. (D) Snapshots of membrane configurations at boundary separation $L/L_o =$ 0.5, 0.75, and 0.90 ($2\alpha = 0$) at under different values of γ. Field precession at $\theta < \theta^*$ causes secondary buckling of the free membrane edges which is reflected by the brake in the slope of the free energy curves at $\gamma = 150$ and 300. The edges that define the boundary separation are colored blue.

2.3.2. Torque on a magnetoelastic membranes

In addition to linear forces, a contracting and expanding magnetoelastic membrane experiences torque on its boundaries. Twisting an elastic membrane at zero external field is disfavored due to the build-up of elastic stress. Rather than changing compression, we rotate the two stiff boundaries in opposite directions by an angle α for a total angle of 2α. The rotation occurs along a centerline drawn along the Y axis that extends through the center of each stiff boundary. Starting from $2\alpha = 0$, we twist the membrane by rotating the boundaries to $2\alpha = 90^\circ$ and then reverse the direction of rotation back to the parallel state. We observe hysteresis in the $\epsilon(\alpha)$ curve (Fig. 2.8A). Twisting membrane edges beyond $2\alpha \simeq 70^\circ$ from lower angles induces a configurational transformation to relieve elastic and bending energy localized in two opposite corners of the membrane (Fig. 2.8B). Further twisting concentrates elastic stress at a single point near the center of the membrane. This conformation persists until the boundaries are rotated close to a parallel position (18°) where the membrane transitions back to a symmetric arch. This transformation also leads to a drop in membrane stretching and bending energies (Fig. 2.3B).

In the case of membrane twisting under a precessing magnetic field, the conformation depends on the magnitude and sign of γ. MD simulations highlight different regimes for magnetically-induced changes in the membrane configuration that correspond to changes in the torque on the stiff membrane boundaries. Under small-angle precession ($\gamma > 0$) and relatively weak fields, the $\epsilon(\alpha)$ curves reveal a hysteresis in the membrane energy (see blue and red curves in Fig. 2.9A). Twisting the boundaries from 0° to 90° causes the

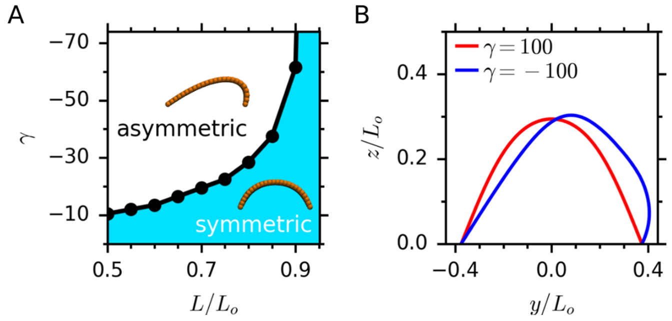

Figure 2.5. Application of magnetic field breaks membrane symmetry. (A) MD simulation data for the transition between symmetric and asymmetric membrane configurations as a function of γ and L/L_0. Above the critical values of $|\gamma|$, only asymmetric configuration exists. (B) Membrane profiles found by analytical methods for $\gamma = 100$ and -100 ($L/L_o = 0.75$).

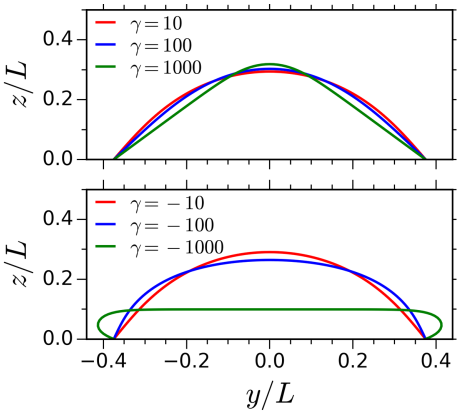

Figure 2.6. Profile curves for the symmetrical ($F_z = 0$) analytical solutions to a magnetoelastic membrane at various positive and negative values of γ.

membrane to undergo two configurational transitions. The reverse path results in a single transition back to the original, single-arch state.

From 0° to 90°, the increase in the free energy of the membrane begins with an unfavorable increase in the dipole-dipole energy (Fig. 2.10). Therefore, the buckling transition at $25° - 33°$,where the center of the single-arch buckles inward, is driven by the magnetic field (Fig. 2.9D). After this point, there is a build-up of elastic stress along a

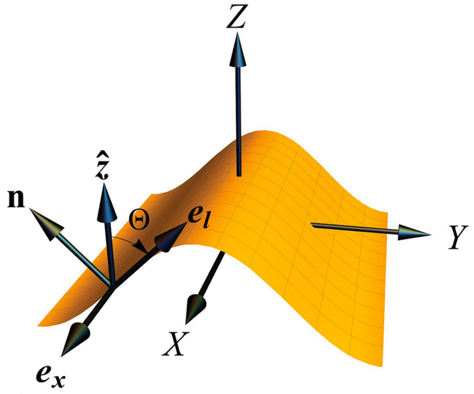

Figure 2.7. Schematic drawing of a membrane showing the angle Θ that the local tangent vector $\mathbf{e}_l$ makes with the precession axis Z. The membrane edges which are parallel to the X axis are fixed.

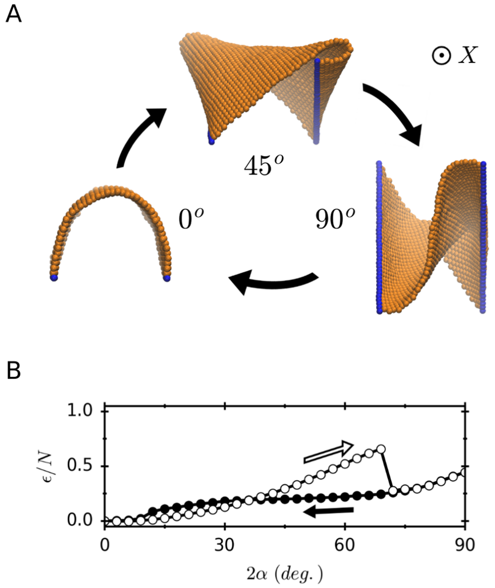

Figure 2.8. Effect of boundary rotation on an elastic membrane with no external field ($\gamma = 0$). (A) Total membrane energy (in units of kT) normalized by the number of colloids, N obtained from molecular dynamics (MD) simulations as the total angle, 2α, between boundaries changes with constant separation ($L/L_o = 0.5$). (B) MD simulated membranes show the conformational transition as the angle between stiff, separated boundaries (blue) increases (images represent $2\alpha = 0, 45°, 90°$, respectively). The membrane undergoes a conformational transition at some threshold value of $2\alpha \simeq 70°$ to relieve accumulated stretching strain causing the formation of a hysteresis.

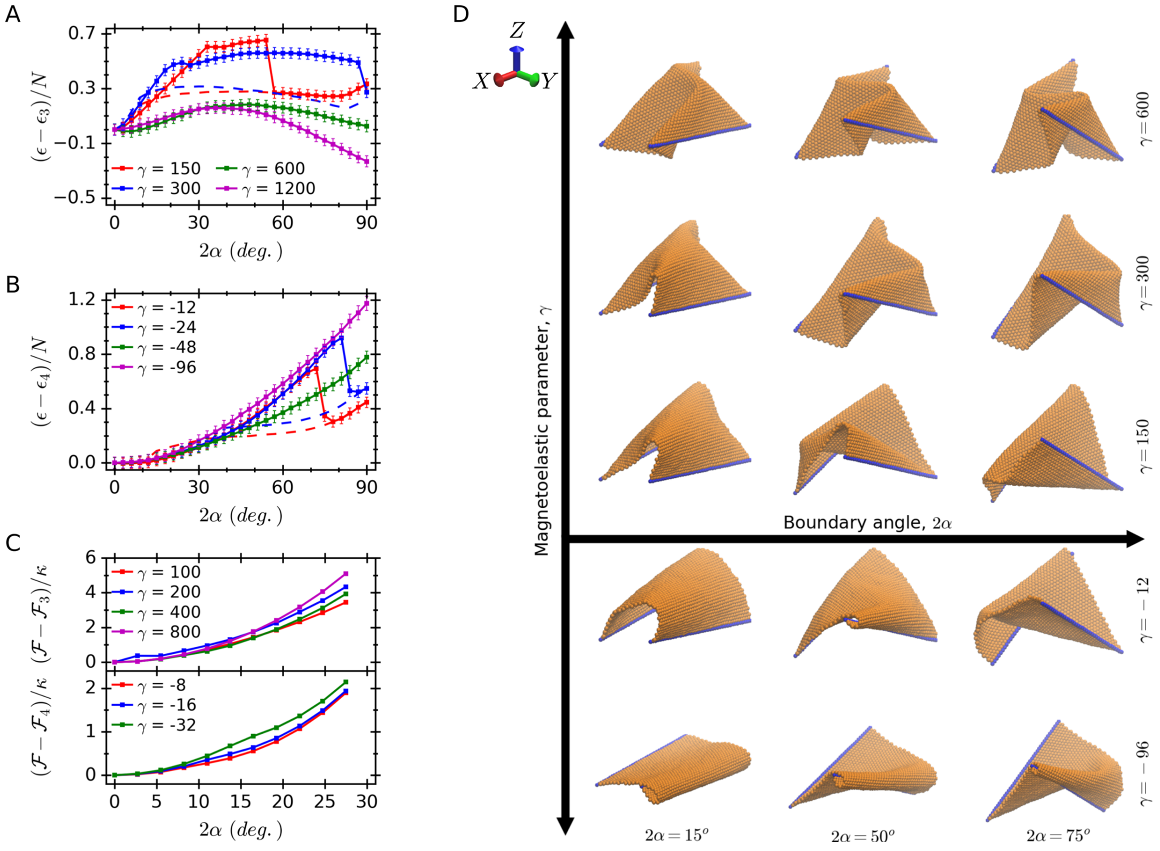

Figure 2.9. Influence of boundary rotation on magnetoelastic membranes. MD simulations results for membrane energy as a function of 2α, the twisting angle of two opposite membrane edges, at $L/L_0 = 0.5$, and for several values of (A) $\gamma > 0$ and (B) $\gamma < 0$. Membranes resist twisting at small 2α under small-angle magnetic field precession ($\gamma > 0$) and for all rotation angles under large-angle precession ($\gamma < 0$). The solid lines represent rotation from $2\alpha = 0$ to $2\alpha = 90°$ and the dashed lines represent the reverse path back to $2\alpha = 0$. There exists a threshold value of γ above which the hysteresis from rotation disappears, green and magenta curves. Curves are shifted by the value of the energy (in units of kT) at $2\alpha = 0$, ϵ_i, for clarity and normalized by the number of colloids, N. Energy is given in the Lennard-Jones units. (C) Membrane free energies from CM calculations as a function of 2α for $\gamma > 0$ and $\gamma < 0$. Free energy curves are shifted by $\mathcal{F}_i$, the free energy values at $2\alpha = 0$, for clarity and normalized to the bending modulus. (D) Snapshots of the membrane configurations at $\alpha = 0, 45°, 90°$, respectively, under different values of γ ($L/L_o = 0.5$). The edges that define the boundary separation are colored blue.

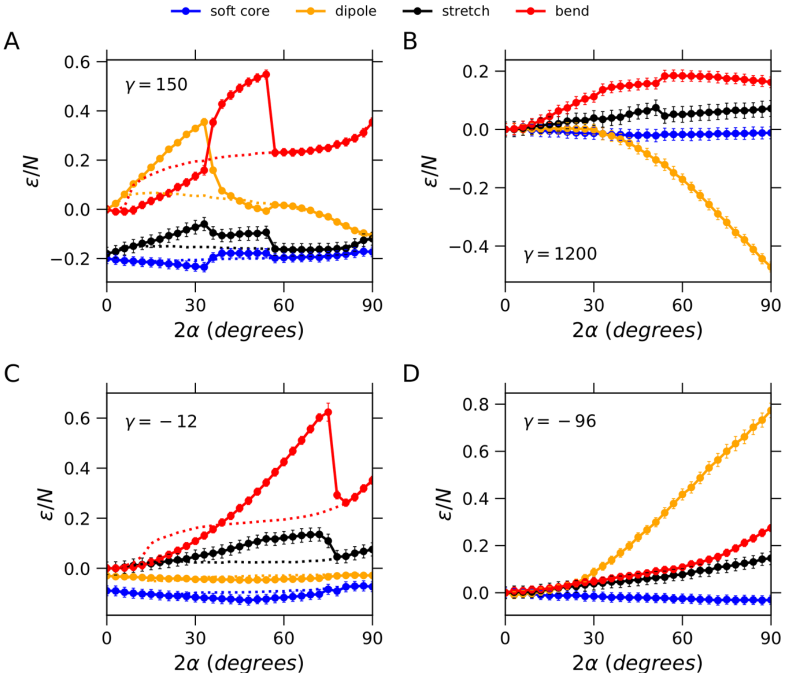

Figure 2.10. Components of the total membrane energy in the presence of a magnetic field: dipole interaction energy, bending energy, stretching energy, and soft core particle repulsion for (A) $\gamma = 150$, (B) $\gamma = 1200$, (C) $\gamma = -12$, and (D) $\gamma = -96$. For clarity, energy curves are shifted and error bars on reverse curves are omitted.

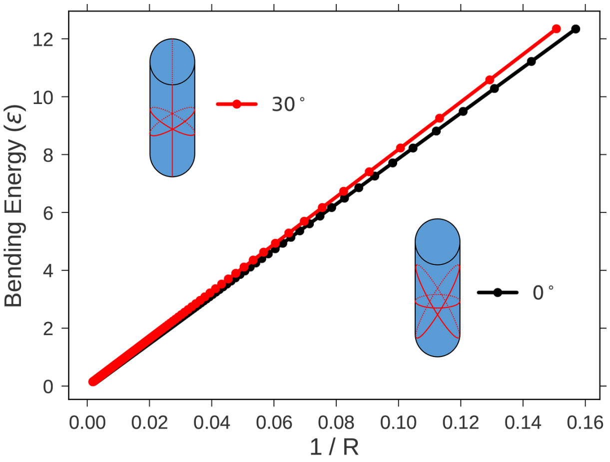

Figure 2.11. Numerical calculations for the total bending energy of a membrane with three bending axes at various curvatures. We fit the continuum bending constant, $\kappa_{real} \approx 26$, to this line, $E = \pi\kappa_{real}/R$.

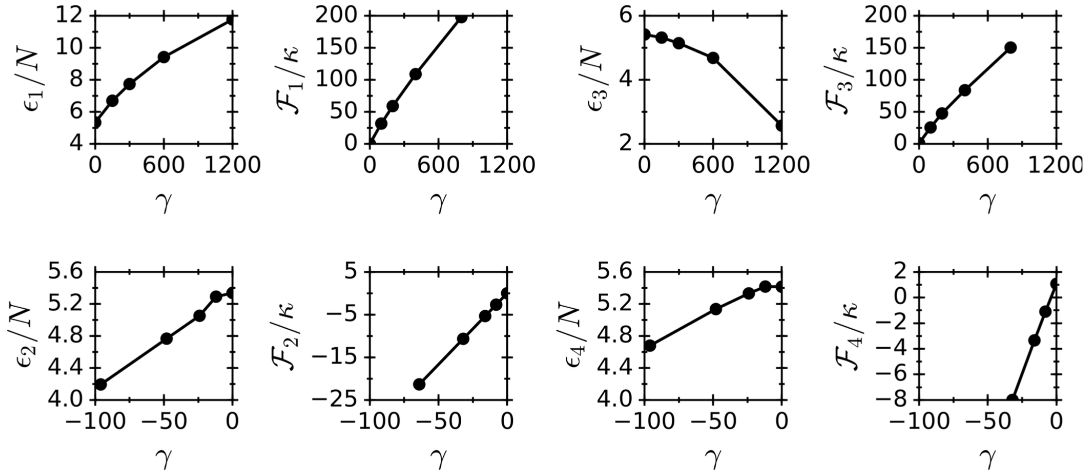

Figure 2.12. Values for the shifted energy constants used in Figure 2.4 and 2.9 as a function of γ.

“V” shaped crease in the membrane. This leads to a second transition at larger angles (57° for $\gamma = 150$, 87° for $\gamma = 300$) back to a similar configuration as the single arch where the elastic stress is more distributed or, in the case of strong fields, concentrated along a line. We refer to this as an ”unbuckling” transition, where the membrane bending and stretching energy recovers from a magnetically-induced, buckled state. Unlike in the $\gamma = 0$ case, the weak field energy curves possesses local minima at intermediate angles, around 80°. Above a threshold value of $\gamma > 300$, the free edges of the membrane buckle inwards (Fig. 2.9D) and adopts a “S” shaped configuration, which eliminates the membrane energy hysteresis. In this regime, the membrane configuration is dominated by magnetic interactions and, above $\gamma > 600$, it has a global energy minimum at the most twisted state.

For large-angle precession ($\gamma < 0$), we also observe a hysteresis in the $\epsilon(\alpha)$ curves under weak fields (Fig. 2.9B). Small $|\gamma|$ ($< |-24|$) result in a similar transition as the purely elastic case with differences in the angle at which the membrane unbuckles, 78°, before transitioning back to a single-arch. MD simulations show that the combination of larger $|\gamma|$ and boundary rotation exacerbates the bending energy penalty while the membrane tries to flatten against the boundaries (Fig. 2.9D) and locks-in a "loop" on one side of the membrane formed from the asymmetric arch. The hysteresis loop is not present for $\gamma < -24$ because of this kinetically locked state. Whether this state is present or not, $\gamma < 0$ disfavors a twisted membrane. CM solutions predict that, in general, as $|\gamma|$ increases, the force keeping the boundaries parallel increases (Fig 2.9C).

Finally, in Fig. 2.12, we discuss how the reference values for the shift in the energy curves in Figures 2.4 and 2.9 highlight changes in membrane buckling. We see that the MD simulations show changes in the slope of the ε curve corresponding to buckling event in the membrane. For instance, the kink in ε_2 occurs when we expect the formation of the asymmetric membrane conformation. We also observe a negative slope in ε_3 (MD simulations) rather than a positive slope for the CM model. This indicates that Gaussian curvature is playing a significant role in decreasing, rather than, increasing the membrane energy. This complex 3-D buckling is significant and must be carefully considered when designing magnetoelastic membrane systems.

2.4. Conclusions

We show that the magnetoelastic parameter γ controls the configuration and defines the configurational transitions of magnetoelastic membranes. By changing γ through the magnetic modulus, m, the actuation of a magnetoelastic membrane can be controlled. For $\gamma > 0$, a flat membrane with rigid, parallel boundaries contracts. If the sign of γ is flipped ($\gamma < 0$), the membrane expands to its original flat configuration. However, applying a field such that $\gamma \gg 1$, a flat membrane twists as it contracts and remains in the twisted state until γ decreases. Thus far, switching between a flat and twisted structure has been observed by altering the chemical environment [47] or intrinsic structure [48, 49] of polypeptide beta-sheets. We show that magnetoelastic membranes can switch between these two morphologies rapidly using external magnetic fields without the challenge of changing a membrane's mechanical or chemical environment.

The CM calculations agree with the predictions of MD simulations for the configurations and configurational transitions driven by membrane compression at $\alpha = 0$. In addition, the analytical solutions to the continuum model constructed here for unstretchable membranes are similarly valid under weak magnetic fields. Now that we have validated these MD simulations with theoretical predictions, we set the stage for addressing dynamical aspects of magnetoelastic membrane behavior in the regime of slow precessing fields.

CHAPTER 3

Magnetoelastic Membrane swimmers

3.1. Introduction

Magnetically controlled microrobots have applications in drug delivery [50–53], sensing [54–56], micromixing [57], detoxification [58, 59], and microsurgery [60, 61]. Such versatile use of magnetic microrobots is possible because magnetic fields can penetrate organic matter, do not interfere with biological or chemical functions, can replace chemical fuels that drive robotic actuation, and, most importantly, can be externally controlled. These properties allow for non-invasive and precise spatiotemporal execution of desired

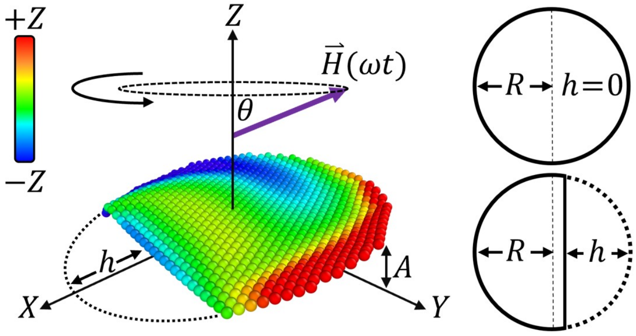

Figure 3.1. An image of a truncated magnetoelastic membrane in a precessing magnetic field. The degree of truncation $S = h/2R$, where h is the sagitta length of the removed circular segment, and R is the membrane radius, determines membrane symmetry. The magnetic field $\vec{\boldsymbol{H}}$ precesses at the angle θ around the z axis with a phase given by $\phi = \omega t$, where ω is the precession frequency and t is time. The field induces a transverse wave along the membrane perimeter with amplitude A, measured from the x-y plane. Coloration indicates z position as shown by the color bar on the left.

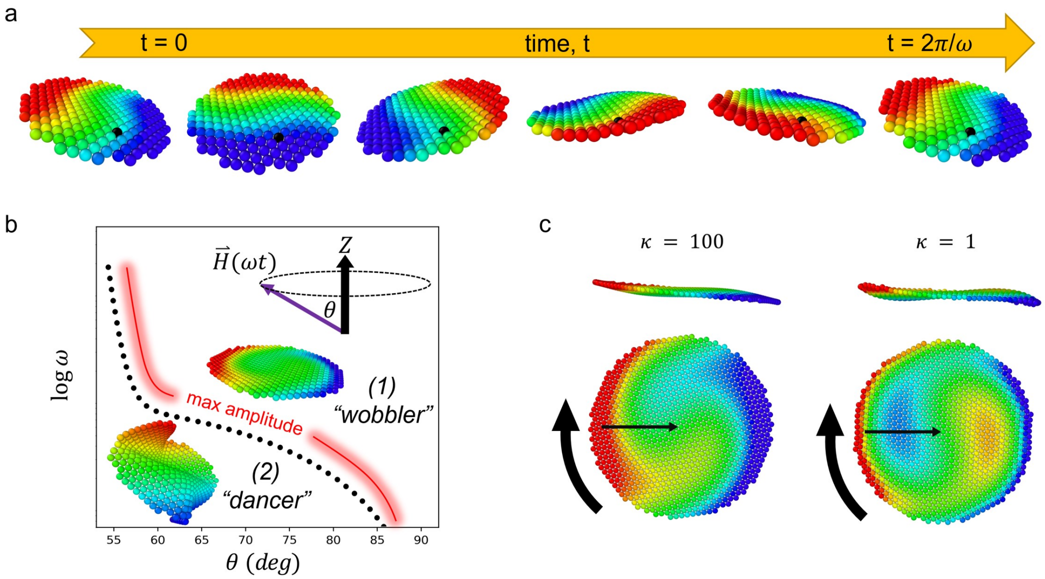

Figure 3.2. A circular magnetoelastic membrane in a precessing magnetic field. (a) Transverse waves propagate around the membrane above a critical frequency ($\omega > \omega_c$) with negligible membrane rotation, highlighted by the black colored colloid. Coloration indicates z position as shown by the color bar in the top right corner. (b) A schematic plot showing the phase diagram of a membrane. Above the dotted black curve, the 'wobbling' membrane remains perpendicular to the precession axis and possess the rotational waves from (a). The wave amplitude maximizes just before the transition. Below this curve, the membrane buckles and rotates asynchronously with the field, hence 'dancers'. (c) The bending stiffness controls the shape of the rotational waves. The black arrows indicate the direction of wave propagation along the perimeter (thick arrow) and radially toward the membrane center (thin arrow).

function. Superparamagnetic particles, in particular, are ideal candidates for robotic functions because they lack residual magnetization, which lowers their propensity to agglomerate, and they are less toxic than ferromagnetic particles [62]. When linked along a linear elastic chain, they form magnetoelastic filaments that bend and swim in response to time-dependent magnetic fields [21, 51]. While filaments possess a repertoire of possible actuating modes, magnetoelastic membranes [31, 37] combine the functionality of 1-D filaments, such as their high surface area-to-volume ratio and ability to swim, with the functionality of 3D magnetic gels, such as encapsulation and tunable porosity [63]. Using 2-D patterning methods, membranes possess unique shape-transforming properties that allow them to dynamically switch between functional states [4, 5], making membranes highly suited for designing multifunctional microrobots.

Non-reciprocal motion induced via competing magnetic and elastic interactions is required for microscopic, magnetoelastic robots to navigate viscous environments [6]. That is, the sequence of configurations that the robot adopts must break time-reversal symmetry to swim at low Reynolds numbers ($\mathrm{Re} = vL/\nu \ll 1$ where L and v are the length and speed of the robot, respectively, and ν is the kinematic viscosity of the fluid). Under these conditions, inertia is negligible. Hence, a microrobot in water experiences the same difficulty that a sardine may experience trying swim in peanut butter ($\mathrm{Re} \sim 10^{-3}$), that is, reciprocal back-and-forth motion will not produce swimming [64]. Magnetoelastic filaments achieve non-reciprocal motion with a non-homogeneous distribution of magnetic components or with shape asymmetry [51–53, 65, 66]. In these previous studies, asymmetries in magnetic filaments induce bending waves that propagate along the filament, resulting in propulsion.

In nature, microscopic organisms such as euglenids swim using self-propagating waves directed along their cellular membrane [67]. G. I. Taylor was the first to model such organisms using a transverse wave traveling along an infinite 2-D sheet [68]. Taylor found that the wave induced motion in the sheet opposite to the propagating wave direction.

Subsequent works expanded on Taylor's findings [69] and developed a rotational counterpart [70] that produces a hydrodynamic torque on circular membranes with prescribed waves traveling around their perimeter.

In this article, we study rotational waves in homogeneous magnetoelastic membranes under precessing magnetic fields. The membrane is composed of hexagonally-packed, superparamagnetic colloids that are bonded to their nearest neighbors. Similar to magnetoelastic filaments [55, 56], the bonding between colloids makes the membrane inextensible, but able to elastically bend. We investigate the dynamic modes of these membranes that are separated by a critical precession frequency ω_c, below which the membrane motion is asynchronous with the field, and above which rotational waves propagate in-phase with the field precession. Breaking the membrane's center of inversion symmetry, by removing part of the circle (Fig. 3.1), allows for locomotion in the fast frequency phase ($\omega > \omega_c$). Shape asymmetry is needed to disrupt the inversion symmetry of the magnetic forces experienced by a circular membrane. We show that the torque and velocity of the membrane counterintuitively resemble the linear Taylor sheet rather than its rotational analogue. Furthermore, by controlling a magnetoviscous parameter and the membrane shape asymmetry, we demonstrate swimming directed by a programmed magnetic field and diagram its non-reciprocal path through conformation space.

The paper is organized as follows. In Sec. II, we establish the phase diagram of a circular magnetoelatic membrane in a precessing magnetic field and determine the transition frequency ω_c. In Sec. III, we introduce hydrodynamic interactions and observe circular locomotion in asymmetric membranes. We demonstrate a programmed magnetic field, in Sec. IV, that directs a membrane swimmer along a predetermined path. Finally, we make concluding remarks on the necessary conditions for superparamagnetic swimmers in Sec. V.

3.2. Methods

3.2.1. Molecular dynamics model

We describe a membrane of radius R that is inextensible, but can bend in response to a dynamic magnetic field. The membrane is a monolayer of N hexagonally, close-packed magnetic colloids with diameter σ. Membrane flexibility is determined by the quadratic dihedral potentials between each colloid i and three of its nearest neighbors $U_{bend} = \frac{\kappa}{2}\sum_i^N \sum_j^n \varphi_j^2$, where κ is the bending rigidity, φ_j is the dihedral angle, and n is the number of dihedrals around i. The bending rigidity κ has units of energy and is scaled by the energy unit ϵ.

We model an implicit, uniform magnetic field by constraining the orientation of the colloids' dipole moments in the direction of the field, $\boldsymbol{H} = \boldsymbol{\mu}/\chi$, where χ is the magnetic susceptibility of the material and $\boldsymbol{\mu}$ is the dipole moment with magnitude μ. The instantaneous dipole orientation is $\hat{\boldsymbol{\mu}} = \sin\theta \sin\omega t \ \hat{\boldsymbol{\imath}} + \sin\theta \cos\omega t \ \hat{\boldsymbol{\jmath}} + \cos\theta \ \hat{\boldsymbol{k}}$, where θ is the field precession angle, ω is the precession frequency, and t is time. The timescale of the simulation is given in units of $t^* = \sigma\sqrt{m/\epsilon}$, where m is the mass of a colloid. We use the simulation time step $\Delta t = 10^{-3}\ t^*$.

The contribution of the dipole potential energy U_{dipole} to the total energy U is the sum of the dipole-dipole potential energy over all colloids. The dipole-dipole interaction is given by $U_{dipole} = \sum_i^N \sum_j^{N'} \frac{\mu_0 \mu^2}{4\pi r_{ij}^3}\left(1 - 3(\hat{\boldsymbol{\mu}} \cdot \hat{\boldsymbol{r}}_{ij})^2\right)$, where $\hat{\boldsymbol{r}}_{ij}$ is the displacement vector between colloids i and j. The total energy U is scaled by ϵ, and the dipole μ is reported in units of $\sqrt{\mu_0/4\pi\sigma^3\epsilon}$, where μ_0 is the magnetic permeability. The dipole-dipole interaction is cut off for all colloids $r_{ij} > 10\sigma$. Finally, the motion of the colloids are damped by a drag force, $-\xi v(t)$, proportional to the colloid velocity, $v(t)$, and the damping coefficient $\xi = 5 \times 10^2\ m/t^*$.

The dynamic states of the membrane were determined by calculating the total potential energy of the membrane over 10^2 precession periods. The transition frequency was determined to within an error of $\pm 10^{-3}$. The transition was confirmed by taking the Fourier transform of the beads position data over time, $\mathcal{F}[x(t)]$, $\mathcal{F}[y(t)]$, $\mathcal{F}[z(t)]$. The MD simulations were performed using LAMMPS [35] and snapshots of the membrane were visualized using the software OVITO [71].

3.2.2. The lattice Boltzmann method with immersed boundaries

Hydrodynamic interactions are coupled to the MD model using the lattice Boltzmann (LB) method [72]. This technique, which comes from a discretization of the Boltzmann transport equation, reproduces the incompressible Navier-Stokes equation in the macroscopic limit. The LB method calculates the evolution of a discrete-velocity distribution function f_i at each fluid node that fills the simulation box on a square lattice mesh with a spacing of Δx. The surface of the colloids act as a boundary and is defined by surface nodes that interact with the fluid using the model developed by Peskin [73].

Using the Bhatnagar-Gross-Krook collision operator [74], the LB equation becomes $f_i(\boldsymbol{x}+\boldsymbol{c}_i\Delta t, t+\Delta t) - f_i(\boldsymbol{x}, t) = -\frac{\Delta t}{\tau}(f_i(\boldsymbol{x}, t) - f_i^{eq}(\boldsymbol{x}, t)) + W_i$. The left-hand side describes the fluid streaming from one node to neighboring nodes along the velocity $\boldsymbol{c}_i$. The first term on the right hand side describes the relaxation of the distribution f_i to the equilibrium distribution f_i^{eq}, where τ is the relaxation time. The W_i term defines external forces on the fluid. These forces are distributed from nodes that define the surface of the colloids, $\sigma/2$ distance away from the particle center. These nodes interact with the fluid using the immersed boundary model developed by Peskin [73].

The fluid parameters are set to reproduce the frictional coefficient of a spherical colloid, which accurately reproduces the drag on a disk. The disk is immersed within a box of $112\times112\times113$ nodes. The spacing between nodes was set as $\Delta x = \sigma/2$ while the time step was set to match the MD simulations. Decreasing Reynolds numbers in a LB fluid can be achieved by choosing an increasing the lattice spacing Δx, increasing the time relaxation parameter or decreasing the Mach number, set by the speed of sound $c_s = \frac{1}{\sqrt{3}}\frac{\Delta x}{\Delta t}$ [75]. It is necessary to maintain resolution of the fluid circulation along the membrane edge and avoid numerical errors associated with increasing the relaxation parameter. Therefore, we rely on a small time step Δt that also integrates effectively with the harmonic potentials in the MD scheme to maintain $Re \ll 1$.

The "two-step" magnetic field was employed using a truncated membrane ($S = 0.48$). The temperature of the LB fluid was thermalized to 1 k_BT. [76] The first step ran for 21 precession periods with $S^{3/2}/(\tau\omega)^2 = 2 \times 10^{-2}$. The second step set the precession angle to $\pi/2$ and rotated the precession axis at a frequency $\omega/\omega_s \approx 10$ for roughly 1/3 the duration of the first step. Because the wobbling mode is stable, the flip does not need to lie perfectly in the x-y plane for the process to repeat effectively.

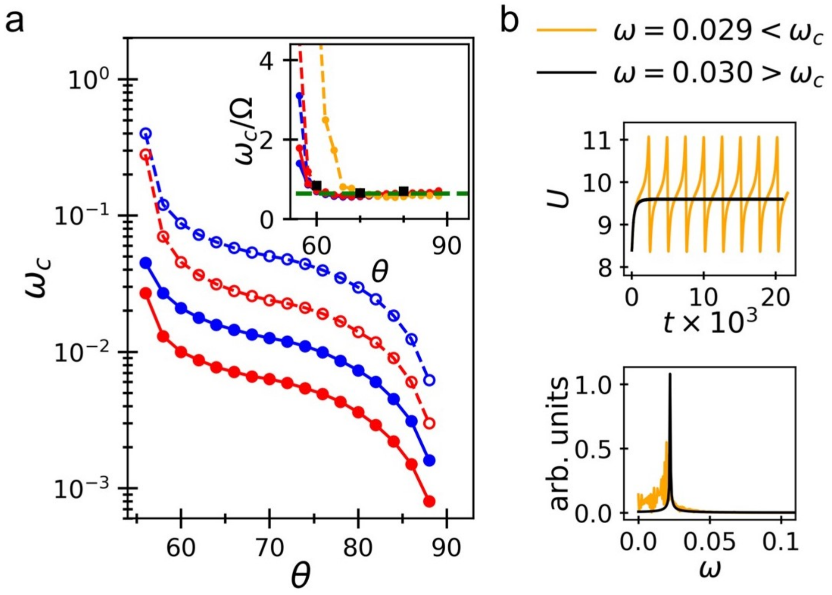

Figure 3.3. The synchronous-asynchronous (wobbler-dancer) transition frequency ω_c for a magnetoelastic membrane. (a) Molecular dynamics calculation of ω_c as a function of the field precession angle θ. The solid and dashed lines indicate a dipole magnitude of $\mu = 2$ and $\mu = 1$, respectively. The inset shows the dimensionless transition frequency ω_c/Ω, where Ω is the membrane's characteristic rotation frequency. The green-dashed line represents the theoretical transition at $\omega_c/\Omega = 2/\pi$, which, near $\theta = 90°$, is independent of bending stiffness ($\kappa = 1$, orange. $\kappa = 100$, blue/red). The black squares show the transition calculated from lattice-Boltzmann simulations. (b) Supercritical and subcritical behavior of the total energy U (magnetic + bending) in units of ϵ. The precession frequency is close to the critical frequency, $0.029 < \omega_c < 0.030$ ($\theta = 80°$). Fourier transform of the rotational wave amplitude (bottom).

3.3. Results and Discussion

3.3.1. Phases of a magnetoelastic membrane

We construct the phase diagram for the dynamic modes of the membrane using molecular dynamics (MD) without hydrodynamics to efficiently search for non-reciprocal actuation relevant to locomotion. Actuation of magnetoelastic membranes in time-dependent magnetic fields necessitates a model that captures elastic bending in response to magnetic forces, which are imparted by the dipolar interactions of embedded magnetic colloids. The membrane is composed of a hexagonal close-packed monolayer of hard spherical colloids, each of diameter σ and possessing a point dipole moment $\boldsymbol{\mu}$ at its center. The bonds between the colloids are approximately inextensible, but able to bend with rigidity κ. The energy scale for κ is given by the energy unit ϵ.

We model an implicit, uniform magnetic field by constraining the orientation of the colloids' dipole moments in the direction of the field, $\boldsymbol{H} = \boldsymbol{\mu}/\chi$, where χ is the magnetic susceptibility of the material and $\boldsymbol{\mu}$ is the dipole moment with magnitude μ. The instantaneous dipole orientation is given by $\hat{\boldsymbol{\mu}} = \sin\theta \sin\omega t \; \hat{\boldsymbol{\imath}} + \sin\theta \cos\omega t \; \hat{\boldsymbol{\jmath}} + \cos\theta \; \hat{\boldsymbol{k}}$, where θ is the field precession angle, ω is the precession frequency, and t is time. The scale for t and ω^{-1} is given in units of $t^* = \sigma\sqrt{m/\epsilon}$, where m is the mass of a colloid, and the dipole μ is reported in units of $\sqrt{\mu_0/4\pi\sigma^3\epsilon}$, where μ_0 is the magnetic permeability.

A diverse set of possible actuations develops depending on the radius R of the thin membrane and the magnetic field parameters (μ, θ, ω). While varying these parameters, we solve the equations of motion for an overdamped system with a friction force imparted on each colloid given by $-\xi\boldsymbol{v}(t)$, where $\boldsymbol{v}(t)$ is the colloid velocity, and ξ is the damping coefficient. See Appendix A for more details on the MD model.

Within this approximation, two dynamic mode regimes develop. At fast frequencies ($\omega > \omega_c$), the membrane motion synchronizes with the field to produce transverse waves that propagate around the membrane (Fig. 3.2a). We refer to these membranes as 'wobblers'. At slow frequencies ($\omega < \omega_c$), we observe a collection of modes that are asynchronous with the field resulting in membrane "dancers" that periodically buckle and spin. The actuation modes of these two regimes are separated by a critical frequency, ω_c (Fig. 3.2b).

As the field precesses, the forces along the membrane perimeter generate internal buckling and create a torque that rotates the membrane around its diameter. If the magnetic field precession is fast ($\omega > \omega_c$), the continuous change in the direction of the axis of rotation leads to the development of a constant-amplitude wave traveling along the membrane perimeter, see Video 1 in Ref. [77]. On average, the membrane remains perpendicular to the precession axis and simply 'wobbles', synchronous to the field, and with no significant rotation around the precession axis. This state closely resembles acoustically levitated granular rafts [78].

The direction of the propagating wave matches the handedness of precession because the dipole-dipole forces, which cause buckling, point in the direction of the magnetic field. However, the field polarity does not affect the magnitude or travel direction of the wave since the superparamagnetic dipoles are always oriented in the same direction as the field. Hence, the force due to the dipole-dipole interactions $\boldsymbol{F}_{dipole}$ remains unchanged ($\boldsymbol{F}_{dipole} \propto (\boldsymbol{\mu} \cdot \boldsymbol{r})\boldsymbol{\mu} = (-\boldsymbol{\mu} \cdot \boldsymbol{r})(-\boldsymbol{\mu})$, where $\boldsymbol{r}$ is the displacement vector between dipoles [79]).

In addition to the rotational waves, the wobbling mode also manifests radially propagating (inward) bending waves (Fig. 3.2c) that terminate at the membrane center. The wave shape weakly depends on the membrane stiffness κ; the wave form is better defined as κ decreases. However, totally compliant membranes ($\kappa \to 0$) do not transmit bending waves and therefore this phenomenon exists only for intermediate κ.

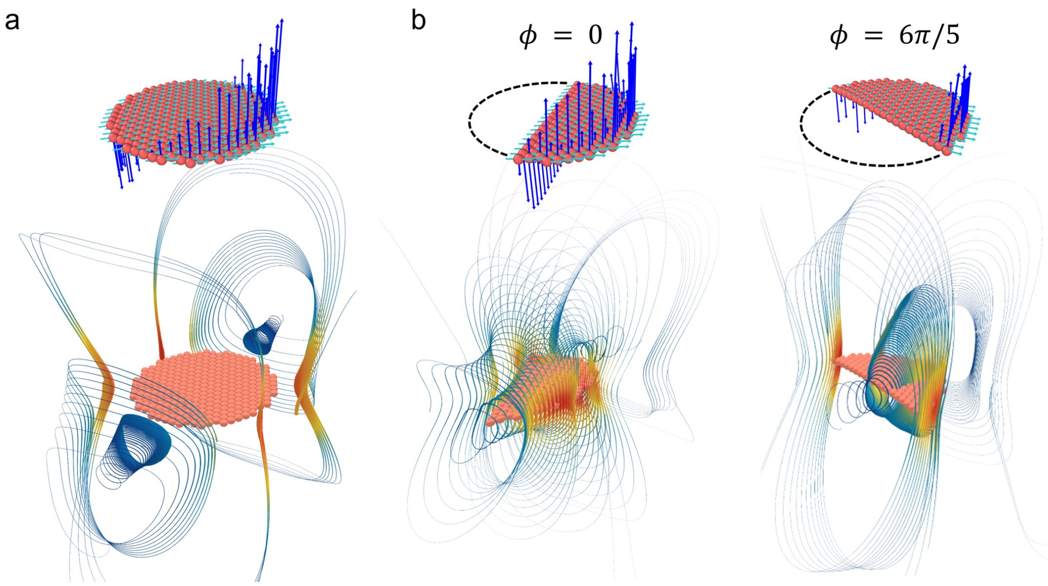

Figure 3.4. Fluid flow around a magnetoelastic membranes in the "wobbler" regime. The top images show the total force vector for each colloid (blue arrows) alongside the dipole orientation (cyan arrows) for a precessing field (μ =1, $\theta = 70°$, $\omega = 0.1$). The bottom images show streamlines around the membrane, where the color indicates flow speed u. (a) A snapshot of a circular membrane. (b) Two snapshots of a truncated circular membrane separated by a shift in the field precession $\Delta\phi = \omega t = 6\pi/5$.

If the precession is slow ($\omega < \omega_c$), the membrane has enough time to rotate completely parallel to the precession axis and will adopt new configurations due to elastic buckling. How the membrane buckles depends on the magnetoelastic parameter [31] $\Gamma = ML^2/\kappa$, which characterizes the ratio between the membrane's magnetic and bending energies, where M is the magnetic modulus, and L^2 is the membrane area. If the magnitude of Γ is very small ($\Gamma \ll 1$) or very large ($\Gamma \gg 1$), we observe hard disk behavior because bending distortions become impossible due to mechanical stiffness or due to unfavorable magnetic interactions, respectively. While not investigated here, strong magnetic coupling [80, 81] between colloids will adversely affect membrane synthesis.

At intermediate Γ, membrane edges buckle several times per precession period and produce magnetically stabilized conformations that, while periodic, run out-of-sync with the field, see Video 2 in Ref. [82]. Much of this back-and-forth "dancing" motion is essentially reciprocal and is therefore a poor candidate for studying swimming at small Re. Subsequently, we seek to formally define ω_c and focus on the wobbling regime ($\omega > \omega_c$).

To accurately determine the transition frequency ω_c that separates the wobblers from the dancers, we investigate how the magnetic field parameters (precession angle θ, dipole magnitude μ), and membrane radius R, in units of σ, (Fig. 3.3a) contribute to the characteristic response time τ of the rotating membrane. When the membrane rotation time τ increases, it necessarily requires a slower field to keep the membrane in the wobbling mode, decreasing ω_c. A larger τ, can be achieved by weakening the magnetic torque (θ closer to $\pi/2$ or smaller μ) or increasing the drag on the membrane (larger R). Similarly, a smaller τ implies a fast membrane response from a strong field or a small membrane. We observe that ω_c diverges as θ approaches the magic angle, partly due to instability of the wobbling phase at angles below the magic angle [83].

The transition to the wobbling state is characterized by the abrupt shift in the membrane's total potential energy U, given in units of ϵ, from a time-dependent function to a constant value (Fig. 3.3b, top). When the potential energy does not change, this implies that the shape of the membrane conformation becomes invariant in the rotating field reference frame. This change in the dynamic buckling results in a single Fourier mode for the displacement of the colloids parallel to the precession axis (Fig. 3.3b, bottom). This resembles the transition between the synchronous and asynchronous motion for oblate magnetic particles [83].

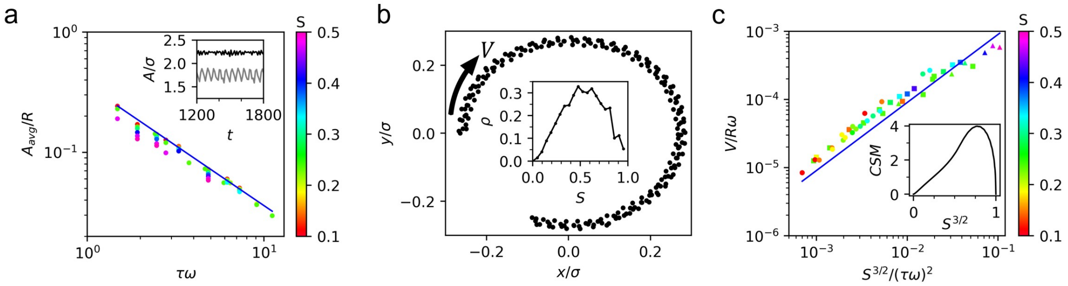

Figure 3.5. Actuation drives circular locomotion of truncated magnetoelastic membranes through a viscous fluid. (a) The average rotational (“wobble”) wave amplitude A_{avg}, scaled by the membrane radius R, depends inversely on the magnetoviscous parameter $\tau\omega$. Data points from lattice Boltzmann simulations are compared to our analytical model (solid blue line). The coloration of the simulation data notes the degree of truncation S. The inset shows the variation in A/σ over time based on membrane geometry ($S = 0.05$, black; $S = 0.5$, gray), where σ is the colloid diameter. (b) The path taken by a membrane in a precessing field. The arrow indicates the travel direction with velocity V. The inset shows the radius ρ of this path as a function of S. (c) The membrane velocity is proportional to $A_{avg}^2 \propto (\tau\omega)^{-2}$ and scales with $S^{3/2}$ due to changes in the length of the membrane perimeter. The data point shapes are coded by the membrane radius ($R = 7$, triangle; $R = 9$, square; $R = 12$, circle). The blue line shows our analytical prediction (slope = 1.0). The inset shows the continuous inversion symmetry measure for a flat truncated membrane.

Characteristic membrane frequency. When the precession angle approaches $\pi/2$, the membrane motion becomes independent of the stiffness of the membrane; the membrane remains flat at all times and for all values of ω. As the field precesses, the forces perpendicular to the membrane plane vanish near $\theta = \pi/2$ preventing significant radial bending and, consequently, changing κ does not shift ω_c (Fig. 3.3a, inset). In this large-angle limit, we can solving an Euler-Lagrange (EL) equation with Rayleigh dissipation (see Appendix B) to derive an equation of motion for a membrane. Doing so reveals a characteristic frequency of membrane motion.

Consider the membrane as a rigid disk of radius R and thickness σ moving in response to a magnetic field. The motion of the disk is synchronous to the field (similar to the rotational wobble of the classic Euler disk, but without surface friction). The disk's orientation is defined by the central normal vector on the face of the disk $\hat{\boldsymbol{n}} = -\sin\gamma\cos\omega t\,\hat{\mathbf{i}} + \sin\gamma\sin\omega t\,\hat{\mathbf{j}} + \cos\gamma\,\hat{\mathbf{k}}$ where γ is the angle of precession around the z axis for $\hat{\boldsymbol{n}}$. We find γ for the steady-state by solving the Euler-Lagrange (EL) equation with a velocity-dependent (Rayleigh) dissipation function [84]. For convenience, we define a second angle $\alpha(t)$ with respect to the x-y plane. This angle is formed by a vector $\hat{\boldsymbol{r}}_x$ that points along the x axis in the disk plane. From the equation for $\hat{\boldsymbol{n}}$, we get the relationship $\alpha(0) = \gamma$. The EL equation for the dynamics of the disk, using the degree of freedom $\alpha(t)$, is written as

$$\frac{d}{dt}\frac{\partial L}{\partial \dot{\alpha}} - \frac{\partial L}{\partial \alpha} + \frac{\partial P}{\partial \dot{\alpha}} = 0 \tag{3.1}$$

where $\alpha = \alpha(t)$, $\dot{\alpha} = d\alpha/dt$, P is the dissipation function, and L is the Lagrangian. The Lagrangian is defined as the difference $T - U$, where T is the kinetic energy, and U is the potential energy. Now we can expand Eq. 3.1 as

$$\frac{d}{dt}\frac{\partial T}{\partial \dot{\alpha}} - \frac{d}{dt}\frac{\partial U}{\partial \dot{\alpha}} - \frac{\partial T}{\partial \alpha} + \frac{\partial U}{\partial \alpha} + \frac{\partial P}{\partial \dot{\alpha}} = 0. \tag{3.2}$$

Since $\frac{\partial T}{\partial \alpha} = 0$ and angular acceleration is negligible when $\mathrm{Re} \ll 1$, we are left with

$$\frac{\partial U}{\partial \alpha} + \frac{\partial P}{\partial \dot{\alpha}} = 0. \tag{3.3}$$

We take P as the Rayleigh dissipation function defined as

$$P = \frac{1}{2}\sum_{i}^{N} \xi (y\dot{\alpha})^2, \tag{3.4}$$

where the sum is over all N colloids i in the disk, y is the distance from the rotation axis and $\xi = 3\pi\eta\sigma$, where η is the dynamic viscosity and σ is the colloid diameter. The sum over all colloids is given by the integral

$$P = \frac{2\xi}{\sigma^2}\int_0^R \int_0^{\sqrt{R^2-x^2}} (y\dot{\alpha})^2 dydx = \frac{3\pi^2\eta R^4}{4\sigma}\dot{\alpha}^2. \tag{3.5}$$

To calculate the total potential energy U, we only need to consider the contribution by the magnetic potential energy. For simplicity, we use a nearest neighbor approximation on a hexagonal lattice and sum the magnetic interactions over all colloids in the membrane.

$$U = \frac{\mu_0}{4\pi}\frac{\mu^2}{\sigma^3}\sum_{i}^{N}\sum_{j}^{n}(1 - 3(\hat{\boldsymbol{\mu}} \cdot \hat{\boldsymbol{r}})^2), \tag{3.6}$$

where the sum is over each colloid i in the disk of N colloids, for all n nearest neighbors indexed by j, μ_0 is the magnetic permeability of free space, μ is the dipole magnitude, and σ is the nearest neighbor distance. Each colloid on a hexagonal lattice has a set displacement vectors, $\hat{\boldsymbol{r}}$, that points toward its six nearest neighbors: $\hat{\boldsymbol{r}}_x = \pm(\sqrt{1-C_x^2}, 0, C_x)$, $\hat{\boldsymbol{r}}_{y1} = \pm(\frac{\sqrt{1-C_1^2}}{2}, \frac{\sqrt{3-3C_1^2}}{2}, C_1)$, $\hat{\boldsymbol{r}}_{y2} = \pm(\frac{\sqrt{1-C_2^2}}{2}, -\frac{\sqrt{3-3C_2^2}}{2}, C_2)$, where $C_x = -\tan\alpha$, $C_1 = -(\frac{1}{2} + \frac{\sqrt{3}}{2}\tan\omega t)\tan\alpha$, $C_2 = -(\frac{1}{2} - \frac{\sqrt{3}}{2}\tan\omega t)\tan\alpha$. We ignore a correction for the colloids along the perimeter by assuming $2\pi R/\pi R^2$ is small for large $R \gg \sigma$. Plugging in $\hat{\boldsymbol{\mu}}$ and the displacement vectors $\hat{\boldsymbol{r}}_i$, into Eq. 3.6, we expand U in a Taylor series to the first order about the point $\alpha = 0$ (the small wave amplitude regime) to yield

$$U = A_0 + \frac{9R^2\mu_0\mu^2 \sin 2\theta \sin \omega t}{2\sigma^5} \tan\alpha + \mathcal{O}(\alpha^2). \tag{3.7}$$

The lower order terms in A_0 are not dependent on α and therefore can be ignored. The accuracy of U can be increased by summing the contribution from dipole-dipole interactions between all colloids. While explicitly adding the contribution from second nearest neighbors, third and so on, is possible, doing so rapidly increases the complexity of U. Since the contribution to the potential energy decreases as $1/r^3$ on a regular lattice $\frac{1}{r^3}(1 + \frac{1}{2^3} + \frac{1}{3^3} + ...)$, the sum can be modified by the Riemann zeta function, $\zeta(3) \approx 1.202$. Therefore, to better approximate the full potential, we replace U with $U' = \zeta(3)U$.

Plugging U' and P into Eq. 3.3, we obtain

$$\dot{\alpha} + \Omega_l \sec^2\alpha \sin\omega t = 0, \tag{3.8}$$

where $\Omega_l = 6\zeta(3)\mu_0\mu^2 \sin 2\theta/\pi^2\sigma^4\eta R^2$ for a system with simple friction on each colloid. For a hydrodynamic system, the potential dissipation function $P = \frac{1}{2}\xi\dot{\beta}^2$ is taken to be consistent with the torque acting on a rotating disk in a viscous fluid, $\xi = \frac{32}{3}\eta R^3$. This changes the size scaling dependence to yield $\Omega_h = 27\zeta(3)\mu_0\mu^2 \sin 2\theta/64\sigma^5\eta R$. The inverse of Ω_h represents the timescale of the membrane's magnetoviscous response $\tau = 1/\Omega_h$ and is part of the magnetoviscous parameter $\tau\omega$. Solving Eq. 3.8 for α,

$$\frac{1}{2}(\alpha + \frac{\sin 2\alpha}{2}) = \frac{\Omega}{\omega}\cos\omega t + Z, \tag{3.9}$$

where $Z = 0$ using the boundary condition $\alpha = 0$ at $\omega t = -\pi/2$. The dynamic transition occurs at $\alpha \to \pi/2$ during the maximum possible amplitude over a field precession. During steady-state conditions this occurs at $\omega t = 0$. Doing so leads to a simple relation for the transition frequency

$$\frac{\omega_c}{\Omega} = \frac{2}{\pi}, \tag{3.10}$$

where $\Omega = 6\zeta(3)\mu_0\mu^2 \sin 2\theta/\pi^2\eta R^2\sigma^4$, where μ_0 is the magnetic permeability of free space, R is the radius of the membrane, η is the viscosity, and $\zeta(x)$ is the Riemann zeta function. The frequency Ω comes from the magnetic ($\propto \mu_0\mu^2 \sin 2\theta R^2/\sigma^5$) and drag ($\propto \eta R^4/\sigma$) potential functions. The ω_c curves in Fig. 3.3a can be scaled by Ω to obtain a dimensionless transition frequency $\omega_c/\Omega = 2/\pi$ (Fig. 3.3a, inset). This number predicts the mode of actuation of a membrane and defines the membrane response time $\tau = \Omega^{-1}$.

3.3.2. Hydrodynamics of membrane “wobblers”

The previous section investigates the broad range of actuating modes accessible to a magnetoelastic membrane. Using an overdamped system, we identify that membrane wobblers display non-reciprocal motion due to waves propagating around its perimeter. To study wobbler locomotion, we introduce hydrodynamic interactions using the lattice Boltzmann (LB) method [72] to confirm that the dancer-wobbler transition exists in a viscous fluid. We rewrite the EL equation using a hydrodynamic drag term for a disk ($\propto \eta R^3$), which modifies the characteristic frequency $\Omega = 27\zeta(3)\mu_0\mu^2 \sin 2\theta/64\eta R\sigma^5$. We will use this definition for Ω hereafter. Both the EL and the LB methods result in the same dimensionless transition ω_c/Ω (Fig. 3.3a, black squares).

The LB method reveals the effect of the wobbler's non-reciprocal motion on the surrounding fluid. This technique, which comes from a discretization of the Boltzmann transport equation, reproduces the incompressible Navier-Stokes equation in the macroscopic limit. The LB method calculates the evolution of a discrete-velocity distribution function f_i at each fluid node that fills the simulation box on a square lattice mesh with a spacing of Δx. The surface of the colloids acts as a boundary and is defined by surface nodes that interact with the fluid using the model developed by Peskin [73]. Care must be taken when implementing the LB method with MD because compliant springs can cause translation of the membrane due to in-plane stretching, which is a mechanism observed in systems of a few colloids [85]. See Appendix C for a complete description of the model.

The fluid flow around the membrane is determined by its symmetry and actuation. The wobbling mode circulates fluid around the membrane diameter in a similar manner to spinning disks [86]. However, the wobbler's axis of rotation moves continuously with the field, which produces an additional circulating flow in the x-y plane far above and below the membrane. For a circular membrane, the speed of the flow field possesses the same mirror symmetry as the forces that drive actuation (Fig. 3.4a).

The centrosymmetry of a circular membrane prevents its center of mass from translating. To induce locomotion, we truncate the membrane by removing a circular segment with a sagitta of length h (Fig. 3.1). We normalize h by the diameter of the circle to define the degree of truncation of the circular membranes as $S = h/2R$. In contrast with the circular membrane case, the shape of the fluid flow in the truncated membrane changes during a single precession period leading to asymmetric flow field that depends on the relative orientation between the field and the truncation cut (Fig. 3.4b).

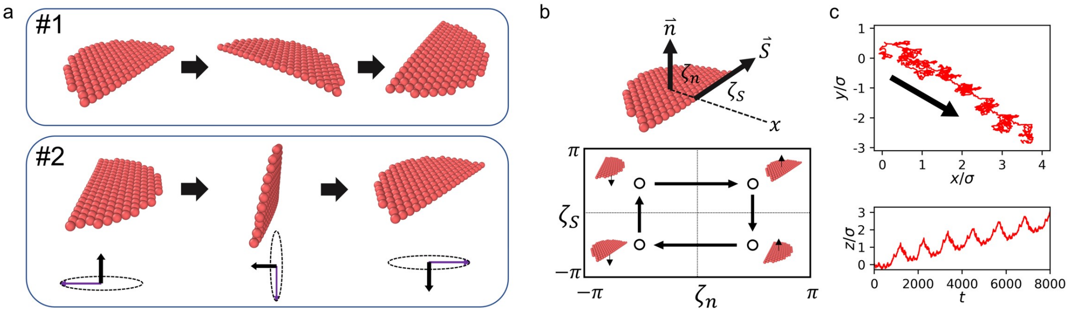

Figure 3.6. A two-step magnetic field directs a swimming membrane along a path. (a) First, a membrane wobbler moves under a precessing magnetic field. After it rotates a half-turn (#1), the precession switches to a fast frequency at $\theta = \pi/2$ while the axis rotates to flip the membrane (#2). (b) We define the angles that the normal vector $\boldsymbol{n}$ and the truncation vector $\boldsymbol{S}$ make with the x axis as ζ_n and ζ_S, respectively. (c) The path in conformation space over the two-step field. (c) Repeated cycles from (a) move the membrane against the Brownian motion of a thermalized fluid. The upper panel shows the motion of the membrane in the x-y plane. The black arrow indicates the direction of motion. The lower panel shows the displacement in the z direction.

The amplitude of propagating waves is particularly relevant for predicting the translational [68] or rotational [70] velocity of a membrane. Here, the wobble amplitude can be calculated by balancing the magnetic [79] and drag [86] torque in a viscous fluid. Consider a wobbling magnetoelastic membrane in the small amplitude limit. Under small distortions, the bending and stretching forces can be neglected. However, the flexibility of the membrane means that only a small area δa near the perimeter is in motion. Therefore, we consider Eq. 3.3 over δa moving freely along the z direction and write the drag term as the first order differential equation,

$$\frac{\partial P}{\partial \dot{z}} = 3\pi\eta\sigma\dot{z}\delta a. \tag{3.11}$$

Solving for z results in an oscillating function that reflects the periodic undulation in the membrane,

$$\frac{z}{R} = \frac{C \cos \omega t}{\tau \omega}, \tag{3.12}$$

where the equation is put in terms of $\tau = 1/\Omega$, and $C = 32/9\pi^2$. The amplitude is maximized $z_{max} = A$ when $\cos \omega t = 1$, From this equation, we see that the reduced amplitude of the rotational waves is inversely proportional to the magnetoviscous parameter. Under small amplitudes for the rotational wave, we obtain the simple relation

$$\frac{A}{R} = \frac{C}{\tau \omega} \tag{3.13}$$

where A is the amplitude, and $C = 32/9\pi^2$ (Fig. 3.5a). In the limit of small deformations, the bending contribution to the torque along the edge is negligible, unless $\kappa \to \infty$. Eq. 3.13 allows us to calculate the maximum flow speed $u_{max} = 4A/(2\pi/\omega)$ from Fig. 3.4, assuming no-slip boundaries.

The amplitude A is independent of the membrane size since $\tau \propto R$. However, the membrane is not free to increase in radius arbitrarily. The small Re condition implies that $\nu \gg R^2/\tau$, where ν is the kinematic viscosity. Obeying this constraint on τ, we can define a magnetoviscous parameter $\tau\omega$ and use it to predict locomotion.

Asymmetry in the fluid flow due to $S > 0$ leads to a membrane that travels with a net velocity in the direction of the truncation cut. This net motion is caused by the decrease in the amplitude of the waves traveling along the truncated edge. Since the truncated edge is closer to the center of mass and κ is homogeneous, the membrane will bend to a lesser extent along the truncation. This manifests as a net motion every $2\pi/\omega$, where reversing the handedness of the field reverses the locomotive direction.

While there is a net velocity along the truncation cut, rotation causes the membrane to follow a curved path. This rotation emerges exclusively due to the magnetic interactions perpendicular to the wobbling membrane. If the projection of the forces, visualized in Fig. 3.4, on the x-y plane is non-zero, the membrane will rotate. This rotation increases as ω approaches ω_c. Torque due to the underlying colloidal lattice is negligible. Over many precession periods, the membrane moves in a circular path around a central point (Fig. 3.5b). The radius ρ of the path depends on S and A_{avg}. Untruncated, $S = 0$, and fully truncated, $S = 1$, do not translate and result in $\rho = 0$. Hence, a maximum for ρ exists at intermediate S values (Fig. 3.5b inset). Since the membrane is composed of colloids, irregularities in the $\rho\left(S, A_{avg}\right)$ curve appear because the symmetry of the membrane changes in discrete steps as subsequent rows of colloids are removed with increasing S. In the limit $\sigma \to 0$, the plot of ρ vs. S would become smooth.

Membrane translation speed. The magnetic field controls how quickly the membrane travels along the circular path and affects its angular velocity. Together with the truncation S, the velocity V at which the membrane translates along the path can be determined using a singularity method. With a nearest-neighbors assumption for the magnetic interactions and treating them as point-disturbances, the advective flow through the center of mass can be calculated.

The fluid velocity at $\boldsymbol{x}$ is calculated by summing over all point disturbances [87]

$$\boldsymbol{v}(\boldsymbol{x}) = \frac{1}{8\pi\eta} \int \boldsymbol{G}(\boldsymbol{x} - \boldsymbol{y}) \cdot \boldsymbol{f}(\boldsymbol{y}) d\boldsymbol{y}, \tag{3.14}$$

where η is the dynamic viscosity, $\boldsymbol{f}(\boldsymbol{y})$ is a point force located at $\boldsymbol{y}$, $\boldsymbol{G}(\boldsymbol{r}) = \frac{\boldsymbol{I}}{|\boldsymbol{r}|} + \frac{\boldsymbol{rr}}{|\boldsymbol{r}|^3}$ is the Oseen tensor, and $\boldsymbol{I}$ is the identity matrix.

At every point on the membrane surface, the no-slip fluid velocity is related to the rigid translation $\boldsymbol{V}$ and angular rotation $\boldsymbol{W}$ by

$$\boldsymbol{v}(\boldsymbol{x}) = \boldsymbol{V} + \boldsymbol{W}(\boldsymbol{x} - \boldsymbol{x}_{com}), \tag{3.15}$$

where $\boldsymbol{x}_{com}$ is the initial center of mass located at the origin. Since we are interested in the center of mass advection $\boldsymbol{v}(\boldsymbol{x}_{com})$, we can ignore the rotation $\boldsymbol{W}$ of the membrane and solve Eq. 3.14 to obtain $\boldsymbol{V}$.

Equation 3.14 can be simplified by considering the underlying lattice and membrane symmetry. For colloids arranged in a lattice along a rigid disk, the magnetic dipole force cancels out for all colloids in the bulk. Therefore, the forces along the perimeter dominate. Furthermore, the center of inversion symmetry for all points along the perimeter of a circular membrane yields opposite forces of equal distance from the center resulting in no locomotion, $\boldsymbol{v}(\boldsymbol{x}_{com}) = 0$. Therefore, we create an imbalance of point forces by making a small truncation along the y direction in the $x > 0$ domain, (i.e. we remove a circular segment centered on the x axis). The difference in the number of point forces due to truncation ΔN on opposite sides of the membrane is due to the number of colloids that can fit along the difference in the edge lengths $\Delta L/\sigma$, where $\Delta L = 2R[2\sqrt{S(1-S)} - \sin^{-1}(2\sqrt{S(1-S)})]$. By using the Puiseux series, we can approximate $\Delta N = 8RS^{3/2}/3\sigma$, which is accurate for $S < (3/8)^{2/3} \approx 0.52$. Since the truncation is small, the point force imbalance occurs along the vector $\boldsymbol{x} = -R\hat{\boldsymbol{r}}_x$. We calculate $\boldsymbol{V} = \boldsymbol{v}(\boldsymbol{x}_{com})$ for an infinitesimally thin disk. With these simplifications, Eq. 3.14 and takes the form

$$\boldsymbol{V} = \frac{\Delta N(\hat{\boldsymbol{\mu}} \ \cdot \ \hat{\boldsymbol{r}}_x)}{8\pi\eta R}(\boldsymbol{I} + \hat{\boldsymbol{r}}_x\hat{\boldsymbol{r}}_x) \cdot \hat{\boldsymbol{\mu}} \tag{3.16}$$

Time-averaging $\boldsymbol{v}$ over the precession period $2\pi/\omega$, we obtain

$$< V_x > = < V_z > = \ 0 \tag{3.17}$$

$$< V_y > = \frac{S^{3/2}\mu_0\mu^2 \sin 2\theta \tan\gamma}{8\pi^2\eta\sigma^5} \tag{3.18}$$

and see that the membrane velocity V is directed along the truncation cut. We can replace the reduced amplitude $\tan\gamma$ with the previous definition of the magnetoelastic parameter to obtain a nondimensional swimming velocity reduced by $R\omega$,

$$\frac{V}{R\omega} = \frac{V}{R\omega} = \frac{C^2}{12\zeta(3)}\frac{S^{3/2}}{(\tau\omega)^2}, \tag{3.19}$$

where the $S^{3/2}$ dependence comes from the number of uncompensated point forces formed by truncation. The velocity is normalized by the phase speed $R\omega$ and is displayed as the blue line in Fig. 3.5c. The inverse squared relation on $\tau\omega$ for the velocity is a result of the dependence on the product of the magnetic force and wave amplitude, which, in turn, relies on the magnetic force. Here, we recover the velocity dependence on the square of the wave amplitude [68], but with a lower velocity ($V \leq V_{Taylor}/6$). Details of the full derivation are found in Appendix E. We see a deviation between simulations and Eq. 3.19 at large values of $S^{3/2}/(\tau\omega)^2$ owing to either a high degree of truncation (a linear polymer) or a small viscomagnetic parameter ("dancer"). The direction of travel along the circular path is dictated by the handedness of the precessing field and is an example of magnetically induce symmetry breaking. We find that the continuous symmetry measurement [88] can predict relative changes in the velocity of locomotion. When the inversion asymmetry increases, V increases (Fig. 3.5c, inset) because the conformational path taken by the membrane widens, leading to greater net work done on the fluid [89].

3.3.3. Directed membrane swimming

Here, we give an example of how a programmed magnetic field can produce a non-reciprocal conformational path that results linear swimming. In Fig. 3.6a, we show that a precessing field can rotate the membrane 180° from its initial configuration. Then, the precession frequency is increased and θ is set to $\pi/2$. This keeps the membrane flat in the precession plane while the precession axis is rotated to flip the membrane. This field is turned on for a period of π/ω_s to flip the membrane orientation, where $\omega_s > \omega$. Once the membrane resembles the starting configuration, the two-step field is repeated. After half the orbit from Fig. 3.5b is obtained, the membrane's center of mass has shifted $\sim 2\rho$. The "flip" from the second field places the membrane back into its original configuration. This recovery stroke moves the membrane back toward its original position, but not entirely, leading to a net translation. The chirality and duration of the magnetic field precession controls the displacement in the membrane plane and the flip direction controls the direction for the out-of-plane displacement. The fastest achievable velocity using this method, assuming no distance loss during the recovery stroke, is the path the membrane follows around consecutive semicircles, $V_{max} = \frac{2}{\pi} < V_y >$.

This cycle forms a closed loop in configuration space based on two independent degrees of freedom, ζ_n and ζ_S, defined by the angles the normal vector $\boldsymbol{n}$ and the truncation vector $\boldsymbol{S}$ make with the x axis, respectively (Fig. 3.6b). This configuration loop is an example of non-reciprocal motion, like the wobbling mode, but is needed to achieve efficient swimming since the latter only follows circular paths. Thermalizing the LB fluid to 1 k_BT, by the method of Adhikari *et al.* [76] for $S^{3/2}/(\tau\omega)^2 \approx 10^{-2}$, shows a swimming membrane as ζ_n and ζ_S changes (Fig. 3.6c). In this instance, the path during the rotation step, to change ζ_S, is dominated by Brownian motion. The largest displacement occurs during the flipping step, to change ζ_n. Additionally, each flip shifts the membrane along the z axis, where the traveling direction is determined by the handedness of the flip. By controlling the precession axis orientation, a membrane may be directed along an arbitrary path.

The useful swimming regime is bound by the Péclet number (Pe) and the dimensionless transition frequency. In other words, the system parameters, in particular, the field frequency ω, must be large enough to maintain the wobbling mode, but not too large as to attenuate the wobble amplitude below an efficient swimming velocity. In practice, this implies operating at a driving frequency just above ω_c. The range for the frequency can be written as $\omega_c < \omega < C^2\eta R^3 S^{3/2}/\sqrt{2}\ \zeta(3)\tau^2 k_BT$, where the upper bound is set to $\text{Pe} = 1$. Here, we calculate $\text{Pe} = VR/D$ using the membrane swimming velocity V, the radius R as the characteristic length, and set the diffusion coefficient D using the radius of gyration of a disk [90]. For example, a membrane of $R = 1$ µm composed of 25 nm magnetite nanoparticles at 25°C in water subject to 50 mT field [91] precessing at 80° gives an effective frequency range of 1-10 kHz.

3.4. Conclusions

Superparamagnetic membranes with homogeneous composition require both non-reciprocal motion and shape asymmetry to swim in viscous fluids. While the Scallop Theorem [6] makes the necessity for non-reciprocal motion known, implementing such motion without modifying the elastic or magnetic homogeneity implies using a “non-reciprocal” magnetic field, where the field vector returns to its starting position without retracing its path. Using a field that does not self-retrace imparts a change in membrane conformation that breaks time-reversal symmetry. However, this type of external magnetic field will still generate centrosymmetric forces within a symmetric membrane. Therefore, shape asymmetry is also needed to displace the membrane center of mass during each period of motion, where more asymmetry leads to a larger per-period displacement.

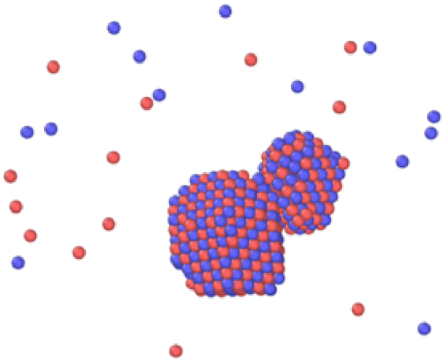

Part 2

Colloidal Magnetic Crystals

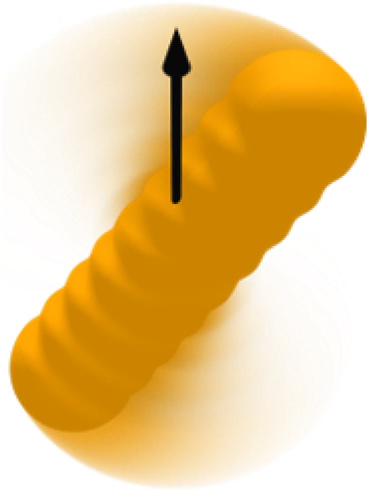

CHAPTER 4

DNA-Assembly of Magnetic Colloidal Crystals

4.1. Introduction

Deoxyribonucleic acid (DNA) has remarkable power in colloidal engineering by facilitating selective and reversible bonds between particles [92–94]. By exposing single-stranded DNA at the outer end of a coated colloid, these “sticky ends” will have favorable hydrogen bonding interactions with their complementary sequence. Aggregations of DNA coated colloids will form specific crystal structures depending on the type and mixtures of sticky ends used [95]. The advantage of these systems is that the chemical and physical properties are controlled by independently by altering the shell and core of the particle leading to any desired combination [96] of lattice parameter, core size, or crystal symmetry, etc. DNA mediated crystallization has uncovered a library of crystal structures with a wide array of applications [97–99].

In recent years a greater influence has been placed on remotely controlling colloid aggregation using external fields [100]. Typically, these assemblies result in either chains [101, 102] or disordered aggregates [29, 103–106]. While crystalline assemblies can form [107], their crystallographic properties remain confined to the narrow conditions dictated by the synthetic environment and there is little control over the shape of the cluster. In particular, creating anisotropic structures are difficult without lithographic techniques [108]. Methods that combine evaporative techniques under magnetic fields have achieved a degree of success in controlling both crystalline order and anisotropic shape control [8, 109]. However, magnetic fields alone have been an ideal choice for directing colloid assembly largely due to its ease of application, flexibility to produce a wide array of field gradients, temperature and chemical independence, and ability to penetrate soft matter systems [110, 111].

In collaboration with Prof. Mirkin at Northwestern University [80], we use theory, simulations, and experiments to uncover avenues for the construction of a wide array of colloidal crystals using magnetic fields. We focus on a system composed of type A and type B particles. Type A particles use their DNA to bind with the DNA of type B particles and vice versa. The sticky ends of type A particles do not bind to other type A particles. Likewise, type B particles do not bind to themselves. In a 50:50 mixture, a body-centered cubic (BCC) crystal lattice will form. We seek to understand how a magnetic field will effect crystal morphology of particles with a core of superparamagnetic magnetite. Using a magnetic field to alter the crystal shape has many potential advantages because the shape would be maintained after the field is turned off and the crystal would not have residual magnetism because the transition to ferromagnetic behavior does not occur despite being the same size [107].

4.2. Methods

4.2.1. Molecular dynamics simulations

Coarse-grained molecular dynamics simulations were executed using the LAMMPS package.[35] and were visualized using Ovito [71]. DNA-coated iron oxide nanoparticles were modeled as a magnetic point dipole sharing a custom DNA potential with screened coulombic interactions [112]. Each simulation consisted of "type 1" and "type 2" particles with complementary sticky ends using an NVE ensemble with a Langevin thermostat [113, 114]. The total potential energy between a pair of particles is the sum of the magnetic and DNA hybridization interactions,

$$U = U_{mag} + U_{hybrid}. \tag{4.1}$$

The magnetic interactions between nanoparticles were modeled as a dipole of fixed magnitude pointing in the direction of the magnetic field, which was along the z-axis. The dipole-dipole interactions between nanoparticle i and all j neighbors within the cutoff distance, 10.4σ, was calculated using the following pairwise expression.

$$U_{mag} = \frac{\mu_0 \mu}{4\pi r_{ij}^3}(1 - 3(\hat{\boldsymbol{\mu}} \cdot \hat{\boldsymbol{r}}_{ij})^2), \tag{4.2}$$

where μ_0 is the magnetic constant, and r_{ij} is the displacement vector between nanoparticle i and nanoparticle j.

The attractive binding potential of complementary DNA strands was calculated using the method of Dhakal et al. that relates the strength of the potential to the overlap of DNA binding regions [112]. The hybridization energy is a sum of an attractive overlap and electrostatic repulsion,

$$U_{hybrid} = U_{overlap} + U_{el}. \tag{4.3}$$

The potential U_{hybrid} is scaled by a factor, C, between 0 and 1, to scale the depth of the potential well, which defines the dimensionless DNA interaction strength ε_{DNA}, more explicitly, $\varepsilon_{DNA} = \frac{C}{k_B T} U_{hybrid}(r_{min})$, where r_{min} coincides with the diameter of the particle. The attractive DNA potential is based on an overlapping-spheres model which describes the attraction of overlapping regions as

$$U_{overlap} = -k_B T n(\frac{\Delta V(r)}{V}), \tag{4.4}$$

where k_B is the Boltzmann constant, T is the absolute temperature, V is the volume, n and is the DNA coverage, and $\Delta V(r)$ is the overlapping region between particles. The relevant geometric parameters for calculating the overlap are nanoparticle and dsDNA radius, and the sticky-end length. These parameters were set to 20.4 nm and 3 nm, respectively. We used $\eta = 0.01$ for the Gaussian smoothing function, which avoids discontinuities in the potential at the maximum linker distance. The strength of the overlap interaction was tuned by changing n. Between particles of the same type, $U_{overlap}$, is turned off.

The purely attractive overlap interaction is counteracted through screened electrostatic repulsion from the charged DNA backbone in the electrolyte solution (650 mM NaCl). We use the Derjaguin approximation to relate the electrostatic potential between two infinite plates to the force felt between nanoparticles [112]

$$U_{el} = 64\pi R\rho\gamma^2 e^{-\kappa(r-2R)}. \tag{4.5}$$

where r is the distance between nanoparticles, R is the nanoparticle radius, κ is the inverse Debye length, γ depends on the effective surface potential, and ρ is the bulk ion concentration. The inverse Debye length was estimated based on the ionic salt concentration to be 2.6 nm^{-1} with a Bjerrum length, ℓ_B, of 0.7 nm calculated from $\kappa^2 = 4\pi\rho\ell_B$. For quantitative analysis, recent work has shown that the Debye length grows with increasing salt concentrations above 500 mM due to ion-ion correlations [115]. The radius R of the nanoparticles was set at 20.4 nm; this sets the nearest neighbor distance in a BCC lattice at 41.6 nm, consistent with the measured lattice parameter of 48 nm. It should be noted that R in U_{el} can be replaced by $2R_AR_B/(R_A+R_B)$ if complementary nanoparticles have different sizes. However, the most significant change in how the system aggregates will be dictated by the change in the magnetic coupling parameter, $\Gamma \propto (R_A + R_B)^{-3}$.

The simulation was executed using Lennard-Jones reduced units, where the temperature, nanoparticle density, and $\mu_0/4\pi$ were set to 1. The length scale, σ, was set to 40 nm, implying a nanoparticle diameter of 1.04σ. Each simulation was run at a volume fraction of 0.01. The damping parameter for the Langevin thermostat was set to 0.1. Each simulation was run for 1.2×10^6 steps with a time step of 0.001 with periodic boundary conditions. The neighbor mismatch probability was averaged from 5 independent simulations of 2000 particles, 50/50 mixture, with a random initial distribution. The radial pair distribution function was calculated in VMD [116].

4.2.2. Magnetic dipole component to surface energy

Using a custom Python code, BCC arrays of dipoles were created with two exposed surfaces. The thickness of the array between the two surfaces was twice the cutoff distance, R_c, for the dipole-dipole interactions. There were no interacting forces or particles above the surfaces. The total dipole-dipole interaction energy was calculated (using LAMMPS) with the dipole vector at various angles from the surface (0° indicating parallel with the exposed surfaces and 90° indicating perpendicular to the surfaces). The cutoff distance

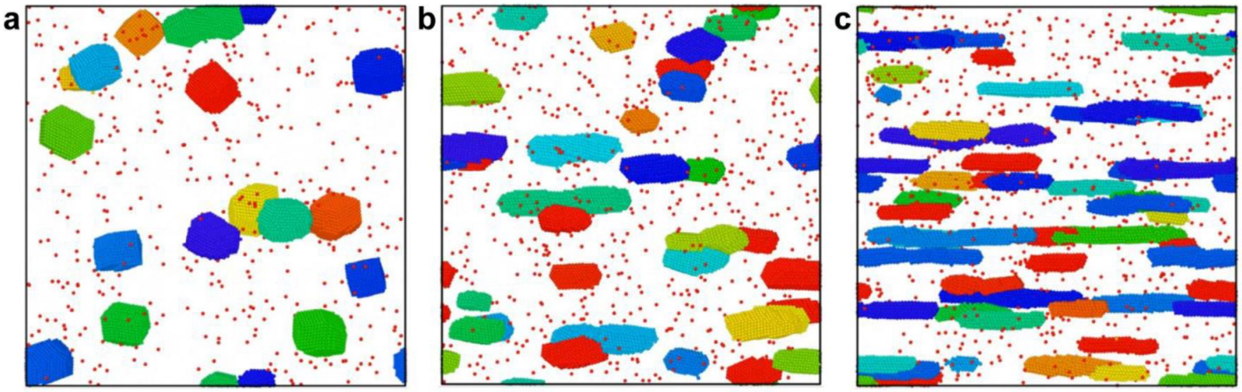

Figure 4.1. Molecular dynamics snapshot of a 1:1 stoichiometry mixture of complementary DNA-coated superparamagnetic nanoparticles in a magnetic field pointing to the left. Each particle has a dipole moment of (a) 0.0, (b) 0.5, and (c) 0.9. Colors represent single crystals of nanoparticles.

was increased until there was a ¡ 0.5 change in the dipole energy, which occurred for $R_c > 60\sigma$. The total dipolar energy was normalized by the total area of exposed surface.

4.2.3. Magnetic coupling between clusters

Two adjacent BCC rhombic dodecahedron were generated using a Haüy construction [117, 118] from 1 to 8 layers of point-dipoles, corresponding to a cluster size of 4.4 to 28.2 , where = 48 nm. The clusters were placed with two parallel rhombic faces positioned 1 apart with the dipoles oriented perpendicular to the parallel faces. The total dipole-dipole interaction energy between the two clusters was calculated over all dipole pairs using U_{mag}. The calculation was executed using LAMMPS over a single time step. Normalized by thermal energy, k_BT, this dimensionless parameter is the magnetic coupling.

4.3. Results and Discussion

In the absence of substantial thermal agitation, magnetic particles assemble along magnetic field lines. This suggests that DNA-coated superparamagnetic nanoparticles will form elongated BCC crystals. Indeed, MD simulations that incorporate both DNA and magnetic interactions find that the aspect ratio of nucleated cystals increase as the field increases (Fig. 4.1). We can show that this must be the case analytically by considering the potential energy of the crystal due to these two forces: the long-range dipole-dipole interaction and the short-range DNA interaction and set the total potential energy F of a magnetic rod is a sum of the magnetic energy F_m and the surface energy F_A, coming from the absence of DNA hybridization on the rod's surface. The surface energy term defines a surface energy per unit area taken with the surface area of a rod, $A(\rho, z) = 2\pi(\rho^2 + 2\rho z)$, with radius ρ and length z. The surface energy term is simply $F_A = \gamma A(\rho, z)$, where γ is the surface tension. We normalize the surface energy by the thermal energy and number of particles to obtain

$$F'_A = \frac{\gamma a^3}{NVk_BT} A(\rho, z), \tag{4.6}$$

where k_B is the Boltzmann constant, T is the temperature, and the number of particles NV/a^3, where a is the lattice constant, and N is the number of particles in the unit cell. The volume, V, of the rod can be viewed as constant because the volume fraction of the system is held constant. The magnetic term is a sum of the dipole-dipole interactions U_{mag} between all particles in the crystal according to Eq. 4.2. As the magnetic field strength increases, the aspect ratio that minimizes the free energy increases (Fig. 4.2).

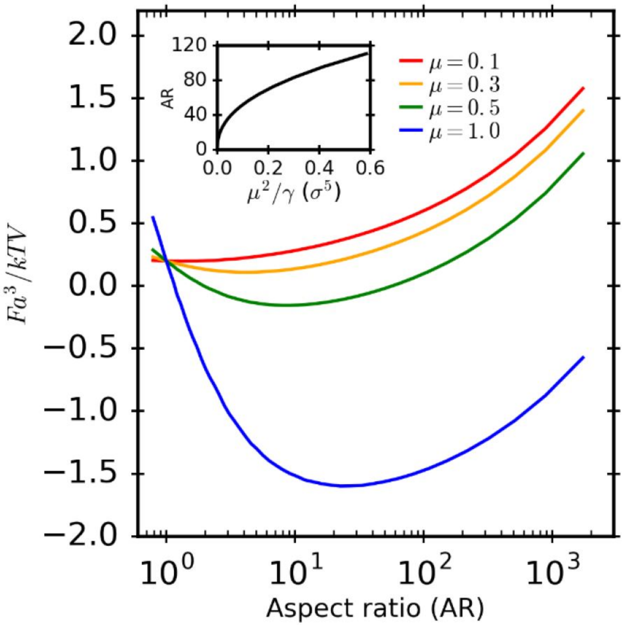

Figure 4.2. Normalized potential energy curves for a square prism crystal as a function of crystal aspect ratio (AR). The inset shows how increasing the ratio between field and surface energy density increases the equilibrium AR of the crystal.

This analysis ignores differences in the magnetic interacts along crystal facets. In the experimental cases describe later, we see that DNA hybridization dominates and forms a BCC with (110) crystal surfaces. However, we note here that close to the crystal melting temperature, or with weaker hydrogen bonding, the dipolar interactions could affect the exposed facets. In fact, the (111) surface has the lowest magnetic energy due to its high density and structural arrangement (Fig 4.3) and should be exposed along the sides of the crystal. Likewise, the plane growing along the field is the lowest density (100) in order to minimize magnetic repulsion.

We can construct a phase diagram in Fig. 4.4a for the possible rod morphologies by controlling the magnetic coupling between superparamagnetic nanoparticles Γ_1 and the complementary DNA hybridization strength ε_{DNA}. When both parameters are weak, the

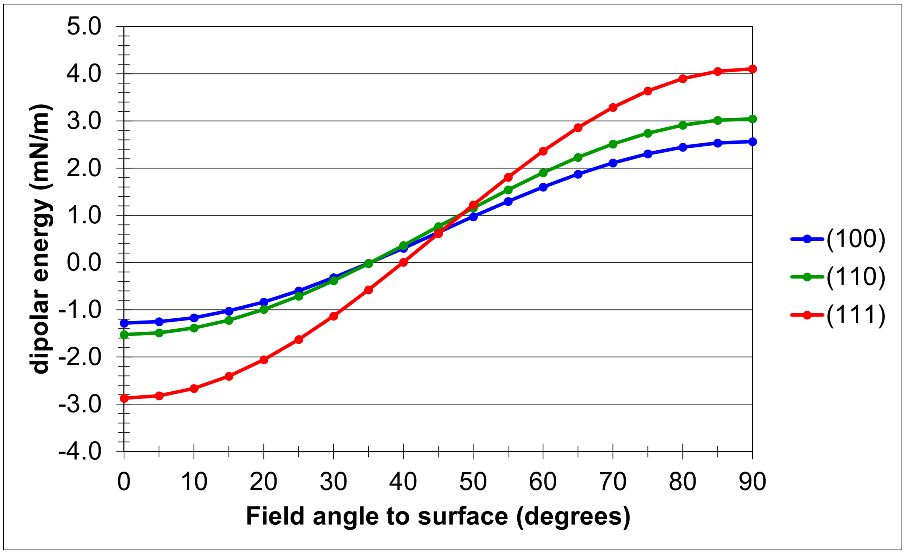

Figure 4.3. Estimate for the magnetic contribution to the surface energy for (100), (110), and (111) surfaces of magnetically saturated 20 nm magnetite nanoparticles.

system is composed of free particles. As Γ_1 increases, the aggregation behavior matches that of the theory of Faraudo *et al.* [22] in that chains will form in equilibrium with the surrounding unaggregated particles. Further increasing the magnetic field strength ($H \sim \mu^2 \sim \Gamma_1$) results in the aggregation of the chains into bundles. In the weak ε_{DNA} case, these chains and bundles have disordered A-B particle pairing. As the hybridization strength increases, the greater the likelyhood that complementary particles will be neighbors (Fig. 4.4b. We see that stronger Γ_1 increases the probability of particle neighbor mismatch because they are stuck in a magnetically stabilized high-energy state.

Experimental results obtained by the Mirkin group showed two primary crystal morphologies depending on the size of the magnetite nanoparticles and the strength of the magnetic field. They observed that using strong magnetic fields (3800 G) resulted in a rod with small, diffuse crystal grains. These small grains gave the rod a "smooth" appearance

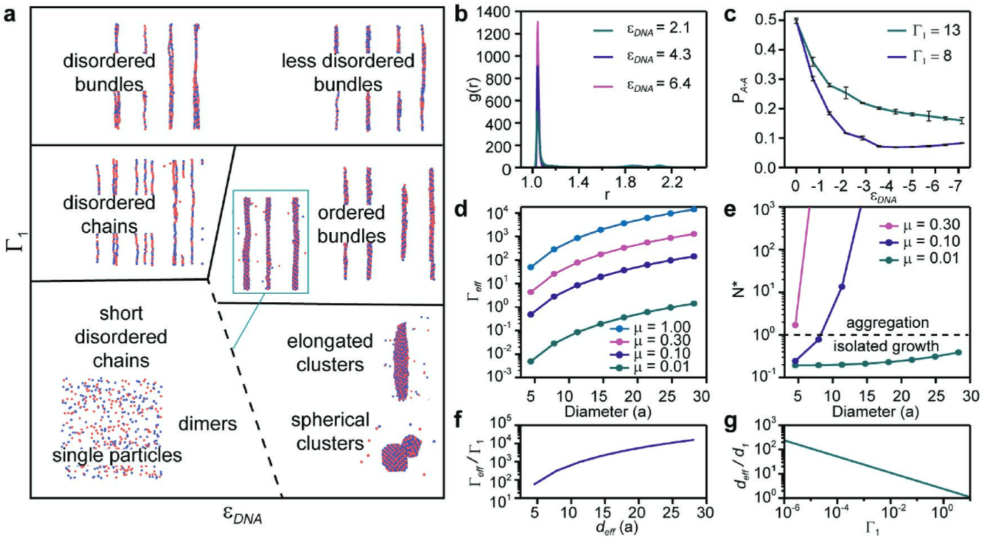

Figure 4.4. a) Schematic showing how magnetic coupling between individual superparamagnetic particles, Γ_1, and the DNA hybridization interaction strength, ε_{DNA}, between complementary particles affect system morphology. b) Radial pair distribution plots with increasing ε_{DNA}. c) Mismatch probability between complementary particle types increases with increasing magnetic field. d) The change in the effective magnetic coupling between clusters, Γ_{eff}, as cluster diameter grows (in lattice parameter units). e) The aggregation parameter with increasing cluster diameter (in lattice parameter units). f) The magnetic coupling between two clusters of equal sizes, Γ_{eff}, normalized by the magnetic coupling between individual particles, Γ_1. g) Calculation of the diameter of a cluster at the onset of chain formation given the initial magnetic coupling. It follows the scaling law $d_{eff} \sim \Gamma_1^{-1/3}$. This figure is adapted from Park *et al.* [80]

with flat, straight surfaces (Fig. 4.5, left). Weaker magnetic fields resulted in recognizable chains of large dodechedronal clusters (Fig. 4.5, right). Both rods possess an underlying BCC structure, indicating that they are in the strong ε_{DNA} regime. The difference in these two rod morphologies relates to how individual magnetic particles couple with each other.

From our phase diagram, we also observe two distinct morphologies when ε_{DNA} is strong and Γ_1 is intermediate in strength. The same thermodynamic analysis used to

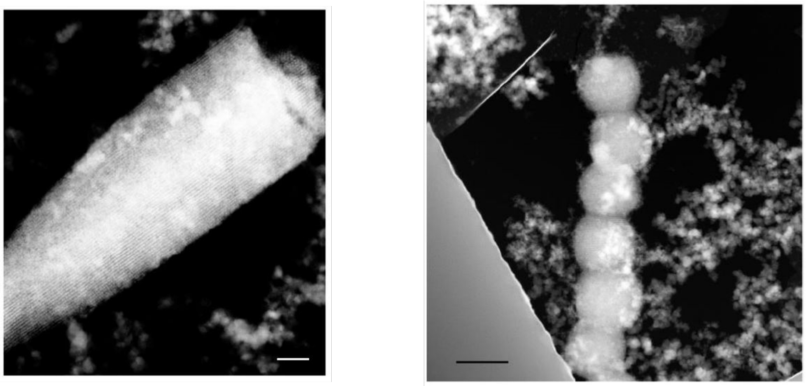

Figure 4.5. (left) Scanning tunneling electron microscope image of a rod under a 3800 G field, assembled from (left) 20 nm Fe_3O_4 nanoparticles, scale bar: 500 nm and (right) 10 nm Fe_3O_4 nanoparticles, scale bar: 2 µm.

predict chain formation of superparamagnetic nanoparticles can be used to predict the onset of chains of clusters [119]. The tendency of the system to form chains id dependent on the aggregation number $N^* = \sqrt{\phi_0 \exp \Gamma_1 - 1}$ of the system, where ϕ_0 is the volume fraction of particles. The free particle regime occurs when $N* < 1$, when the system is dominated by entropy. Chains form when $N* > 1$ and bundles (aggregation of parallel chains) form when $N* >> 1$.

Theoretically, the analysis of Andreu *et al.* applies to all superparamagnetic particles, regardless of scale. Therefore, when large BCC clusters form, they act as one large superparamagnetic particle with a new magnetic coupling constant Γ_{eff}. We show in Fig. 4.4d how Γ_{eff} increases as a function of cluster size. These curves collapse into a single function when normalizing them by the single-particle magnetic coupling (Fig. 4.4f). The exponential dependence of the aggregation number on the magnetic coupling explains how large chains of clusters occur in systems with weak dipoles, which can occur using a weaker field or, or equivalently, smaller nanoparticles. It isn't until the system crosses $N^* = 1$ that the isolated growth of clusters eventually causes them to form chains

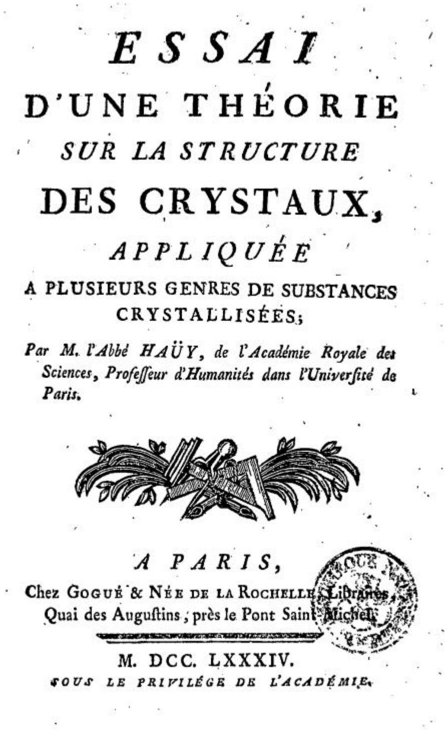

ESSAI
D'UNE THÉORIE
SUR LA STRUCTURE
DES CRYSTAUX,
APPLIQUÉE
A PLUSIEURS GENRES DE SUBSTANCES
CRYSTALLISÉES;
Par M. l'Abbé HAÜY, *de l'Académie Royale des Sciences, Profeſſeur d'Humanités dans l'Univerſité de Paris.*

A PARIS,
Chez GOGUÉ & NÉE DE LA ROCHELLE, Libraires,
Quai des Auguſtins, près le Pont Saint-Michel.

M. DCC. LXXXIV.
SOUS LE PRIVILÉGE DE L'ACADÉMIE.

Figure 4.6. An image of the title page for Haüy essay on his theories for crystalline solids. On page 21 he states the beginning of his construction: "...avec une multitude de petits cubes, une pile quadrangulaire régulière, c'est-à-dire, composée de couches qui aillent en décroissant uniformément de la base au sommet." Translating this as: " ...with a multitude of small cubes, a regular quadrangular pile, that is to say, composed of layers which decrease uniformly from the base to the top." [117]

(Fig. 4.4e). Likewise, if chains form when clusters are very small, we obtain the observed smooth rod morphology.

We calculate the $\Gamma_e ff$ for a cluster using a Haüy construction. In his 1784 essay on crystalline solids (Fig. 4.6), Haüy proposed a method for building shapes, like dodecahedrons, using cubic cells. By layering the unit cells of a BCC crystal to form a square pyramid on each face of the initial cell, a dodecahedron emerges (Fig. 4.7). In the weak field regime, we can now calculate the effective diameter d_{eff} of a cluster that will induce

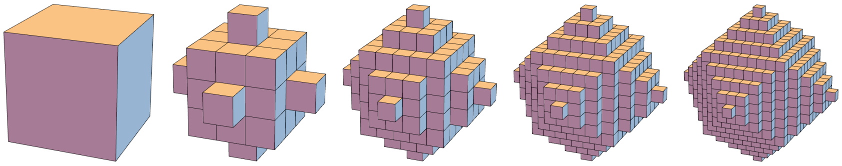

Figure 4.7. Haüy construction of a dodecahedron using cubes. Image from Wolfram [118].

chain formation. Calculation shown in Fig. 4.4g, reveal that this cluster becomes smaller as Γ_1 increases. The ratio Γ_{eff}/Γ_1 depends on the volume of the cluster

$$\frac{\Gamma_{eff}}{\Gamma_1} = \alpha^2 \Big(\frac{d_{eff}}{d_1}\Big)^3, \tag{4.7}$$

where α is a material and geometric constant that relates the dipole of a cluster with its volume. For a BCC dodecahedron composed of identical superparamagnetic particles, $\alpha^2 \approx 4/5$. Eq. 4.7 can be solved for d_{eff}/d_1 at the onset of chain formation ($N^* = 1$) to obtain

$$\Big(\frac{d_{eff}}{d_1}\Big) = \Big(\frac{5(1 - \ln \phi_0)}{4\Gamma_1}\Big)^{1/3} \tag{4.8}$$

This equation gives us the slope of the curve in Fig. 4.4g (-1/3) and allows us to predict the width of the rod using only the properties of the initial superparamagnetic nanoparticles.

4.4. Conclusions

Our work shows that an applied magnetic field will affect the growth properties and overall morphology of superparamagnetic nanoparticles coated with complementary DNA binding. This applies not only to DNA, but any short-range chemical linking system.

MD simulations and experiments show the formation of elongated magnetic rods due to magnetic dipole-dipole interactions. The morphological consequences of the magnetic coupling between particles are significant. The magnetic coupling between BCC clusters increases as they grow. Eventually, the clusters will form chains. If this occurs when the cluster is small, the resulting magnetic rod will possess a smooth surface. If magnetic interactions are weak, the clusters will grow much larger until they are able to assemble into chains. Our results are relevant to any magnetic system with competing bonding interactions and will predict the morphology of magnetic aggregates.

CHAPTER 5

Precession-driven phase transitions in Superparamagnetic Nanorods

5.1. Introduction

Colloidal crystals composed of superparamagnetic particles are shown as promising platforms for optoelectronics [120, 121], mechanosensors [122], and filtration [123, 124] devices due to their biocompatibility and responsiveness. However, it is critical to understand how the morphological evolution of the crystal is controlled by the magnetic field and competing interactions. While crystalline ordering is usually driven by close-packing [125, 126], chemical bonds [80, 127], or magnetic interactions [128, 129] to create a static structure, it can also be controlled by particle shape and motion. Such entropic effects emerge when thermal energy is significant allowing elongated particles to adopt liquid crystal phases [130].

Spontaneous 1-D positional ordering arises from collections of elongated particles (the so-called smectic phase), whereby they develop a layered structure. Smectic liquid crystals have many applications in science and technology such as thin films [131], electromechanical sensors [132], actuators [133], and fabrication platforms [134], owed to this layered 1-D period order. It even has an emerging relevance in cell biology [135]. Magnetic fields can guide the formation of the smectic phase for systems where the magnetic interactions between particles is weak [136].

Interactions between superparamagnetic particles can be estimated by calculating the magnetic coupling constant [119] $\Gamma = \mu_o \mu^2/2\pi d^3 k_B T$, where μ_o is the magnetic constant, μ is the dipole magnitude, k_B is the Boltzmann constant, T is the absolute temperature, and d is the distance between dipoles. It represents the strongest possible magnetic interaction relative to thermal energy. If $\Gamma \gg 1$, magnetic interactions dominate over thermal forces and the system can become fixed in a magnetic-stabilized state. Therefore, new physics can be uncovered by studying systems where $\Gamma \ll 1$. In this regime, the magnetic field manipulates the motion of particles and the small Γ prevents aggregation or repulsive trapping. This is a reasonable and common condition. Magnetic particles are often coated in a non-magnetic layer to act as a linking agent, biocompatibility layer, and an aggregation inhibitor [137, 138]. Additionally, by operating in a low magnetic coupling regime, the applicability of results is expanded to any system that generates a field or force (electrical, chemical or hydrodynamic) that produces similar particle motion.

Here, we use a combination of theory and molecular dynamics models to demonstrate how a precessing magnetic field can drive a system of coated (low Γ) superparamagnetic rods into the smectic phase. First, we describe the motion of the rods using theory and define the valid regime for the "strong precession" model that forgoes the need for explicit magnetic calculations. Next, we explain that the system is defined by two parameters: the reduced concentration ρd^3, and the rod precession angle β. On this phase diagram, we compare simulations using explicit magnetic calculations to the steric MD model and see how both show larger β favours the smectic phase. Finally, we demonstrate how rod interaction drives phase separation in binary mixtures.

5.2. Methods

We seek to predict the nematic-smectic phase transition in a system of precessing superparamagnetic rods composed of a stiff linear chain of superparamagnetic particles. To this end, we begin by calculating the precession angle of the rod β. While this angle is suppressed at very high densities, this investigation will inform how the phase diagram can be constructed later on. Then, we will describe a purely steric MD model that forgoes the need for costly magnetic calculations. Finally, we will describe the "full" MD model against which our other models can be tested.

5.2.1. Precession angle for dilute superparamagnetic rods

An externally applied magnetic field controls the orientation of superparamagnetic rods. The orientation of the rod is parametrized by the angle with respect to the precession axis β and the azimuthal angle α. By convention, we align the precession axis in the z-direction and measure the azimuthal angle from the x-axis. We apply a precessing magnetic field in the direction $\hat{\boldsymbol{H}} = (\sin\theta\cos\omega t, \sin\theta\sin\omega t, \cos\theta)$, where θ is the magnetic field precession angle, ω is the precession angular frequency, and t is time. For a superparamagnetic system, $\boldsymbol{H} = \boldsymbol{\mu}/\chi$, where χ is the magnetic susceptibility and $\boldsymbol{mu}$ is the dipole moment. For $\cos\theta < \frac{1}{\sqrt{3}}$, a stiff rod will precess synchronous to the field and avoid oscillatory behaviour [83]. Therefore, we define the orientation of the rod using its long axis, $\hat{\boldsymbol{n}} = (\sin\beta\cos\alpha, \sin\beta\sin\alpha, \cos\beta)$, where β is the angle from the z-axis, and $\alpha = \omega\, t - \phi$, where ϕ is the phase lag.

The phase lag determines the magnetic torque acting on the superparamagnetic rod and must be balanced by the drag torque. We define the drag torque according to a

Rayleigh viscous dissipation function P added to the Euler-Lagrange (EL) equation [84],

$$\frac{d}{dt}\frac{\partial L}{\partial \dot{\alpha}} - \frac{\partial L}{\partial \alpha} + \frac{\partial P}{\partial \dot{\alpha}} = 0, \tag{5.1}$$

where $\dot{\alpha} = \frac{d\alpha}{dt}$, and $L = T - U$ is the Lagrangian, where T is the kinetic energy and U is the potential energy. In a manner similar to previous work on magnetoelastic membranes [139], the EL equation is constructed from the interactions of superparamagnetic particles moving in a viscous fluid. Furthermore, in a Stokes regime, acceleration terms can be neglected leaving us with the simple form

$$\frac{\partial U}{\partial \alpha} + \frac{\partial P}{\partial \dot{\alpha}} = 0. \tag{5.2}$$

The rods do not stretch or bend so only the magnetic interactions contribute to the potential energy U. We use a nearest neighbours approach to calculate the dipole-dipole interactions of each superparamagnetic particle. Each dipole is identical in strength and orientation leading to

$$U = 2\left(N-1\right)\frac{\mu_o \mu^2}{4\pi r^3}\left(1 - 3\left(\hat{\boldsymbol{\mu}} \cdot \hat{\boldsymbol{r}}\right)^2\right), \tag{5.3}$$

where N is the number of beads, μ_o is the magnetic constant, μ is the dipole magnitude, r is the distance between dipoles, and $\hat{\boldsymbol{r}}$ is the displacement vector. In a stiff chain, we take $\hat{\boldsymbol{r}} = \hat{\boldsymbol{n}}$ and the distance r between dipoles to be the size of the particle σ. Taking the derivative with respect to the degree of freedom α yields

$$\frac{\partial U}{\partial \alpha} = \frac{-3N\mu_o \mu^2}{\pi \sigma^3}\left(\sin^2\beta \sin^2\theta \sin\phi \left(\cot\beta \cot\theta + \cos\phi\right)\right). \tag{5.4}$$

Note that in the static-field limit, $\phi \to 0$ and $\beta \to \theta$, this expression results in no torque on the rod ($\frac{\partial U}{\partial \alpha} \to 0$), as expected.

The rod of length l is coated in a passive, non-magnetic layer making the diameter $d > \sigma$. The dissipation function acting on the rod is approximated as the sum of friction elements per unit length d,

$$P = \frac{1}{2}\sum_{i}^{l/d} k v_i^2, \tag{5.5}$$

where the sum over l/d elements considers the velocity v_i at each section of the rod given the friction coefficient $k = 3\pi\eta\ d$, where η is the dynamic viscosity of the fluid. The velocity of each element i is $v_i = u\ d \sin\beta$, where u is the distance along the rod. The distance u increments by $d/2$ because the center of mass (the stationary point during precession) shifts by this amount. That is, the rod precesses around its center element when l/d is even or precesses between two elements when l/d is odd. Note when considering N superparamagnetic beads distributed evenly along the length l, this rule is flipped. For calculating $\sum v_i^2$, we can replace the terms in u^2 with integers by multiplication $(2u)^2/4$ allowing us to replace the sum with an expression for the sum of all integers up to l/d, $\sum (2u)^2 = (2l/d + 1)(l/d + 1)(l/d)/6$. This leads to the equation for the drag torque

$$\frac{\partial P}{\partial \dot{\alpha}} = \frac{3\pi}{16}\eta\sigma\omega\ d^3 \left(2\frac{l}{d} + 1\right)\left(\frac{l}{d} + 1\right)\left(\frac{l}{d}\right)\sin^2\beta. \tag{5.6}$$

We see that when l/d goes to zero (a sphere), so does the drag torque. Plugging in our expressions in Eq. 5.4 and Eq. 5.6 into Eq. 5.2 leads to the relation,

$$\Omega \sin^2\theta \sin\phi\,(\cot\beta \cot\theta + \cos\phi) + \omega = 0, \tag{5.7}$$

where $\Omega = 12N\mu_o\mu^2/\eta\pi^2\sigma^3 d^3(l/d)^3$ for long rods ($l/d \gg 1$). The magnetoviscous ratio Ω is a characteristic frequency that depends on the strength of the magnetic energy ($N\mu_o\mu^2/\sigma^3$) compared to the viscous drag ($\eta\ d^3\,(l/d)^3$) and can be thought of as a characteristic "response" frequency of the rod in a dynamic magnetic field. Solving for β, we obtain our final expression for the rod precession angle,

$$\beta = \cot^{-1}\left(\frac{2}{\sqrt{3}}\frac{\omega' \csc\phi}{\sin 2\theta} - \cos\phi\tan\theta\right). \tag{5.8}$$

The reduced field frequency $\omega' = \frac{\omega\sqrt{3}}{\Omega}$ defines the relationship between the rod response time and the field precession period. While ω' is a magnetoviscous parameter,24 leaving it as reduced frequency intuitively reflects its role as a scaled frequency. Therefore, it is easy to see the β curve for a particular θ in Fig. 5.1a becomes centered at 1 when plotting against ω'. The reduced field frequency can be rewritten in terms of a set of dimensionless constants,

$$\omega' = \frac{1}{72\sqrt{3}}\frac{(\ln\left(\frac{l}{d}+1\right)+C)}{R^4\Gamma D'}, \tag{5.9}$$

where R is the thickness ratio d/σ, the magnetic coupling constant $\Gamma = \mu_o\mu^2/2\pi\ d^3 k_B T$, where k_B is the Boltzmann constant, and T is the absolute temperature, $D' = D/\omega\ A$ is the relative diffusion constant relating the diffusion timescale over the rod area $A = ld$ to the field precession period. The $\ln(l/d+1) + C$ terms relate to the diffusion $D = k_B T(\ln(l/d+1)+C)/3\pi\eta\, l$, where $C \approx 0.312$ for sufficiently long rods ($< 5\% error for l/d >$ 4) [140].

To find the expression for ϕ, we solve Eq. 5.8 in the slow field limit. Under a pseudo-static field, the rod will maintain alignment with the field direction. This limit implies $\beta \to \theta$ and that the lag is very small leading to $\cos\phi \to 1$. We obtain $\phi = \tan^{-1}(\omega/[(\Omega - \omega)(\Omega + \omega)]) \approx \tan^{-1}(\omega'/3)$.

Eq. 5.8 shows that there is a well-defined intermediate frequency at which $\beta = \theta/2$. If we set this condition for β and solve for ω, assuming real solutions with $\omega > 0$, we can expand a power series around $\cos\theta = 1$ to obtain

$$\omega'_{\theta/2} = 1 + \frac{5}{\sqrt{3}}\left(\cos\theta - 1\right). \tag{5.10}$$

5.2.2. Magnetic MD Model

We represent a coated, superparamagnetic rod as a linear chain of magnetic beads of diameter σ that are covered evenly in a non-magnetic layer with thickness $d - \sigma = 2\sigma$. The rod moves rigidly in response to a magnetic field. We simulate under an NVT ensemble a system of rods suspended in solution with density $d^3\rho$. Time is integrated with a step of 0.002 τ, where the unit of time $\tau = \sigma\sqrt{m/\epsilon}$, where is the mass of one magnetic bead. The temperature of the system is maintained by the Langevin method [141]. The temperature is set such that the thermal energy k_BT is equal to the energy unit ϵ and the damping coefficient is 5 m/τ.

The potential energy of the system is a sum of the magnetic and hard-core interactions. The dipole moment $\boldsymbol{\mu}$, at the centre of each bead is oriented in the direction of field $\boldsymbol{H}$, as described in Section 2.1. The magnitude of the dipole moments μ are identical and have units of $\sqrt{\mu_o/4\pi\sigma^3\epsilon}$. The potential energy is the sum of all the dipole-dipole interactions for each bead within a cut off distance of 5σ. The potential energy of one dipole pair is $U_{ij} = \sum_i^M \sum_j^{M'} \frac{\mu_o \mu^2}{4\pi r^3}\left(1 - 3\left(\hat{\boldsymbol{\mu}} \cdot \hat{\boldsymbol{r}}_{ij}\right)^2\right)$, where M is the total number of beads in the system, and $\hat{\boldsymbol{r}}_{ij}$ is the displace vector between beads i and j. Rod collisions are purely repulsive and add to the total potential energy using the WCA potential [34], where the distance parameter σ_{WCA} is set to the total rod thickness d.

The nematic and smectic phases were quantified by calculating their respective order parameters. The orientational information in a collection of symmetric rods (or molecules) can be determined using the order tensor,12

$$Q = \frac{1}{N}\sum_i^{N_i}\left(\hat{u}_{i,\alpha}\hat{u}_{i,\beta} - \frac{\delta_{\alpha\beta}}{3}\right) \tag{5.11}$$

where Q is a second rank tensor, N is the number of rods, $\hat{u}_i$ is the unit orientation vector of rod i, and α and β are the Cartesian coordinates x, y, and z. It is usually assumed that Q is calculated over a small macroscopic volume, which is represented by our simulated system. The nematic director $\hat{\boldsymbol{n}}$ corresponds to the eigenvector of Q with the largest eigenvalue. The smectic order considers the location of the center of each rod, $\boldsymbol{r}$,

$$\kappa = \max_d \left|\left\langle \exp\left(2\pi i \frac{\boldsymbol{r} \cdot \hat{\boldsymbol{n}}}{d}\right)\right\rangle\right|, \tag{5.12}$$

where the layer spacing d is chosen to maximize the order κ. A practical method of extracting smectic order parameter from experiments is to use diffusion data [142].

The precession around the z-axis implies that, if the smectic state is present, the length of the box in the z-direction L_z must be an integer number of layers n. We don't know the layer thickness *apriori* but it will be a function of the rod length $f_0(l)$. There will be a mismatch in the lengths L_z and $nf_0(l)$. This difference will be distributed over all layers

$\delta = L_z/n - f_0(l)$. If δ is small, then $L_z/n \approx f_0(l)$. We can inform how long to make L_z by using the maximum possible value for $\delta_{max} = l/2$. By assuming that $f_0(l) \rightarrow l = 24\sigma$ for small β, we determine that the maximum error in layer spacing over n=50 layers is 0.24σ. The real number of layers we observe is 50 ± 1. The box contains 9,800 rods that are initialized with a random position and orientation. The density begins at $d^3\rho = 0.01$ and is slowly increased at a rate of $3.125 \times 10^{-6} d^3\rho/\tau$ by isotropically shrinking the x-y area.

5.2.3. Purely steric "strong precession" MD model

Due to the cumbersome nature of magnetic calculations, we sought to explore a regime where the essential physics can be captured, but all dipole-dipole calculations can be ignored. Assumptions for this purely steric model are (1) the field is strong enough to maintain the orientation of the rods against Brownian motion, (2) a low magnetic coupling between rods (large R, small Γ), (3) the precession period is much faster than the rod diffusion time (small D'), and (4) the rod precession angle β is not suppressed by collisions (low ρd^3).

The first and second assumptions allow us to ignore dipole-dipole calculations and rotation dynamics. We assume that the rods will always point in the direction of the precessing field. Regardless of how strong the dipole interactions are to meet this condition, the magnetic coupling remains small because the nonmagnetic layer is sufficiently thick (Fig. 5.2a).

The third assumption relates to how the space swept out by a precessing rod over one precession period; that is, distribute repulsive particles along the skin of a double-cone to create an implicit precession. Superparamagnetic rods of identical lengths are in-phase while precessing, meaning that the "precessing" white particles (Fig. 5.2b) do not interact with other white particles. Repulsive interaction is only felt between the central red particle and all other particles. Due to this interaction, the rod must extend l distance away from the center to represent the correct l/d. The density of the white particles is set to $\sim 1/\sigma^2$. The fast field or slow diffusion assumption is distinct from field that is precessing in the limit of infinite precession speed, which we have describe previously [21, 37, 41]. In that case, the field was fast compared to the rod (or chain) response time, analogous to $1/\Omega$. We model it as a rigid body and, since it follows the field, rigid body rotation is restricted.

Assumption (4) depends on dilute conditions. Even in the absence of a magnetic field, increasing rod density, forces the alignment of the rods. This necessarily suppresses β until, at the high density limit, $\beta \to 0$. However, simulations suggest that there is little deviation in β during the nematic-smectic transition, which we show later on in Fig. 5.3.

Based on these conditions we have developed a purely repulsive model to represent an ensemble of precessing rods. The rods are composed of two types of particles: red and white, as shown in Fig. 5.2b. The repulsive potential between red-red is the WCA potential, as mentioned in Section 2.2. However, the red-white potential is a soft-core potential [143] reflecting the finite strength of the precession barrier preventing rods from freely diffusing. This potential is given as

$$U_{rw} = 4\epsilon\lambda^b \left[\frac{1}{w^2} - \frac{1}{w}\right], \tag{5.13}$$

where the activation parameter $\lambda = 0.1$, $b = 1$, $w = p\,(1-\lambda)^2 + (r/d)^6$, where $p = 1/2$, and r is the bead-bead distance below the cut off $r = 1.1\mathrm{d}$ when the potential reaches zero ($U_{rw}\,(r = 1.1d) = 0$). These parameters result in a soft core barrier of 2 k_BT.

The simulation begins with 1000 rods randomly distributed in a cubic box with periodic boundaries. We integrate time using an NPT ensemble using a time step of 0.001 τ. Like the magnetic MD model, the temperature is controlled by Langevin dynamics and the pressure is maintained using the Nosé-Hoover algorithm [144]. We apply a slow pressure ramp to maintain quasi-constant pressure beginning at $P\sigma^3/\epsilon = 0.1$ to 1.0, encompassing the relevant range of densities in which the nematic-smectic transition occurs. The box axes are allowed to relax anisotropically with the x and y axes coupled for visual convenience. The transition from nematic to smectic is defined by the inflection point (i. e. half max smectic order) averaged over 5 simulations.

For the binary mixtures, the same method as the single component simulations was applied with $3,456$ rods, randomly distributed in an initially cubic box, ($1:1$ mixture of $l/d = 4$, $\beta = 29°$, $\sigma = 0.97$; $l/d = 8$, $\beta = 12°$, $s = 1.0$). This combination is consistent with rods under a field precessing at $\theta = 40°$ and $\omega = 0.14/\tau$. The difference in their l/d and σ ($\sim \mu^{1/3}$) alone result in a different angle of precession. In this case, the implicit magnetic coupling remains below one ($\Gamma = 0.06$ and 0.07 for the $l/d = 4$ and $l/d = 8$, respectively). In addition, the reduced diffusion is also small ($D' = 2 \times 10^{-3}$ and 10^{-3} for the $l/d = 4$ and $l/d = 8$, respectively).

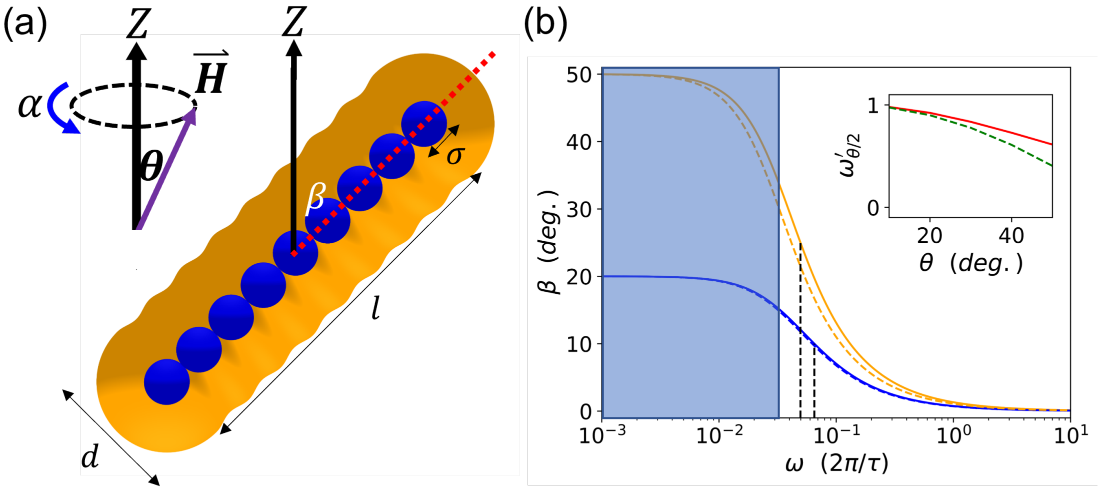

Figure 5.1. Precession of a superparamagnetic rod. (a) Schematic for a magnetic field $\boldsymbol{H}$ precessing around the z-axis at a precession angle θ. A rod composed of a stiff chain of superparamagnetic particles (blue) of diameter σ are coated by a non-magnetic material (orange); the coating determines its aspect ratio l/d. The rod orientation is measured by its angle β to the precession (z) axis. (b) The external field $\boldsymbol{H}$ drives rod precession for $\theta = 20°$ and $50°$. As the field precession frequency ω increases, β decreases. The blue shaded region highlights when the diffusion time over the rod area is less than the precession period. (inset) The reduced frequency at which $\beta = \theta/2$ as a function θ for simulated (red) and theory (green dash).

5.3. Results and Discussion

The viscous drag on a rotating superparamagnetic rod significantly impacts its motion in precessing magnetic fields. The rod's precession angle β and azimuthal phase lag ϕ must result in a magnetic torque (Eq. 5.4) that balances the drag torque (Eq. 5.6). We show in Fig. 5.1b the curve describing the rod precession angle β as a function of the field precession frequency ω (for $\theta = 20°$ and $50°$). In the static field limit (small ω), the rod precession matches the field angle $\beta = \theta$. As ω increases, $\beta \to 0$ according to Eq. 5.8, having good agreement with MD simulations.

To uniquely determine β, two variables must be known: θ and the reduced field frequency ω'. This dimensionless parameter from Eq. 5.9 rescales ω relative to the magnetoviscous response frequency of the rod, and otherwise acts conceptually identical to the field frequency. In Eq. 5.8, we theoretically derive $\beta(\theta, \omega')$ and produce a curve (Fig. 5.1b, dashed line) nearly identical to that of MD simulations (Fig. 5.1b, solid line).

The inflection point in the $\beta\left(\theta, \omega'\right)$ curve is a characteristic frequency at which $\beta = \theta/2$. In Eq. 5.10, we expand Eq. 5.8 in a power series to obtain a simple relationship to predict the characteristic frequency $\omega'_{\theta/2}$, which remains accurate for small precession angles (Fig. 5.1b, inset). This frequency is well-defined at experimentally realizable intermediate frequencies and is useful as a way of describing the system's precession properties, such as the reduced diffusion constant $D'\left(\omega\right)$ from Eq. 5.9.

Precession induced properties are dependent on $D' \ll 1$ because this is the regime where the precession period is shorter than the diffusion time across the precession barrier. In Fig. 5.1b, we shade the region where the rods diffuse faster than the field precesses. Diffusion time decreases with decreasing temperature; however, the temperature cannot be arbitrarily lowered because the magnetic coupling Γ $1/T$ must also be less than 1 to ensure thermal energy dominates over magnetic-induced effects. We control the magnetic coupling by coating the rods with a non-magnetic layer. Increasing the distance between superparamagnetic dipoles rapidly decreases Γ $1/d^3$. The magnetic coupling can also be decreased by weakening the magnetic field, but doing so may collapse orientational (nematic) order [145] (Fig. 5.2a, inset). From Fig. 5.2a, we see that for any reasonable magnitude for the dipole moment μ, the magnetic coupling Γ quickly decays to below 1 when the thickness of the passive layer is on the order of the magnetic particle diameter.

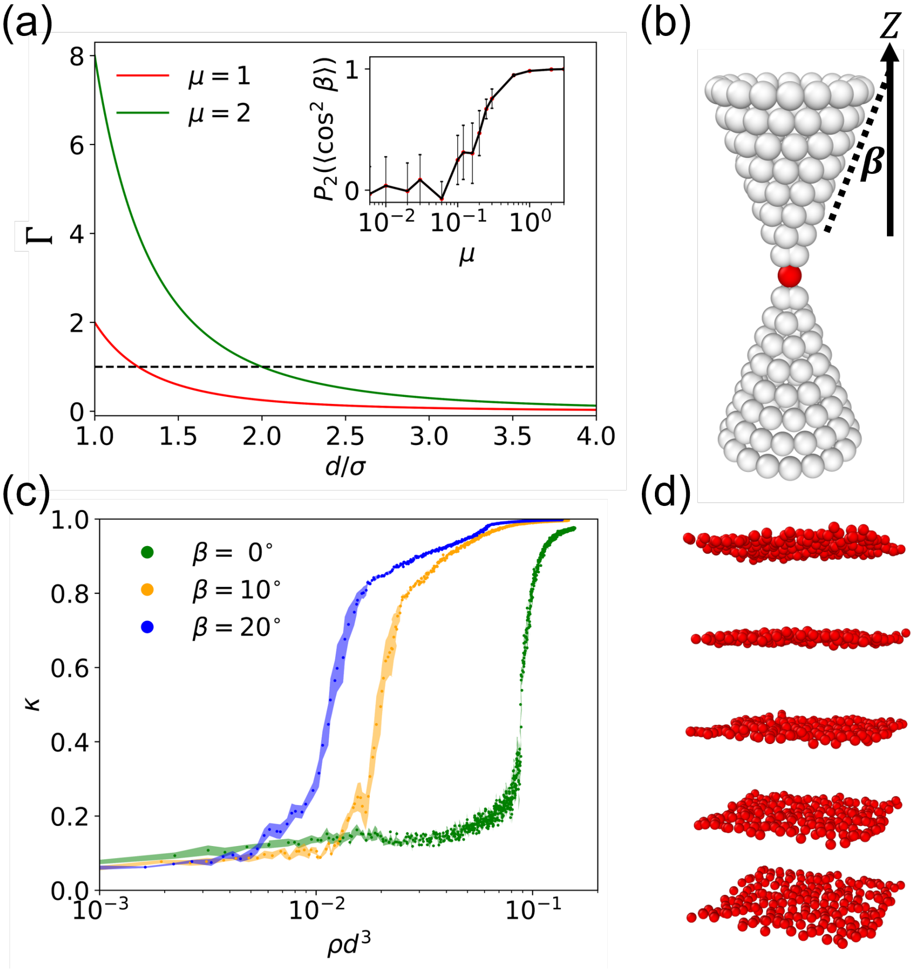

Figure 5.2. (a) The magnetic coupling $\Gamma(\ 1/d^3)$ decreases as the distance between dipoles ($\mu = 1$ (red) and 2 (green)) increases. (a, inset) The orientational order of magnetic rods as μ increases with error bars representing one standard error in the order. (b) Steric MD model, that assumes small Γ, where the red bead is the centre of precession for a rod ($l/d = 8$) and the white beads fill the skin of a double-cone matching the rod precession angle β. (c) The smectic order of the steric model at various precession angles showing how increasing β decreases the transition density. Shaded areas represent one standard error. (d) Steric model in the smectic phase; for clarity, only the red centre beads are shown.

For our model, we consider rods coated by a σ thick passive layer, where σ is the diameter of the magnetic nanoparticles, for a total rod diameter of 3σ.

With the conditions $D' \ll 1$ and $\Gamma \ll 1$ met, we introduce the purely steric "strong precession" model, described in detail in the Methods section. The skin of a double-cone, swept out by the rod, is treated as a soft barrier to the centres of other rods (Fig. 5.2b). Since, the rods are in-phase, the beads in the white "double-cone" beads can overlap with white beads in other rods. This model specifies β as a constant, which implicitly sets θ and ω' without needing to perform dipole-dipole calculations. In Fig. 5.2c, we show that the transition to the layered (smectic) phase occurs at a lower density for larger precession angles. The transition is defined by the density at which the system reaches half the maximum smectic order. The centres of the rods in the smectic phase can be seen in Fig. 5.2d. Obscuring the white beads allows us to see the disordered layers that indicate a small magnetic coupling regime.

We observe the same density suppression for the nematic-smectic transition using the full magnetic MD model. The sharpness of the transition and the maximum smectic order depends on the strength of the precession barrier. As the system density increases, the collision frequency between rods increases and results in a continuous transition to the smectic phase, given a constant β (Fig 5.3b). The magnetic MD model is not in the strong precession limit, therefore, the density required to induce the nematic-smectic transition is slightly higher than the steric model (Fig. 5.3c). This indicates that the precession barrier is easier to diffuse across meaning that different temperatures can be modelled by adjusting the energy barrier in the steric model. Finally we should note that, the MD

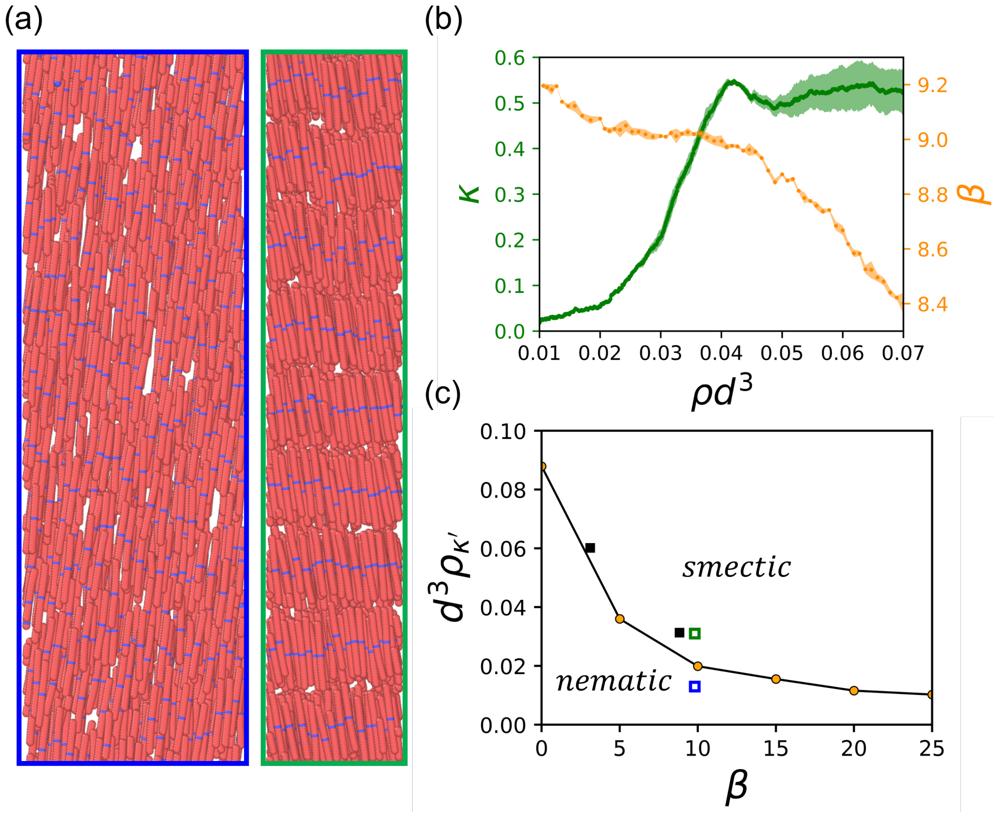

Figure 5.3. (a) Magnetic MD model below (left) and above (right) the nematic-smectic transition ($\theta = 20°$, $\omega' = 0.2$). (b) The smectic order κ and rod angle β for the magnetic MD model as the system density ρd^3 increases. (c) The phase diagram separating the nematic and smectic regions. The orange data is the strong precession model and the black squares denote the observed transition from the magnetic MD model, with green and blue highlight snapshots from (a).

model validates the steric model's assumption that the precession angle does not change by showing that the transition occurs over densities with negligible changes to β.

In Fig. 5.4, we use for the steric model to investigate the behaviour of binary mixtures of different length rods, $l/d = 4$ (cyan) and 8 (red), where the system would normally be too large to investigate using the magnetic mode. We see synchronization-driven phase separation occurring due to the steric repulsion of incompatibly precessing rods [146].

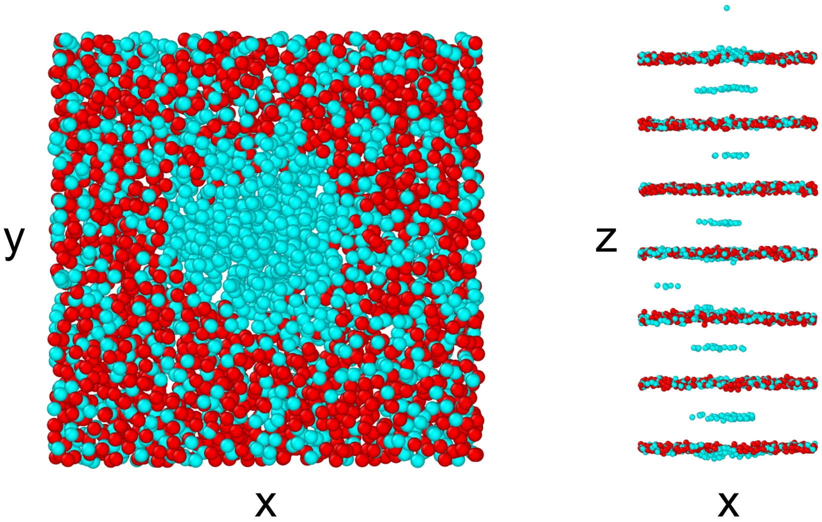

Figure 5.4. A (50% cyan $l/d = 4$: 50% red $l/d = 8$) binary mixture of rods in the smectic regime, centres shown for clarity.

We observe two phases: a mixed phase and a phase rich in short rods. The short rods precess at a larger angle and therefore the steric cost of the mixed phase decreases more with a short rod rich phase than a long rod rich phase. Full segregation does not occur due to the entropy of the diffusing rods. The presence of the interstitial layers suggests possible consequence of local alignment. In the absence of sufficient fluctuations or shear forces, layers may stabilize defects such as two regions of the long-rod phase offset by one short-rod layer.

5.4. Conclusions

In summary, the density at which the nematic-to-smectic transition occurs in a system of precessing rods decreases with increasing precession angle. We show this effect using a purely steric molecular dynamics model and validate it in a superparamagnetic system. Systems with rods of disparate lengths will phase separate and can form stable defects in the smectic layers. Future work is needed to define the phase boundaries present in systems of binary mixtures. We anticipate that a better understanding of liquid crystal phase transitions in dynamic magnetic fields will advance the design and control of liquid crystal-based devices.

CHAPTER 6

Summary and Outlook

6.1. Dissertation Summary

This dissertation used a combination of theory and simulation to address contemporary problems in magnetoelastic membranes and superparamagnetic crystals. Throughout, I use dimensionless parameters to express each problem in a manner that holds the most physical relevance possible; doing so allows the reader to learn how competing forces shape the system, using a single number. In Chapter 2, we saw how the magnetoelastic parameter dictates the conformation of the membrane in a fast precessing field and how that directs the forces along the membrane's perimeter. We found by simulation and later *via* analytical solutions, that the magnitude of the force is significantly affected by spontaneous symmetry breaking in the membrane configuration. In the next chapter, we added a surrounding fluid and lowered the field precession frequency, which allows the viscous forces to affect the membrane dynamics and the system was defined by the magnetoviscous parameter. The magnetoviscous parameter controlled the membrane undulation amplitude and, in turn, the displacement of the center-of-mass during swimming. Furthermore, we showed using the lattice Boltzmann method and the Stokeslet, that the swimming velocity is linearly proportional to the membrane asymmetry. These works show how engineers and physics that create a magnetic membrane must consider the symmetry induced by the magnetic field as well as how the membrane's intrinsic symmetry implicates desired properties. The membrane projects influenced our approach on magnetic crystals in part two, as in each case, the system could be understood as magnetic forces balancing out a competing force that resisted the dipolar interactions: the elastic bending and the fluid drag, respectively. In Chapter 4, the most important quantity that explains the morphological differences between rough and smooth crystalline rods is the superparamagnetic coupling parameter, a ratio between the magnetic and thermal energies. Finally, the magnetoviscous analysis from part 1 allowed us to imagine how a far-from-equilibrium system can be used to generate crystalline order. We demonstrated this was the case by analytically describing the precession of a magnetic rod using relative precession frequency with similar viscomagnetic properties as seen in Chapter 3. Ultimately, these works strove to develop simple mathematical relationships between pertinent system properties and dimensionless control parameters in order to confer physical intuition. By doing so, we lay the foundation for the facile design of superparamagnetic soft matter systems that convey the proper symmetries to address future technological advancement.

6.2. Outlook for Future Work

6.2.1. Magnetoelastic Membranes

Membrane fabrication. The fabrication of magnetoelastic membranes have been exceedingly difficult. While many groups have successfully synthesized a monolayer of superparamagnetic particles in a variety of symmetries [14, 147–150], connecting them and liberating a specific area has proved challenging. For experimentalists, a combination of

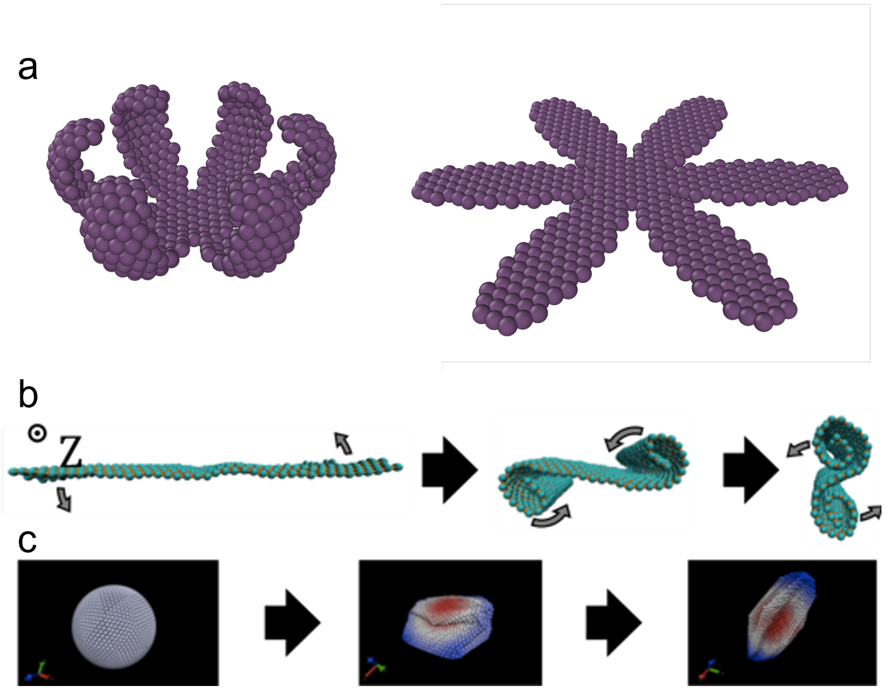

Figure 6.1. (a) A membrane petal with intrinsic curvature, left, can be opened with a large-angle precessing field, right. (b) A square membrane forced to lie in along the precession axis, will curl similar to filaments in a precessing field. (c) Closed membrane spheres, left, will deform in the presence of a large-angle precessing field, middle, and a small-angle precessing field, right.

bottom-up and top-down approaches may prove useful. For instance, the colloid monolayer could be dispersed between polydimethylsiloxane (PDMS) layers [151]. This method would allow membranes of any shape to be synthesized using standard photolithography. In addition, the layers can be stretched when deposited to optionally introduce intrinsic curvature. Another possibility is to form a monolayer of colloids that can chemically bond with sticky DNA [92], streptavidin-biotin [56, 57, 152], or a fusible polymers.

Impact of membrane symmetry. We showed in Chapter 3 that the continuous symmetry measure [88] of the truncated membrane directly affect membrane locomotion. How a membrane bends in response to the field will also depend on edge effects that is the focus of stress is determined by the shape of the perimeter [153], which we could largely ignore using a (mostly) circular membrane. Since the locomotion velocity depends on the bending amplitude and the shape symmetry, more research needs to be done on how different symmetries affect and investigate whether or not there is a rigorous relationship between the continuous symmetry measure and membrane displacement in a viscous fluid.

Impact of membrane fluctuations and edge effects. Nanoparticles are subject to thermal fluctuations from the environment. When incorporated in a fluid or crystalline membrane, these fluctuations can contribute to out-of-plane distortions that result in non-zero Gaussian curvature. These effects dramatically alter the mechanical properties of atomic films, like graphene [154], as well as colloidal membranes [155]. Noteably, this phenomenon will prevent crumpling, but will also rescale (increasing for crystalline, and decreasing for fluid) the bending modulus linearly with temperature [156, 157]. In particular, edge effects can drive topological changes by acting as a source for the phonon-mediated membrane fluctuations, as well as dictating the shape of the resulting curvature [155, 158].

Membrane ensembles. Further investigation into systems of multiple membranes are needed. The fluid flow during the “wobbling” precession generates many vortices that should induce an outward hydrodynamic repulsion of neighboring membranes in the membrane plane and in the direction of the precession axis. However, the external field ensures that all membranes remain in-phase with each other. This means that the repulsion would be minimized when the membrane are in-plane or vertically stacked. Therefore, systems of circular magnetoelastic membranes will form a hexagonally-packed liquid crystal. Disruption to the membrane circular symmetry will induce hydrodynamic

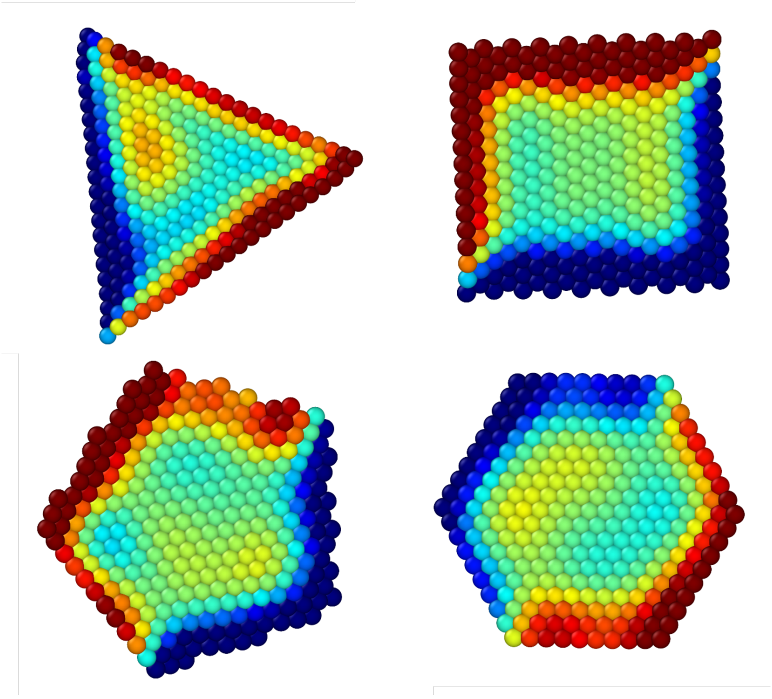

Figure 6.2. Various membrane shapes in large-angle precessing field. The color shows displacement in the direction of the precession axis.

distortions that, if they do not destabilize the crystal, would cause phonon-like motion in the crystal lattice.

6.2.2. Colloidal Magnetic Crystals

Controlling crystal shape and defects. Further shape control may be accomplished by moving beyond a static field. For instance, preliminary results suggest that flat discoidal crystals of a variety of symmetries may be formed form rotating magnetic fields (Fig. 6.3. Once the magnetic crystal is formed, there is great potential to further manipulate it. When a crystal is made from superparamagnetic particles, it retains its superparamagnetic properties, even if the crystal size has passed when the superparamagnetic-ferromagnetic transition would have occurs in bulk magnetite [107]. It will not magnetically aggregate

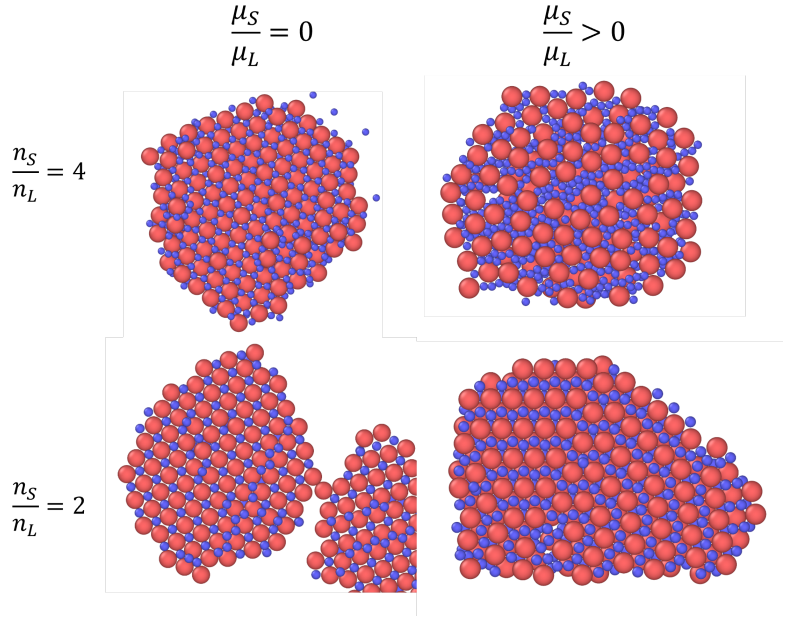

Figure 6.3. Colloidal crystals in a rotating magnetic field with various number n and dipole ratios μ ratios.

with other crystals, but can be actuated by an externally applied field. The mechanical properties of the crystal can be examined by forming pillars on a sticky substrate, where the magnetic field is initially perpendicular to the surface to grow the rods and then applied in parallel to analyze their buckling and oscillatory behavior [**cebers20016flexible**]. Of course, the mechanics of a crystal are dependent on present defects. Further investigation must be made in using magnetic fields to control grain size and prevent cracks under stress [159].

Liquid crystal hydrodynamics. The hydrodynamics of a precessing ellipsoidal particles in a viscous fluid is known analytically [160]. Camassa *et al.* show that, as a rod precessing, the fluid around it oscillates both perpendicularly and in parallel to the precession axis. The hydrodynamic behavior of an ensemble of precessing rods is unknown and, presumably, may be insignificant with a random distribution of rods, even in the nematic phase. However, we know that as magnetic repulsion increases in a system of magnetic beads and rods, a hexagonal arrangement develops. In this repulsive regime, the smectic phase would essentially become more like a solid crystal, where rod diffusion drops considerably. An interesting route of study would be the transmission of phonons that occur do to hydrodynamically induce oscillations in neighboring precessing rods.

Bibliography

[1] Wasilewski, P. & Kletetschka, G. Lodestone: Natures only permanent magnet-What it is and how it gets charged. *Geophysical research letters* **26,** 2275–2278 (1999).

[2] Mourino, M. R. From Thales to Lauterbur, or from the lodestone to MR imaging: magnetism and medicine. *Radiology* **180,** 593–612 (1991).

[3] Gilbert, W. *De magnete* (Courier Corporation. Translation by P. F. Mottelay., 1958).

[4] Hu, W., Lum, G., Mastrangeli, M. & Sitti, M. Small-scale soft-bodied robot with multimodal locomotion. *Nature* **554,** 81–85 (2018).

[5] Li, C., Lau, G. C., Yuan, H., Aggarwal, A., Dominguez, V. L., Liu, S., Sai, H., Palmer, L. C., Sather, N. A., Pearson, T. J., Freedman, D. E., Amiri, P. K., de la Cruz, M. O. & Stupp, S. I. Fast and programmable locomotion of hydrogel-metal hybrids under light and magnetic fields. *Science Robotics* **5,** eabb9822 (2020).

[6] Purcell, E. M. Life at low Reynolds number. *Am. J. Phys.* **45,** 3–11 (1977).

[7] Cong, H., Yu, B., Tang, J., Li, Z. & Liu, X. Current status and future developments in preparation and application of colloidal crystals. *Chem. Soc. Rev.* **42,** 7774–7800 (2013).

[8] Jiang, C., Leung, C. W. & Pong, P. W. Magnetic-field-assisted assembly of anisotropic superstructures by iron oxide nanoparticles and their enhanced magnetism. *Nanoscale Res. Lett.* **11,** 1–12 (2016).

[9] Li, F., Josephson, D. P. & Stein, A. Colloidal assembly: the road from particles to colloidal molecules and crystals. *Angewandte Chemie International Edition* **50,** 360–388 (2011).

[10] Onsager, L. The effects of shape on the interaction of colloidal particles. *Ann. N. Y. Acad. Sci.* **51,** 627–659 (1949).

[11] Driscoll, M., Delmotte, B., Youssef, M., Sacanna, S., Donev, A. & P., C. Unstable fronts and motile structures formed by microrollers. *Nat Phys* **13,** 375–379 (2017).

[12] Kaiser, A. & Snezhko A.and Aranson, I. S. Flocking ferromagnetic colloids. *Sci Adv* **3,** e1601469 (2017).

[13] Liu, Q., Ackerman, P. J., Lubensky, T. C. & Smalyukh, I. I. Biaxial ferromagnetic liquid crystal colloids. *Proc Natl Acad Sci U S A* **113,** 10479–10484 (2016).

[14] Spiteri, L., Messina, R., Gonzalez-Rodriguez, D. & L., B. Ordering of sedimenting paramagnetic colloids in a monolayer. *Phys Rev E* **98,** 020601 (2018).

[15] Kim, E., Stratford, K. & Cates, M. E. Bijels Containing Magnetic Particles: A Simulation Study. *Langmuir* **26,** 7928–7936 (2010).

[16] Li, H., Halsey, T. C. & Lobkovsky, A. Singular Shape of a Fluid Drop in an Electric or Magnetic Field. *Europhys Lett* **27,** 575–580 (1994).

[17] Kamien, R. D. & Nelson, D. R. Directed Polymer Melts and Quantum Critical Phenomena. *J Stat Phys* **71,** 23–50 (1993).

[18] Zrinyi, M., Barsi, L. & Buki, A. Ferrogel: a new magneto-controlled elastic medium. *Polymer Gels and Networks* **5,** 415–427 (1997).

[19] Dreyfus, R., Baudry, J., Roper, M. L., Fermigier, M., Stone, H. A. & J., B. Microscopic artificial swimmers. *Nature* **437,** 862–865 (2005).

[20] Wei, J., Song, F. & Dobnikar, J. Assembly of Superparamagnetic Filaments in External Field. *Langmuir* **32,** 9321–9328 (2016).

[21] Dempster, J. M., Vázquez-Montejo, P. & de la Cruz, M. O. Contractile actuation and dynamical gel assembly of paramagnetic filaments in fast precessing fields. *Phys. Rev. E* **95,** 052606 (2017).

[22] Faraudo, J., Andreu, J. S., C., C. & J., C. Predicting the Self-Assembly of Superparamagnetic Colloids under Magnetic Fields. *Adv Funct Mater* **26,** 3837–3858 (2016).

[23] Mahmoudi, M., Sant, S., Wang, B., Laurent, S. & Sen, T. Superparamagnetic iron oxide nanoparticles (SPIONs): Development, surface modification and applications in chemotherapy. *Adv Drug Deliv Rev* **63,** 24–46 (2011).

[24] Sabale, S., Kandesar, P., Jadhav, V., Komorek, R., Motkuri, R. K. & Yu, X. Recent developments in the synthesis, properties, and biomedical applications of core/shell superparamagnetic iron oxide nanoparticles with gold. *Biomater Sci* **5,** 2212–2225 (2017).

[25] Furst, E. M., Suzuki, C., Fermigier, M. & Gast, A. P. Permanently Linked Monodisperse Paramagnetic Chains. *Langmuir* **14,** 7334–7336 (1998).

[26] Ido, Y., Li, Y., Tsutsumi, H., Sumiyoshi, H. & Chen, C. Magnetic microchains and microswimmers in an oscillating magnetic field. *Biomicrofluidics* **10,** 011902 (2016).

[27] Vilfan, M., Potočnik, A., Kavčič, B., Osterman, N., Poberaj, I., Vilfan, A. & Babič, D. Self-assembled artificial cilia. *Proc Natl Acad Sci U S A* **107,** 1844–1847 (2010).

[28] Bannwarth, M. B., Utech, S., Ebert, S., Weitz, D. A., Crespy, D. & Landfester, K. Colloidal Polymers with Controlled Sequence and Branching Constructed from Magnetic Field Assembled Nanoparticles. *Nano Lett* **9,** 2720–2728 (2015).

[29] Kralj, S. & Makovec, D. Magnetic Assembly of Superparamagnetic Iron Oxide Nanoparticle Clusters into Nanochains and Nanobundles. *ACS Nano* **9,** 9700–9707 (2015).

[30] Geng, B. Y., Ma, J. Z., Liu, X. W., Du, Q. B., Kong, M. G. & Zhang, L. D. Hydrophilic polymer assisted synthesis of room-temperature ferromagnetic Fe3O4 nanochains. *Appl Phys Lett* **90,** 043120 (2007).

[31] Vázquez-Montejo, P. & de la Cruz, M. O. Flexible paramagnetic membranes in fast precessing fields. *Phys. Rev. E* **98,** 032603 (2018).

[32] Smallenburg, F. & Dijkstra, M. Phase diagram of colloidal spheres in a biaxial electric or magnetic field. *J Chem Phys* **132,** 204508 (2010).

[33] Osterman, N., Poberaj, I., Dobnikar, J., Frenkel, D., Ziherl, P. & Babić, D. Field-Induced Self-assembly of Suspended Colloidal Membranes. *Phys Rev Lett* **103** (2009).

[34] Weeks, J. D., Chandler, D. & Andersen, H. C. Role of Repulsive Forces in Determining the Equilibrium Structure of Simple Liquids. *J. Chem. Phys.* **54,** 5237–5247 (1971).

[35] Plimpton, S. Fast Parallel Algorithms for Short-Range Molecular Dynamics. *J Comput Phys* **117,** 1–19 (1 1995).

[36] Humphrey, W., Dalke, A. & Schulten, K. VMD: Visual molecular dynamics. *J Mol Graph* **14,** 33–38 (1 1996).

[37] Brisbois, C. A., Tasinkevych, M., Vàzquez-Montejo, P. & de la Cruz, M. O. Actuation of magnetoelastic membranes in precessing magnetic fields. *Proc. Natl. Acad. Sci. USA* **116,** 2500–2505 (2019).

[38] Laug, P. & Borouchaki, H. *The BL2D Mesh Generator: Beginner's Guide, User's and Programmer's Manual* tech. rep. RT-0194 (INRIA, 1996), 44.

[39] Gilbert, J. C. & Lemaréchal, C. Some numerical experiments with variable-storage quasi-Newton algorithms. *Math Program* **45,** 407–435. ISSN: 1436-4646 (1989).

[40] Seung, H. S. & Nelson, D. R. Defects in flexible membranes with crystalline order. *Phys Rev A* **38** (1988).

[41] Vázquez-Montejo, P., Dempster, J. M. & de la Cruz, M. O. Paramagnetic filaments in a fast precessing field: Planar versus helical conformations. *Phys Rev Mater* **1,** 064402 (2017).

[42] Capovilla, R. & Guven, J. Stresses in lipid membranes. *J Phys A Math Gen* **35,** 6233 (2002).

[43] Capovilla, R., Chryssomalakos, C. & Guven, J. Hamiltonians for curves. *J Phys A Math Gen* **35,** 6571 (2002).

[44] Diamant, H. & Witten, T. A. Compression Induced Folding of a Sheet: An Integrable System. *Phys Rev Lett* **107,** 164302 (2011).

[45] Zhu, L. & Chen, X. Mechanical analysis of eyelid morphology. *Acta Biomater* **9,** 7968–7976 (2013).

[46] Stoop, N. & Müller, M. M. Non-linear buckling and symmetry breaking of a soft elastic sheet sliding on a cylindrical substrate. *Int J Non Linear Mech* **75,** 115–122 (2015).

[47] Flynn, J. D., McGlinchey, R. P., Walker III, R. L. & Lee, J. C. Structural features of α-synuclein amyloid fibrils revealed by Raman spectroscopy. *J Biol Chem* **293,** 767–776 (2018).

[48] Zhang, S., Andreasen, M., Nielsen, J. T., Liu, L., Nielsen, E. H., Song, J., Ji, G., Sun, F., Skrydstrup, T., Besenbacher, F., Nielsen, N. C., Otzen, D. E. & Dong, M. Coexistence of ribbon and helical fibrils originating from hIAPP20–29 revealed by quantitative nanomechanical atomic force microscopy. *Proc Natl Acad Sci U S A* **110,** 2798–2803 (2013).

[49] Moyer, T. J., Cui, H. & Stupp, S. I. Tuning Nanostructure Dimensions with Supramolecular Twisting. *J Phys Chem B* **117,** 4604–4610 (2013).

[50] Dombrowski, T. & Klotsa, D. Kinematics of a simple reciprocal model swimmer at intermediate Reynolds numbers. *Phys. Rev. Fluids* **5,** 063103 (2020).

[51] Dreyfus, R., Baudry, J., Roper, M., Fermigier, M., Stone, H. & Bibette, J. Microscopic Artificial Swimmers. *Nature* **437,** 862–865 (2005).

[52] Jang, B., Gutman, E., Stucki, N., Seitz, B. F., Wendel-García, P. D., Newton, T., Pokki, J., Ergeneman, O., Pané, S., Or, Y. & Nelson, B. J. Undulatory Locomotion of Magnetic Multilink Nanoswimmers. *Nano Lett.* **15,** 4829–4833 (2015).

[53] Bryan, M. T., Garcìa-Torres, J., Martin, E. L., Hamilton, J. K., Calero, C., Petrov, P. G., Winlove, C. P., Pagonabarraga, I., Tierno, P., Sagués, F. & Ogrin, F. Y.

Microscale Magneto-Elastic Composite Swimmers at the Air-Water and Water-Solid Interfaces Under a Uniaxial Field. *Phys. Rev. Appl.* **11,** 044019 (2019).

[54] Moerland, C. P., van IJzendoorn, L. J. & Prins, M. W. J. Rotating magnetic particles for lab-on-chip applications – a comprehensive review. *Lab Chip* **19,** 919–933 (2019).

[55] Goubault, C., Jop, P., Fermigier, M., Baudry, J., Bertrand, E. & Bibette, J. Flexible Magnetic Filaments as Micromechanical Sensors. *Phys. Rev. Lett.* **91,** 260802 (2003).

[56] Biswal, S. L. & Gast, A. P. Mechanics of semiflexible chains formed by poly(ethylene glycol)-linked paramagnetic particles. *Phys. Rev. E* **68,** 021402 (2003).

[57] Biswal, S. L. & Gast, A. P. Micromixing with Linked Chains of Paramagnetic Particles. *J. Anal. Chem.* **76,** 6448–6455 (2004).

[58] Zhu, W., Li, J., Leong, Y. J., Rozen, I., Qu, X., Dong, R., Wu, Z., Gao, W., Chung, P. H., Wang, J. & Chen, S. 3D-Printed Artificial Microfish. *Adv. Mater.* **27,** 4411–4417 (2015).

[59] Wu, Z., Li, T., Gao, W., Xu, T., Jurado-Sánchez, B., Li, J., Gao, W., He, Q., Zhang, L. & Wang, J. Cell-Membrane-Coated Synthetic Nanomotors for Effective Biodetoxification. *Adv. Funct. Mater.* **25,** 3881–3887 (2015).

[60] Wu, S., Hu, W., Ze, Q., Sitti, M. & Zhao, R. Multifunctional magnetic soft composites: a review. *Multifunct. mater.* **3,** 042003 (2020).

[61] Vyskocil, J., Mayorga-Martinez, C. C., Jablonská, E., Novotný, F., Ruml, T. & Pumera, M. Cancer Cells Microsurgery via Asymmetric Bent Surface Au/Ag/Ni Microrobotic Scalpels Through a Transversal Rotating Magnetic Field. *ACS Nano* **14,** 8247–8256 (2020).

[62] Markides, H., Rotherham, M. & Haj, A. Biocompatibility and Toxicity of Magnetic Nanoparticles in Regenerative Medicine. *J. Nanomater.* **2012,** 13 (2012).

[63] Li, Y., Huang, G., Zhang, X., Li, B., Chen, Y., Lu, T., Lu, T. J. & Xu, F. Magnetic Hydrogels and Their Potential Biomedical Applications. *Adv. Funct. Mater.* **23,** 660–672 (2013).

[64] Roper, M., Dreyfus, R., Baudry, J., Fermigier, M., Bibette, J. & Stone, H. A. Do magnetic micro-swimmers move like eukaryotic cells? *Proc. R. Soc. Lond. A* **464,** 877–904 (2008).

[65] Yang, T., Sprinkle, B., Guo, Y., Qian, J., Hua, D., Donev, A., Marr, D. W. M. & Wu, N. Reconfigurable microbots folded from simple colloidal chains. *Proc. Natl. Acad. Sci. U.S.A.* **117,** 18186–18193 (2020).

[66] Cebers, A. Flexible magnetic swimmer. *Magnetohydrodynamics* **41,** 63–72 (2005).

[67] Arroyo, M., Heltai, L., Millán, D. & DeSimone, A. Reverse engineering the euglenoid movement. *Proc. Natl. Acad. Sci. U.S.A.* **109,** 17874–17879 (2012).

[68] Taylor, G. I. Analysis of the swimming of microscopic organisms. *Proc. R. Soc. Lond. A* **209,** 447–461 (1951).

[69] Lauga, E. & Powers, T. R. The hydrodynamics of swimming microorganisms. *Reports on Progress in Physics* **72,** 096601 (2009).

[70] Corsi, G., De Simone, A., Maurini, C. & Vidoli, S. A neutrally stable shell in a Stokes flow: a rotational Taylor's sheet. *Proc. R. Soc. Lond. A* **475,** 20190178 (2019).

[71] Stukowski, A. Visualization and analysis of atomistic simulation data with OVITO-the Open Visualization Tool. *Model. Simul. Mat. Sci. Eng.* **18** (2010).

[72] Mackay, F., Ollila, S. & Denniston, C. Hydrodynamic forces implemented into LAMMPS through a lattice-Boltzmann fluid. *Comput. Phys. Commun.* **184,** 2021–2031. ISSN: 0010-4655 (2013).

[73] Peskin, C. S. The immersed boundary method. *Acta. Numer.* **11,** 479–517 (2002).

[74] Bhatnagar, P. L., Gross, E. P. & Krook, M. A Model for Collision Processes in Gases. I. Small Amplitude Processes in Charged and Neutral One-Component Systems. *Phys. Rev.* **94,** 511–525 (1954).

[75] Krüger, T., Kusumaatmaja, H., Kuzmin, A., Shardt, O., Silva, G. & Viggen, E. M. *The Lattice Boltzmann Method - Principles and Practice* (Springer International Publishing, 2017).

[76] Adhikari, R., Stratford, K., Cates, M. E. & Wagner, A. J. Fluctuating lattice Boltzmann. *EPL* **71,** 473–479 (2005).

[77] Magnetoelastic membrane with stiffness $\kappa = 10$ under a magnetic field, $\mu = 1.5$, $\theta = 70°$, and $\omega = 0.06$. The coloration highlights the displacement in the z-direction. See Video 1 in Supplemental Material.

[78] Lim, M. X., VanSaders, B., Souslov, A. & Jaeger, H. M. Mechanical Properties of Acoustically Levitated Granular Rafts. *Phys. Rev. X* **12,** 021017 (2022).

[79] Yung, K. W., Landecker, P. B. & Villani, D. D. An analytic solution for the force between two magnetic dipoles. *Magn. Electr. Separ.* **9,** 39–52 (1998).

[80] Park, S. S., Urbach, Z. J., Brisbois, C. A., Parker, K. A., Partridge, B. E., Oh, T., Dravid, V. P., Olvera de la Cruz, M. & Mirkin, C. A. DNA-and Field-Mediated

Assembly of Magnetic Nanoparticles into High-Aspect Ratio Crystals. *Adv. Mater.* **32,** 1906626 (2020).

[81] Messina, R., Aljawhari, S., Bécu, L., Schockmel, J., Lumay, G. & Vandewalle, N. Quantitatively mimicking wet colloidal suspensions with dry granular media. *Sci. Rep.* **5,** 10348 (2015).

[82] Magnetoelastic membrane with stiffness $\kappa = 20$ under a magnetic field, $\mu = 1.5$, $\theta = 60^\circ$ and $\omega = 0.013$.. The coloration highlights the displacement in the z-direction. See Video 2 in Supplemental Material.

[83] Cīmurs, J. & Cēbers, A. Dynamics of anisotropic superparamagnetic particles in a precessing magnetic field. *Phys. Rev. E* **87,** 062318 (2013).

[84] Goldstein, H. *Classical Mechanics* 3rd ed., p. 24 (Addison-Wesley, 2000).

[85] Grosjean, G., Hubert, M., Collard, Y., Pillitteri, S. & Vandewalle, N. Surface swimmers, harnessing the interface to self-propel. *Eur. Phys. J. E* **41,** 137. ISSN: 1292-895X (2018).

[86] Tanzosh, J. P. & Stone, H. A. A general approach for analyzing the arbitrary motion of a circular disk in a stokes flow. *Chem. Eng. Commun.* **148,** 333–346 (1996).

[87] Guazzelli, É., Morris, J. F. & Pic, S. *A Physical Introduction to Suspension Dynamics* (Cambridge University Press, 2011).

[88] Zabrodsky, H., Peleg, S. & Avnir, D. Continuous symmetry measures. *J. Am. Chem. Soc.* **114,** 7843–7851 (1992).

[89] Grosjean, G., Hubert, M., Lagubeau, G. & Vandewalle, N. Realization of the Najafi-Golestanian microswimmer. *Phys. Rev. E* **94,** 021101 (2016).

[90] Capuani, F., Pagonabarraga, I. & Frenkel, D. Lattice-Boltzmann simulation of the sedimentation of charged disks. *J. Chem. Phys.* **124,** 124903 (2006).

[91] Susan-Resiga, D., Socoliuc, V., Bunge, A., Turcu, R. & Vékás, L. From high colloidal stability ferrofluids to magnetorheological fluids: tuning the flow behavior by magnetite nanoclusters. *Smart Mater. Struct.* **28,** 115014 (2019).

[92] Cutler, J. I., Auyeung, E. & Mirkin, C. A. Spherical Nucleic Acids. *Journal of the American Chemical Society* **134,** 1376–1391 (2012).

[93] Hu, Y. & Niemeyer, C. M. From DNA nanotechnology to material systems engineering. *Adv. Mater.* **31,** 1806294 (2019).

[94] Wang, S., Park, S. S., Buru, C. T., Lin, H., Chen, P.-C., Roth, E. W., Farha, O. K. & Mirkin, C. A. Colloidal crystal engineering with metal–organic framework nanoparticles and DNA. *Nat. Commun.* **11,** 1–8 (2020).

[95] Macfarlane, R. J., Jones, M. R., Senesi, A. J., Young, K. L., Lee, B., Wu, J. & Mirkin, C. A. Establishing the design rules for DNA-mediated programmable colloidal crystallization. *Angew. Chem. Int. Ed.* **49,** 4589–4592 (2010).

[96] Macfarlane, R. J., Lee, B., Jones, M. R., Harris, N., Schatz, G. C. & Mirkin, C. A. Nanoparticle Superlattice Engineering with DNA. *Science* **334,** 204–208 (2011).

[97] Girard, M., Wang, S., Du, J. S., Das, A., Huang, Z., Dravid, V. P., Lee, B., Mirkin, C. A. & de la Cruz, M. O. Particle analogs of electrons in colloidal crystals. *Science* **364,** 1174–1178 (2019).

[98] Wang, S., Du, J. S., Diercks, N. J., Zhou, W., Roth, E. W., Dravid, V. P. & Mirkin, C. A. Colloidal crystal "alloys". *J. Am. Chem. Soc.* **141,** 20443–20450 (2019).

[99] Rogers, W. B., Shih, W. M. & Manoharan, V. N. Using DNA to program the self-assembly of colloidal nanoparticles and microparticles. *Nat. Rev. Mater.* **1,** 1–14 (2016).

[100] Harraq, A. A., Choudhury, B. D. & Bharti, B. Field-Induced Assembly and Propulsion of Colloids. *Langmuir* **38,** 3001–3016 (2022).

[101] Hill, L. J. & Pyun, J. Colloidal polymers via dipolar assembly of magnetic nanoparticle monomers. *ACS Appl. Mater. Interfaces* **6,** 6022–6032 (2014).

[102] Byrom, J., Han, P., Savory, M. & Biswal, S. L. Directing assembly of DNA-coated colloids with magnetic fields to generate rigid, semiflexible, and flexible chains. *Langmuir* **30,** 9045–9052 (2014).

[103] Bharti, B., Fameau, A.-L., Rubinstein, M. & Velev, O. D. Nanocapillarity-mediated magnetic assembly of nanoparticles into ultraflexible filaments and reconfigurable networks. *Nat. Mater.* **14,** 1104–1109 (2015).

[104] Das, S., Ranjan, P., Maiti, P. S., Singh, G., Leitus, G. & Klajn, R. Dual-responsive nanoparticles and their self-assembly. *Adv. Mater.* **25,** 422–426 (2013).

[105] Toulemon, D., Rastei, M. V., Schmool, D., Garitaonandia, J. S., Lezama, L., Cattoën, X., Bégin-Colin, S. & Pichon, B. P. Enhanced collective magnetic properties induced by the controlled assembly of iron oxide nanoparticles in chains. *Adv. Funct. Mater.* **26,** 2454–2462 (2016).

[106] Ku, J., Aruguete, D. M., Alivisatos, A. P. & Geissler, P. L. Self-assembly of magnetic nanoparticles in evaporating solution. *J. Am. Chem. Soc.* **133,** 838–848 (2011).

[107] Ge, J., Hu, Y., Biasini, M., Beyermann, W. P. & Yin, Y. Superparamagnetic magnetite colloidal nanocrystal clusters. *Angew. Chem. Int. Ed.* **46,** 4342–4345 (2007).

[108] Choi, S., Stassi, S., Pisano, A. P. & Zohdi, T. I. Coffee-Ring Effect-Based Three Dimensional Patterning of Micro/Nanoparticle Assembly with a Single Droplet. *Langmuir* **26,** 11690–11698 (2010).

[109] Park, J.-I., Jun, Y.-w., Choi, J.-s. & Cheon, J. Highly crystalline anisotropic superstructures via magnetic field induced nanoparticle assembly. *Chem. Commun.* 5001–5003 (2007).

[110] Rikken, R. S. M., Nolte, R. J. M., Maan, J. C., van Hest, J. C. M., Wilson, D. A. & Christianen, P. C. M. Manipulation of micro- and nanostructure motion with magnetic fields. *Soft Matter* **10,** 1295–1308 (9 2014).

[111] Spatafora-Salazar, A., Lobmeyer, D. M., Cunha, L. H. P., Joshi, K. & Biswal, S. L. Hierarchical assemblies of superparamagnetic colloids in time-varying magnetic fields. *Soft Matter* **17,** 1120–1155 (5 2021).

[112] Dhakal, S., Kohlstedt, K., Schatz, G., Mirkin, C. & Olvera de la Cruz, M. Growth dynamics for DNA-Guided nanoparticle crystallization. *ACS Nano* **7,** 10948–10959 (2013).

[113] Dünweg, B. & Paul, W. Brownian dynamics simulations without Gaussian random numbers. *Int. J. Mod. Phys. C* **02,** 817–827 (1991).

[114] Schneider, T. & Stoll, E. Molecular-dynamics study of a three-dimensional one-component model for distortive phase transitions. *Phys. Rev. B* **17,** 1302–1322 (1978).

[115] Seo, S. E., Girard, M., de la Cruz, M. O. & Mirkin, C. A. The Importance of Salt-Enhanced Electrostatic Repulsion in Colloidal Crystal Engineering with DNA. *ACS Central Science* **5,** 186–191 (2019).

[116] Humphrey, W., Dalke, A. & Schulten, K. VMD: Visual molecular dynamics. *Journal of Molecular Graphics* **14,** 33–38 (1996).

[117] Haüy, R.-J. *Essai d'une théorie sur la structure des crystaux, appliquée à plusieurs genres de substances crystallisées* (À Paris, Chez Gogué & Née de la Rochelle, Libraires, quote on p. 21, 1784).

[118] Weisstein, E. W. *Haüy Construction* From MathWorld–A Wolfram Web Resource. `https://mathworld.wolfram.com/HauyConstruction.html`.

[119] Andreu, J. S., Camacho, J. & Faraudo, J. Aggregation of superparamagnetic colloids in magnetic fields: the quest for the equilibrium state. *Soft Matter* **7,** 2336–2339 (6 2011).

[120] Wang, M. & Yin, Y. Magnetically responsive nanostructures with tunable optical properties. *J. Am. Chem. Soc.* **138,** 6315–6323 (2016).

[121] Redl, F. X., Cho, K.-S., Murray, C. B. & O'Brien, S. Three-dimensional binary superlattices of magnetic nanocrystals and semiconductor quantum dots. *Nature* **423,** 968–971 (2003).

[122] Petcharoen, K. & Sirivat, A. Magneto-electro-responsive material based on magnetite nanoparticles/polyurethane composites. *Mater. Sci. Eng. C* **61,** 312–323 (2016).

[123] Liu, J., Cai, Y., Deng, Y., Sun, Z., Gu, D., Tu, B. & Zhao, D. Magnetic 3-D ordered macroporous silica templated from binary colloidal crystals and its application for effective removal of microcystin. *Microporous Mesoporous Mater.* **130,** 26–31 (2010).

[124] Zhang, Y., Yue, Q., Zagho, M. M., Zhang, J., Elzatahry, A. A., Jiang, Y. & Deng, Y. Core–Shell magnetic Mesoporous silica microspheres with large Mesopores for enzyme immobilization in biocatalysis. *ACS Appl. Mater. Interfaces* **11,** 10356–10363 (2019).

[125] Rastogi, V., García, A. A., Marquez, M. & Velev, O. D. Anisotropic particle synthesis inside droplet templates on superhydrophobic surfaces. *Macromol. Rapid Commun.* **31,** 190–195 (2010).

[126] Chen, M., Cölfen, H. & Polarz, S. Centrifugal field-induced colloidal assembly: From chaos to order. *ACS Nano* **9,** 6944–6950 (2015).

[127] Etgar, L., Leitus, G., Fradkin, L., Assaraf, Y. G., Tannenbaum, R. & Lifshitz, E. Optical and Magnetic Properties of Conjugate Structures of PbSe Quantum Dots and γ-Fe2O3 Nanoparticles. *ChemPhysChem* **10,** 2235–2241 (2009).

[128] Li, Z., Qian, C., Xu, W., Zhu, C. & Yin, Y. Coupling morphological and magnetic anisotropy for assembling tetragonal colloidal crystals. *Sci. Adv.* **7,** eabh1289 (2021).

[129] Ding, T., Song, K., Clays, K. & Tung, C.-H. Controlled directionality of ellipsoids in monolayer and multilayer colloidal crystals. *Langmuir* **26,** 11544–11549 (2010).

[130] Andrienko, D. Introduction to liquid crystals. *J. Mol. Liq.* **267,** 520–541 (2018).

[131] Iino, H., Kobori, T. & Hanna, J.-i. High Uniformity and High Thermal Stability of Solution-Processed Polycrystalline Thin Films by Utilizing Highly Ordered Smectic Liquid Crystals. *Jpn. J. Appl. Phys.* **51,** 11PD02 (2012).

[132] Hiraoka, K., Stein, P. & Finkelmann, H. Electromechanics of a chiral smectic C elastomer: measurement of complex piezoelectric constant through successive phase transformations. *Macromol. Chem. Phys.* **205,** 48–54 (2004).

[133] Sánchez-Ferrer, A. & Finkelmann, H. Thermal and mechanical properties of new main-chain liquid-crystalline elastomers. *Mol. Cryst. Liq. Cryst.* **508,** 348–710 (2009).

[134] Yoon, J., Baca, A. J., Park, S.-I., Elvikis, P., Geddes, J. B., Li, L., Kim, R. H., Xiao, J., Wang, S., Kim, T.-H., *et al.* Ultrathin silicon solar microcells for semitransparent, mechanically flexible and microconcentrator module designs. *Nat. Mater.* **7,** 907–915 (2008).

[135] Hu, S., Dasbiswas, K., Guo, Z., Tee, Y.-H., Thiagarajan, V., Hersen, P., Chew, T.-L., Safran, S. A., Zaidel-Bar, R. & Bershadsky, A. D. Long-range self-organization of cytoskeletal myosin II filament stacks. *Nat. Cell Biol.* **19,** 133–141 (2017).

[136] Hama, H. Effects of a magnetic field on the nematic-smectic A transition in liquid crystals. *J. Phys. Soc. Jpn.* **54,** 2204–2209 (1985).

[137] Chong, W. H., Chin, L. K., Tan, R. L. S., Wang, H., Liu, A. Q. & Chen, H. Stirring in Suspension: Nanometer-Sized Magnetic Stir Bars. *Angew. Chem. Int. Ed.* **52,** 8570–8573 (2013).

[138] Lu, A.-H., Salabas, E. e. & Schüth, F. Magnetic nanoparticles: synthesis, protection, functionalization, and application. *Angew. Chem. Int. Ed.* **46,** 1222–1244 (2007).

[139] Brisbois, C. A. & de la Cruz, M. O. Locomotion of magnetoelastic membranes in viscous fluids. *Phys. Rev. Research* **4,** 023166 (2022).

[140] Ortega, A. & Garcıa de la Torre, J. Hydrodynamic properties of rodlike and disklike particles in dilute solution. *J. Chem. Phys.* **119,** 9914–9919 (2003).

[141] Schneider, T. & Stoll, E. Molecular-dynamics study of a three-dimensional one-component model for distortive phase transitions. *Phys. Rev. B* **17,** 1302 (1978).

[142] Cifelli, M., Cinacchi, G. & De Gaetani, L. Smectic order parameters from diffusion data. *J. Chem. Phys.* **125,** 164912 (2006).

[143] Beutler, T. C., Mark, A. E., van Schaik, R. C., Gerber, P. R. & Van Gunsteren, W. F. Avoiding singularities and numerical instabilities in free energy calculations based on molecular simulations. *Chem. Phys. Lett.* **222,** 529–539 (1994).

[144] Shinoda, W., Shiga, M. & Mikami, M. Rapid estimation of elastic constants by molecular dynamics simulation under constant stress. *Phys. Rev. B* **69,** 134103 (2004).

[145] Khokhlov, A. & Semenov, A. Influence of external field on the liquid-crystalline ordering in the solutions of stiff-chain macromolecules. *Macromolecules* **15,** 1272–1277 (1982).

[146] Paulo, G. & Tasinkevych, M. Binary mixtures of locally coupled mobile oscillators. *Phys. Rev. E* **104,** 014204 (2021).

[147] Vogel, N., de Viguerie, L., Jonas, U., Weiss, C. K. & Landfester, K. Wafer-Scale Fabrication of Ordered Binary Colloidal Monolayers with Adjustable Stoichiometries. *Advanced Functional Materials* **21,** 3064–3073 (2011).

[148] Euliss, L. E., Grancharov, S. G., O'Brien, S., Deming, T. J., Stucky, G. D., Murray, C. B. & Held, G. A. Cooperative Assembly of Magnetic Nanoparticles and Block Copolypeptides in Aqueous Media. *Nano Letters* **3,** 1489–1493 (2003).

[149] Ahniyaz, A., Sakamoto, Y. & Bergström, L. Magnetic field-induced assembly of oriented superlattices from maghemite nanocubes. *Proceedings of the National Academy of Sciences* **104,** 17570–17574 (2007).

[150] Chen, J., Dong, A., Cai, J., Ye, X., Kang, Y., Kikkawa, J. M. & Murray, C. B. Collective Dipolar Interactions in Self-Assembled Magnetic Binary Nanocrystal Superlattice Membranes. *Nano Letters* **10,** 5103–5108 (2010).

[151] Yuan, B., Jin, Y., Sun, Y., Wang, D., Sun, J., Wang, Z., Zhang, W. & Jiang, X. A Strategy for Depositing Different Types of Cells in Three Dimensions to Mimic Tubular Structures in Tissues. *Advanced Materials* **24,** 890–896 (2012).

[152] Dorgan, L., Magnotti, R., Hou, J., Engle, T., Ruley, K. & Shull, B. Methods to determine biotin-binding capacity of streptavidin-coated magnetic particles. *Journal of Magnetism and Magnetic Materials* **194,** 69–75. ISSN: 0304-8853 (1999).

[153] Alben, S., Balakrisnan, B. & Smela, E. Edge Effects Determine the Direction of Bilayer Bending. *Nano Letters* **11,** 2280–2285 (2011).

[154] Wei, Y., Wang, B., Wu, J., Yang, R. & Dunn, M. L. Bending rigidity and Gaussian bending stiffness of single-layered graphene. *Nano letters* **13,** 26–30 (2013).

[155] Jia, L. L., Zakhary, M. J., Dogic, Z., Pelcovits, R. A. & Powers, T. R. Chiral edge fluctuations of colloidal membranes. *Physical Review E* **95,** 060701 (2017).

[156] Nelson, D. & Peliti, L. Fluctuations in membranes with crystalline and hexatic order. *Journal de physique* **48,** 1085–1092 (1987).

[157] Aronovitz, J. A. & Lubensky, T. C. Fluctuations of Solid Membranes. *Phys. Rev. Lett.* **60,** 2634–2637. `https://link.aps.org/doi/10.1103/PhysRevLett.60.2634` (25 June 1988).

[158] Zelisko, M., Ahmadpoor, F., Gao, H. & Sharma, P. Determining the Gaussian Modulus and Edge Properties of 2D Materials: From Graphene to Lipid Bilayers. *Phys. Rev. Lett.* **119,** 068002 (6 2017).

[159] Chabanov, A., Jun, Y. & Norris, D. J. Avoiding cracks in self-assembled photonic band-gap crystals. *Appl. Phys. Lett.* **84,** 3573–3575 (2004).

[160] Camassa, R., Leiterman, T. J. & McLaughlin, R. M. Trajectory and flow properties for a rod spinning in a viscous fluid. Part 1. An exact solution. *J. Fluid Mech.* **612,** 153–200 (2008).